Rosenthal, Y., Holbourn, A.E., Kulhanek, D.K., and the Expedition 363 Scientists
Proceedings of the International Ocean Discovery Program Volume 363
publications.iodp.org

https://doi.org/10.14379/iodp.proc.363.104.2018

Site U1483[1]

Y. Rosenthal, A.E. Holbourn, D.K. Kulhanek, I.W. Aiello, T.L. Babila, G. Bayon, L. Beaufort, S.C. Bova, J.-H. Chun, H. Dang, A.J. Drury, T. Dunkley Jones, P.P.B. Eichler, A.G.S. Fernando, K.A. Gibson, R.G. Hatfield, D.L. Johnson, Y. Kumagai, T. Li, B.K. Linsley, N. Meinicke, G.S. Mountain, B.N. Opdyke, P.N. Pearson, C.R. Poole, A.C. Ravelo, T. Sagawa, A. Schmitt, J.B. Wurtzel, J. Xu, M. Yamamoto, and Y.G. Zhang[2]

Keywords: International Ocean Discovery Program, IODP, *JOIDES Resolution*, Expedition 363, Site U1483, Northwest Australian margin, Scott Plateau, Browse Basin, Sunda arc, Neogene, Pliocene, Pleistocene, Indonesian Throughflow, Leeuwin Current, West Australian Current, eastern Indian Ocean, Timor Sea, Timor Strait, Australian monsoon, hydroclimate, precipitation reconstruction, southwestern sector Indo-Pacific Warm Pool, orbital-scale climate variability, carbonate accumulation, clay, tephra, soft-sediment deformation, exceptional foraminifer and nannofossil preservation, biosilica, stratigraphic intercalibration and cyclostratigraphy, anaerobic methane oxidation, sulfate–methane transition zone

Contents

Background and objectives

International Ocean Discovery Program (IODP) Site U1483 is located on the northwest Australian margin at 13°5.24′S, 121°48.25′E in 1733 m water depth (Figures **F1**, **F2**). The site is situated on seismic Line BR98-117, 1300 m northeast of the intersection with seismic Line BR98-168 and ~0.8 nmi southeast of the ~40 m long piston Core MD01-2378 (Figure **F3**), which provides insights into late Pleistocene sedimentation and stratigraphy at this location (e.g., Holbourn et al., 2005; Kuhnt et al., 2015). The interpretation of Miocene seismic reflectors is based on comparison to the Australian Geological Survey Organisation regional seismic survey Line 119-04 (well control by Buffon 1 and Brewster 1A) and the BBHR Line 175/10 (well control by Argus 1). A major unconformity marks the top of the prograding sequence at 0.72 s two-way traveltime below seafloor and is interpreted as the middle Miocene sequence boundary corresponding to a major sea level drop associated with rapid expansion of the Antarctic Ice Sheet (Mi-3; 13.8 Ma) (Rosenthal et al., 2016) (Figure **F4**).

Site U1483 is situated on the Scott Plateau at the northwestern margin of the northeast-trending Browse Basin, which underlies the Australian northwest margin between the onshore Kimberley Basin and the Scott Plateau (Symonds et al., 1994). This region, which is adjacent to some of the oldest ocean crust still in the world's ocean (Argo Abyssal Plain), formed after the breakup of Gondwanaland and the separation of northwest Australia from the Tethyan landmass (Gradstein, 1992). The Mesozoic section beneath the Scott Plateau is strongly influenced by breakup-related tectonism and forms the acoustic basement through much of the Scott Plateau area (Stagg and Exon, 1981). The postbreakup sedimentary succes-

Figure F1. Northwest Australian margin showing Sites U1482 and U1483 (yellow circles) on the Scott Plateau and the three main exit passages of the Indonesian Throughflow into the eastern Indian Ocean: the Lombok Strait (sill depth = 350 m), Ombai Strait (sill depth = 3250 m), and Timor Strait (sill depth = 1890 m). Contour interval = 500 m.

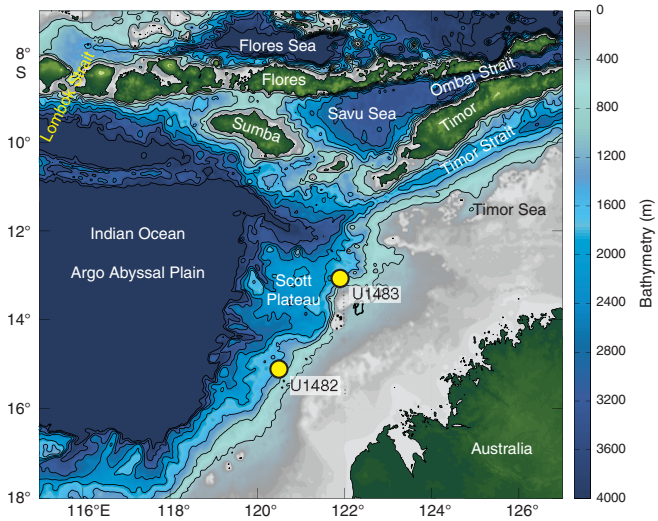

[1] Rosenthal, Y., Holbourn, A.E., Kulhanek, D.K., Aiello, I.W., Babila, T.L., Bayon, G., Beaufort, L., Bova, S.C., Chun, J.-H., Dang, H., Drury, A.J., Dunkley Jones, T., Eichler, P.P.B., Fernando, A.G.S., Gibson, K.A., Hatfield, R.G., Johnson, D.L., Kumagai, Y., Li, T., Linsley, B.K., Meinicke, N., Mountain, G.S., Opdyke, B.N., Pearson, P.N., Poole, C.R., Ravelo, A.C., Sagawa, T., Schmitt, A., Wurtzel, J.B., Xu, J., Yamamoto, M., and Zhang, Y.G., 2018. Site U1483. *In* Rosenthal, Y., Holbourn, A.E., Kulhanek, D.K., and the Expedition 363 Scientists, *Western Pacific Warm Pool*. Proceedings of the International Ocean Discovery Program, 363: College Station, TX (International Ocean Discovery Program). https://doi.org/10.14379/iodp.proc.363.104.2018

[2] **Expedition 363 Scientists' addresses.**

MS 363-104: Published 8 June 2018

Figure F2. Bathymetric map showing the location of Site U1483 (yellow circle). Bathymetry is based on R/V *Sonne* Cruise SO-185 bathymetric survey with multibeam echosounder SIMRAD EM 120 (Kuhnt et al., 2006).

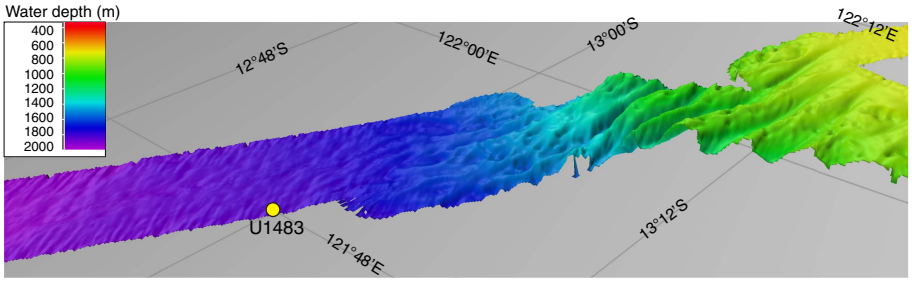

Figure F3. Contoured bathymetric map showing the location of Site U1483 (yellow circle) and piston Core MD01-2378 (white circle) on seismic Line BR98-168 (strike line), 1300 m northeast of the intersection with seismic Line BR98-117 (dip line). Contour interval = 100 m. Bathymetry from **http://www.gebco.net**.

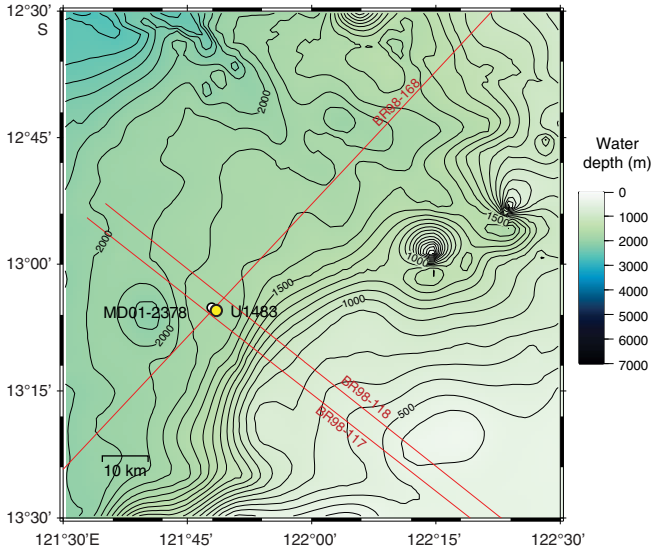

sion forms an ~2000 m thick, relatively uniform blanket over the Scott Plateau and the northeastern margin of Browse Basin. Site U1483 is located south of the Sunda arc, where ongoing collision between Australia and the Eurasia/Pacific arc system has occurred since the Miocene (Keep et al., 2007; Hall, 2012). However, intense Neogene faulting is mainly observed in the southernmost parts of the Browse Basin (Barcoo Subbasin), whereas the northern parts are relatively devoid of intense Neogene deformation (Keep et al., 2007).

Site U1483 is located ~142 nmi northeast of Site U1482. Both sites are within the hydrographic transition that separates the warm tropical water of the Indo-Pacific Warm Pool (IPWP) and subtropical water masses. Jointly, the two sites are suitable to monitor changes in the southward extent of tropical warm water related to circulation and/or global climate trends. Both sites are close to the oceanographic front between relatively cool, nutrient-rich water carried northward in the Eastern Indian Ocean by the West Australian Current and warm, oligotrophic Leeuwin Current water, which results in a steep north–south sea-surface temperature (SST) gradient (Figure **F5**).

The sedimentation rate at Site U1483 is ~9 cm/ky (Holbourn et al., 2005), about twice the rate at Site U1482, which will allow for the reconstruction of late Pliocene to recent paleoceanography at

Figure F4. A. Seismic Line BR98-168 with location of Site U1483 (13°5.24′S, 121°48.24′E; water depth = 1733 m). Location of crossing seismic lines shown with dashed lines at top. SP = shotpoint. B. Seismic Line BR98-117 showing projected location of Site U1483. CDP = common depth point.

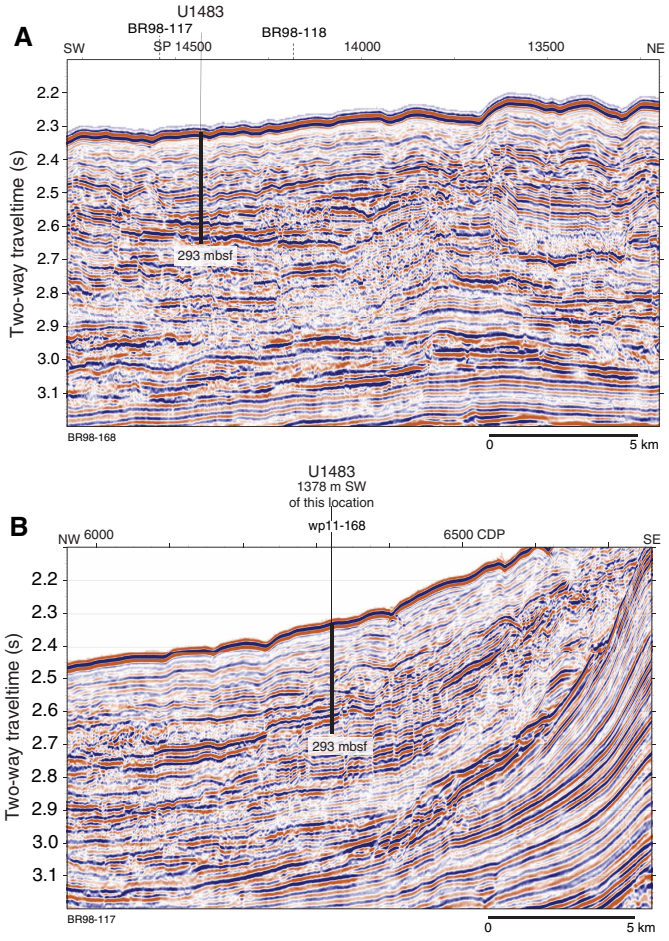

higher resolution than at Site U1482. Combined, the two sites will allow for reconstruction of the southwestern extent of the IPWP since the early late Miocene. Furthermore, the sites are located along the route of the Indonesian Throughflow (ITF) as it exits into the Indian Ocean through the Timor Strait between northwest Australia and Java (Figure **F1**). The Timor Strait is one of the three main exits of the ITF to the eastern Indian Ocean (Gordon, 2005). Thus, Sites U1482 and U1483 are ideally located to monitor changes in the intensity and thermal structure of ITF water masses entering the Eastern Indian Ocean (e.g., Xu et al., 2008).

Figure F5. Mean annual SST off Northwest Australia, illustrating the steep north–south SST gradient in the region (ODV World Ocean Atlas, 2013: **http://odv.awi.de/data/ocean/world-ocean-atlas-2013/**).

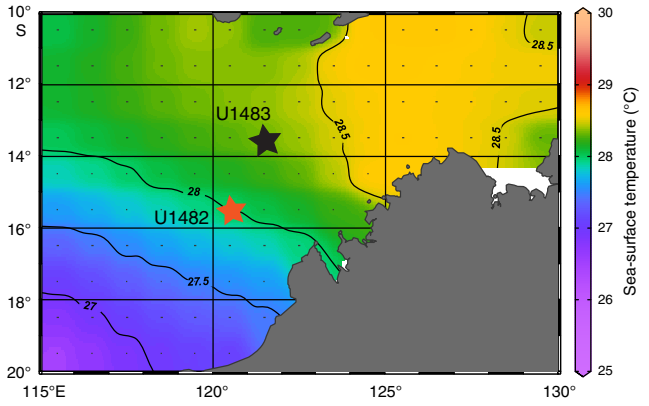

Operations

Transit to Site U1483

The 142 nmi transit to Site U1483 was completed in 12.5 h at an average speed of 11.4 kt. The vessel began lowering thrusters at 0618 h (all times are local ship time; UTC + 8 h) on 26 October 2016, switching to dynamic positioning control at 0630 h. We deployed the positioning beacon at 0650 h on 26 October.

Operations summary

We cored three holes at Site U1483 (Table **T1**). The original operations plan called for coring to advanced piston corer (APC) refusal (estimated at 250 meters below seafloor [mbsf]), followed by two additional holes deepened to 350 mbsf using the extended core barrel (XCB). Instead, we cored three holes using the APC to ~290 mbsf, the depth at which we encountered APC refusal. We decided not to deepen the holes to the original planned total depth because we had already reached our primary age target.

Hole U1483A was cored with the APC using the Icefield MI-5 core orientation tool and nonmagnetic hardware to 293.3 mbsf (Cores 363-U1483A-1H through 31H), where a partial stroke indicated APC refusal. Downhole temperature measurements using the advanced piston corer temperature tool (APCT-3) were taken on Cores 4H (37.1 mbsf), 7H (65.6 mbsf), 10H (94.1 mbsf), and 13H (122.6 mbsf), obtaining reliable results on three of the four deployments. A total of 308.58 m of sediment was recovered over 293.3 m of coring (105% recovery) in Hole U1483A.

Hole U1483B was then cored with the APC using the Icefield MI-5 core orientation tool and nonmagnetic hardware to 287.0 mbsf (Cores 363-U1483B-1H through 31H). A total of 301.62 m of sediment was collected over this interval (105% recovery). Oriented APC coring using the Icefield MI-5 orientation tool with nonmagnetic hardware continued in Hole U1483C and reached 284.8 mbsf (Cores 363-U1483C-1H through 31H). One drilled interval (3 m) advanced the hole without coring to avoid alignment of core gaps for stratigraphic correlation. A total of 292.42 m of core was recovered over 281.8 m of coring (104% recovery). Operations at Site U1483 ended at 0800 h on 30 October 2016. Total time spent at the site was 97.5 h (4.1 days).

A total of 92 APC cores were recovered at this site, collecting 902.62 m of sediment over 862.1 m of penetration (105.2% recovery).

Hole U1483A

After deploying the positioning beacon, we prepared and spaced out the bottom-hole assembly (BHA), which consisted of an APC/XCB coring assembly with two stands of drill collars. During deployment of the drill string, the seafloor depth was measured at 1747.4 meters below rig floor (mbrf) with the precision depth recorder (PDR), and we decided to shoot the first core from a depth of 1743 mbrf.

Hole U1483A was spudded at 1250 h on 26 October 2016 with Core 363-U1483A-1H recovering 8.6 m of core, establishing a seafloor depth of 1732.9 meters below sea level (mbsl). Oriented APC coring using the Icefield MI-5 core orientation tool with nonmagnetic hardware continued to 236.6 mbsf (Core 25H). Downhole temperature measurements were taken with the APCT-3 on Cores 4H (37.1 mbsf), 7H (56.1 mbsf), 10H (84.6 mbsf), and 13H (113.1 mbsf), obtaining good measurements on three of the four deployments. While retrieving Core 26H, the forward core winch wire parted, leaving the core barrel in the hole. The core winch wire was restrung in the derrick and reheaded. We prepared a fishing spear and lowered it into the drill pipe. The core was retrieved and pulled to surface during the second fishing attempt. After Core 26H was laid out, APC coring continued to 293.3 mbsf (Core 31H), where we encountered a partial stroke, indicating APC refusal and ending Hole U1483A. Total time spent in Hole U1483A was 42.25 h (1.8 days).

A total of 31 APC cores were taken in Hole U1483A. We recovered 308.58 m of sediment over 293.3 m of coring for an average recovery of 105.2%.

Hole U1483B

The vessel was offset 20 m east of Hole U1483A, the drill string was spaced out to 1737.5 mbrf, and Hole U1483B was spudded at 0205 h on 28 October 2016. Core 363-U1483B-1H recovered 2.05 m of sediment, establishing a seafloor depth of 1734.0 mbsl. Oriented APC coring using the Icefield MI-5 core orientation tool with nonmagnetic hardware proceeded to 287.0 mbsf (Cores 1H through 31H). We terminated Hole U1483B just above where we reached APC refusal in Hole U1483A. Total time spent in Hole U1483B was 25.5 h (1.1 days).

A total of 31 APC cores were taken in Hole U1483B, recovering 301.62 m of sediment over 287.0 m of coring (105.1% recovery).

Hole U1483C

The vessel was offset 20 m south of Hole U1483B, the bit was set at 1739.0 mbrf, and Hole U1483C was spudded at 0330 h on 29 October 2016. Core 363-U1483C-1H recovered 6.3 m of sediment, establishing a seafloor depth of 1731.2 mbsl. Oriented APC coring using the Icefield MI-5 core orientation tool with nonmagnetic hardware penetrated to 284.8 mbsf (Cores 1H through 30H). One drilled interval advanced the bit 3 m to offset core gaps for stratigraphic correlation. After reaching our depth target, we retrieved the drill string to the vessel and secured the rig floor for transit. The thrusters were raised at 0740 h, and we departed for Site U1484 at 0754 h on 30 October, ending operations at Site U1483. Total time spent in Hole U1483C was 29.75 h (1.2 days).

Hole U1483C consisted of 30 APC cores recovering 292.42 m of sediment over 281.8 m of coring (103.8% recovery). A single drilled interval advanced the hole 3 m without coring.

Table T1. Site U1483 core summary. CSF = core depth below seafloor (mbsf in text), DRF = drilling depth below rig floor, DSF = drilling depth below seafloor. APC = advanced piston corer, XCB = extended core barrel. Core types: H = advanced piston corer, numeric core type = drilled interval. APCT-3 = advanced piston corer temperature tool, Icefield = orientation tool. (Continued on next two pages.) **Download table in CSV format.**

Hole U1483A
Latitude: 13°05.2382′S
Longitude: 121°48.2424′E
Water depth (m): 1732.93
Date started (UTC): 25 October 2016, 2230 h
Date finished (UTC): 27 October 2016, 1650 h
Time on hole (days): 1.76
Seafloor depth DRF (m): 1743.9
Seafloor depth calculation method: APC calculated depth
Rig floor to sea level (m): 10.97
Drilling system: 11-7/16 inch APC/XCB DC280 bit
Penetration DSF (m): 293.3
Cored interval (m): 293.3
Recovered length (m): 308.58
Recovery (%): 105.21
Total cores (no.): 31
APC cores (no.): 31
Age of oldest sediment cored: mid-Pliocene

Hole U1483B
Latitude: 13°05.2371′S
Longitude: 121°48.2538′E
Water depth (m): 1734.01
Date started (UTC): 27 October 2016, 1650 h
Date finished (UTC): 28 October 2016, 1810 h
Time on hole (days): 1.06
Seafloor depth DRF (m): 1745.0
Seafloor depth calculation method: APC calculated depth
Rig floor to sea level (m): 10.99
Drilling system: 11-7/16 inch APC/XCB DC280 bit
Penetration DSF (m): 287.0
Cored interval (m): 287.0
Recovered length (m): 301.62
Recovery (%): 105.09
Total cores (no.): 31
APC cores (no.): 31
Age of oldest sediment cored: mid-Pliocene

Hole U1483C
Latitude: 13°05.2479′S
Longitude: 121°48.2537′E
Water depth (m): 1731.19
Date started (UTC): 28 October 2016, 1810 h
Date finished (UTC): 30 October 2016, 0000 h
Time on hole (days): 1.24
Seafloor depth DRF (m): 1742.2
Seafloor depth calculation method: APC calculated depth
Rig floor to sea level (m): 11.01
Drilling system: 11-7/16 inch APC/XCB DC280 bit
Penetration DSF (m): 284.8
Cored interval (m): 281.8
Recovered length (m): 292.42
Recovery (%): 103.77
Drilled interval (m): 3.0
Drilled interval (no.): 1
Total cores (no.): 30
APC cores (no.): 30
Age of oldest sediment cored: mid-Pliocene

Core	Date (2016)	Time on deck UTC (h)	Depth DSF (m) Top of interval	Depth DSF (m) Bottom of interval	Interval advanced (m)	Depth CSF (m) Top of cored interval	Depth CSF (m) Bottom of cored interval	Recovered length (m)	Curated length (m)	Recovery (%)	Sections (*N*)	Comments
363-U1483A-												
1H	26 Oct	0505	0	8.6	8.6	0	8.63	8.63	8.63	100	7	Icefield
2H	26 Oct	0555	8.6	18.1	9.5	8.6	18.61	10.01	10.01	105	8	Icefield
3H	26 Oct	0640	18.1	27.6	9.5	18.1	28.04	9.94	9.94	105	8	Icefield
4H	26 Oct	0735	27.6	37.1	9.5	27.6	37.82	10.22	10.22	108	8	Icefield, APCT-3
5H	26 Oct	0815	37.1	46.6	9.5	37.1	47.08	9.98	9.98	105	8	Icefield
6H	26 Oct	0855	46.6	56.1	9.5	46.6	56.53	9.93	9.93	105	8	Icefield
7H	26 Oct	0945	56.1	65.6	9.5	56.1	66.17	10.07	10.07	106	8	Icefield, APCT-3
8H	26 Oct	1025	65.6	75.1	9.5	65.6	75.51	9.91	9.91	104	8	Icefield
9H	26 Oct	1105	75.1	84.6	9.5	75.1	85.09	9.99	9.99	105	8	Icefield
10H	26 Oct	1155	84.6	94.1	9.5	84.6	94.65	10.05	10.05	106	8	Icefield, APCT-3
11H	26 Oct	1230	94.1	103.6	9.5	94.1	104.09	9.99	9.99	105	8	Icefield
12H	26 Oct	1530	103.6	113.1	9.5	103.6	113.81	10.18	10.21	107	8	Icefield
13H	26 Oct	1625	113.1	122.6	9.5	113.1	123.44	10.34	10.37	109	8	Icefield, APCT-3, imploded liner (bottom)
14H	26 Oct	1700	122.6	132.1	9.5	122.6	132.31	9.71	9.71	102	8	Icefield
15H	26 Oct	1735	132.1	141.6	9.5	132.1	142.32	10.22	10.22	108	8	Icefield
16H	26 Oct	1815	141.6	151.1	9.5	141.6	151.35	9.75	9.75	103	8	Icefield, imploded liner (bottom)
17H	26 Oct	1855	151.1	160.6	9.5	151.1	161.50	10.40	10.40	109	8	Icefield
18H	26 Oct	1935	160.6	170.1	9.5	160.6	170.25	9.65	9.65	102	8	Icefield, imploded liner (bottom)
19H	26 Oct	2010	170.1	179.6	9.5	170.1	180.11	10.01	10.01	105	8	Icefield, imploded liner (top)
20H	26 Oct	2130	179.6	189.1	9.5	179.6	189.62	10.02	10.02	105	8	Icefield
21H	26 Oct	2225	189.1	198.6	9.5	189.1	198.85	9.75	9.75	103	9	Icefield
22H	26 Oct	2300	198.6	208.1	9.5	198.6	208.52	9.92	9.92	104	8	Icefield, imploded liner (bottom)
23H	26 Oct	2340	208.1	217.6	9.5	208.1	218.02	9.92	9.92	104	8	Icefield

Table T1 (continued). (Continued on next page.)

Core	Date (2016)	Time on deck UTC (h)	Depth DSF (m) Top of interval	Depth DSF (m) Bottom of interval	Interval advanced (m)	Depth CSF (m) Top of cored interval	Depth CSF (m) Bottom of cored interval	Recovered length (m)	Curated length (m)	Recovery (%)	Sections (*N*)	Comments
24H	27 Oct	0020	217.6	227.1	9.5	217.6	227.93	10.33	10.33	109	8	Icefield
25H	27 Oct	0050	227.1	236.6	9.5	227.1	237.22	10.12	10.12	107	8	Icefield
26H	27 Oct	0810	236.6	246.1	9.5	236.6	246.71	10.11	10.11	106	8	Icefield, core line parted, core retrieved on 2nd fishing run
27H	27 Oct	1025	246.1	255.6	9.5	246.1	256.12	10.02	10.02	105	8	Icefield
28H	27 Oct	1115	255.6	265.1	9.5	255.6	265.37	9.77	9.77	103	8	Icefield
29H	27 Oct	1200	265.1	274.6	9.5	265.1	275.21	10.11	10.11	106	8	Icefield
30H	27 Oct	1300	274.6	284.1	9.5	274.6	284.86	10.26	10.26	108	8	Icefield
31H	27 Oct	1350	284.1	293.3	9.2	284.1	293.37	9.27	9.27	101	9	Icefield, pumped out liner
363-U1483B-												
1H	27 Oct	1815	0	2.0	2.0	0.0	2.05	2.05	2.05	103	3	Icefield
2H	27 Oct	1915	2.0	11.5	9.5	2.0	11.90	9.90	9.90	104	8	Icefield
3H	27 Oct	1955	11.5	21.0	9.5	11.5	21.35	9.85	9.85	104	8	Icefield
4H	27 Oct	2030	21.0	30.5	9.5	21.0	30.94	9.94	9.94	105	8	Icefield
5H	27 Oct	2105	30.5	40.0	9.5	30.5	40.41	9.91	9.91	104	8	Icefield
6H	27 Oct	2155	40.0	49.5	9.5	40.0	49.92	9.92	9.92	104	8	Icefield
7H	27 Oct	2230	49.5	59.0	9.5	49.5	59.46	9.96	9.96	105	8	Icefield
8H	27 Oct	2305	59.0	68.5	9.5	59.0	69.06	10.06	10.06	106	8	Icefield
9H	27 Oct	2345	68.5	78.0	9.5	68.5	78.27	9.77	9.77	103	8	Icefield
10H	28 Oct	0045	78.0	87.5	9.5	78.0	88.04	10.04	10.04	106	8	Icefield
11H	28 Oct	0120	87.5	97.0	9.5	87.5	97.25	9.75	9.75	103	8	Icefield
12H	28 Oct	0200	97.0	106.5	9.5	97.0	107.08	10.08	10.08	106	8	Icefield
13H	28 Oct	0235	106.5	116.0	9.5	106.5	116.36	9.86	9.86	104	8	Icefield
14H	28 Oct	0310	116.0	125.5	9.5	116.0	126.47	10.47	10.47	110	8	Icefield
15H	28 Oct	0400	125.5	135.0	9.5	125.5	135.22	9.72	9.72	102	8	Icefield
16H	28 Oct	0440	135.0	144.5	9.5	135.0	145.34	10.34	10.34	109	8	Icefield
17H	28 Oct	0515	144.5	154.0	9.5	144.5	154.74	10.24	10.24	108	8	Icefield
18H	28 Oct	0555	154.0	163.5	9.5	154.0	164.16	10.16	10.16	107	8	Icefield
19H	28 Oct	0635	163.5	173.0	9.5	163.5	173.35	9.85	9.85	104	8	Icefield
20H	28 Oct	0720	173.0	182.5	9.5	173.0	183.06	10.06	10.06	106	8	Icefield
21H	28 Oct	0810	182.5	192.0	9.5	182.5	192.98	10.48	10.48	110	8	Icefield
22H	28 Oct	0905	192.0	201.5	9.5	192.0	202.24	10.24	10.24	108	8	Icefield
23H	28 Oct	0955	201.5	211.0	9.5	201.5	210.80	9.30	9.30	98	8	Icefield
24H	28 Oct	1035	211.0	220.5	9.5	211.0	221.15	10.15	10.15	107	8	Icefield
25H	28 Oct	1155	220.5	230.0	9.5	220.5	230.68	10.18	10.18	107	8	Icefield
26H	28 Oct	1240	230.0	239.5	9.5	230.0	239.84	9.84	9.84	104	8	Icefield
27H	28 Oct	1320	239.5	249.0	9.5	239.5	249.22	9.72	9.72	102	8	Icefield, liner imploded (bottom)
28H	28 Oct	1405	249.0	258.5	9.5	249.0	259.31	10.31	10.31	109	8	Icefield
29H	28 Oct	1450	258.5	268.0	9.5	258.5	268.18	9.68	9.68	102	8	Icefield
30H	28 Oct	1530	268.0	277.5	9.5	268.0	278.17	10.17	10.17	107	8	Icefield
31H	28 Oct	1610	277.5	287.0	9.5	277.5	287.12	9.62	9.62	101	8	Icefield
363-U1483C-												
1H	28 Oct	1940	0	6.3	6.3	0	6.33	6.33	6.33	100	6	Icefield
2H	28 Oct	2030	6.3	15.8	9.5	6.3	16.08	9.78	9.78	103	8	Icefield
3H	28 Oct	2105	15.8	25.3	9.5	15.8	25.48	9.68	9.68	102	8	Icefield
4H	28 Oct	2150	25.3	34.8	9.5	25.3	34.80	9.50	9.50	100	8	Icefield
5H	28 Oct	2225	34.8	44.3	9.5	34.8	44.37	9.57	9.57	101	8	Icefield
6H	28 Oct	2300	44.3	53.8	9.5	44.3	53.90	9.60	9.60	101	8	Icefield
7H	28 Oct	2335	53.8	63.3	9.5	53.8	63.74	9.94	9.94	105	8	Icefield
8H	29 Oct	0010	63.3	72.8	9.5	63.3	73.06	9.76	9.76	103	8	Icefield
9H	29 Oct	0045	72.8	82.3	9.5	72.8	82.75	9.95	9.95	105	8	Icefield
10H	29 Oct	0120	82.3	91.8	9.5	82.3	92.20	9.90	9.90	104	8	Icefield
11H	29 Oct	0155	91.8	101.3	9.5	91.8	101.84	10.04	10.04	106	8	Icefield
12H	29 Oct	0230	101.3	110.8	9.5	101.3	110.97	9.65	9.67	102	8	Icefield
13H	29 Oct	0305	110.8	120.3	9.5	110.8	121.04	10.24	10.24	108	8	Icefield
14H	29 Oct	0355	120.3	129.8	9.5	120.3	129.89	9.59	9.59	101	8	Icefield
15H	29 Oct	0435	129.8	139.3	9.5	129.8	140.09	10.29	10.29	108	8	Icefield
16H	29 Oct	0520	139.3	148.8	9.5	139.3	148.81	9.51	9.51	100	7	Icefield, liner imploded (bottom)
17H	29 Oct	0600	148.8	158.3	9.5	148.8	159.05	10.25	10.25	108	8	Icefield
18H	29 Oct	0640	158.3	167.8	9.5	158.3	168.17	9.87	9.87	104	8	Icefield
19H	29 Oct	0725	167.8	177.3	9.5	167.8	177.25	9.45	9.45	99	8	Icefield, shattered liner, pumped out
20H	29 Oct	0920	177.3	186.8	9.5	177.3	187.30	10.00	10.00	105	8	Icefield, replaced inner, outer, and piston seals
21H	29 Oct	1010	186.8	196.3	9.5	186.8	196.72	9.92	9.92	104	8	Icefield, liner imploded (bottom)
221	29 Oct	1020	196.3	199.3	3.0	*****Drilled from 196.3 to 199.3 m DSF without coring*****						
23H	29 Oct	1055	199.3	208.8	9.5	199.3	208.92	9.62	9.62	101	7	Icefield, liner imploded (bottom)
24H	29 Oct	1140	208.8	218.3	9.5	208.8	218.61	9.81	9.81	103	8	Icefield

Table T1 (continued).

Core	Date (2016)	Time on deck UTC (h)	Depth DSF (m) Top of interval	Depth DSF (m) Bottom of interval	Interval advanced (m)	Depth CSF (m) Top of cored interval	Depth CSF (m) Bottom of cored interval	Recovered length (m)	Curated length (m)	Recovery (%)	Sections (*N*)	Comments
25H	29 Oct	1220	218.3	227.8	9.5	218.3	228.38	10.08	10.08	106	8	Icefield
26H	29 Oct	1310	227.8	237.3	9.5	227.8	237.70	9.90	9.90	104	8	Icefield, liner imploded (bottom)
27H	29 Oct	1355	237.3	246.8	9.5	237.3	247.03	9.73	9.73	102	8	Icefield
28H	29 Oct	1440	246.8	256.3	9.5	246.8	256.88	10.08	10.08	106	8	Icefield
29H	29 Oct	1520	256.3	265.8	9.5	256.3	266.41	10.11	10.11	106	8	Icefield, liner imploded (bottom)
30H	29 Oct	1605	265.8	275.3	9.5	265.8	276.20	10.40	10.40	109	8	Icefield
31H	29 Oct	1645	275.3	284.8	9.5	275.3	285.14	9.87	9.84	104	9	Icefield

Core description

We cored three holes at Site U1483, with the deepest hole penetrating to 293.37 mbsf (Hole U1483A). The succession recovered from Holes U1483A–U1483C is composed of pelagic and hemipelagic lower Pliocene to recent sediment. The sequence at Site U1483 is assigned to one lithologic unit and three subunits defined on the basis of a combination of visual core description, microscopic examination of smear slides, magnetic susceptibility, color spectral observations, and bulk mineralogical analysis by X-ray diffraction (XRD) (see **Core description** and **Physical properties** in the Expedition 363 methods chapter [Rosenthal et al., 2018a]). The major characteristics of the sedimentary sequence at Site U1483 are illustrated in Figure **F6**.

Unit descriptions

Unit I

Intervals: 363-U1483A-1H-1, 0 cm, through 31H-CC, 63 cm; 363-U1483B-1H-1, 0 cm, through 31H-CC, 17 cm; 363-U1483C-1H-1, 0 cm, through 31H-CC, 22 cm
Depths: Hole U1483A = 0–293.37 mbsf, Hole U1483B = 0–287.12 mbsf, Hole U1483C = 0–285.14 mbsf
Thickness: Hole U1483A = 293.37 m, Hole U1483B = 287.12 m, Hole U1483C = 285.14 m.
Age: early Pliocene to recent
Lithology: nannofossil ooze, clay-rich nannofossil ooze, nannofossil-rich clay, diatom-bearing clay-rich nannofossil ooze, diatom-rich nannofossil clay, clay-rich foraminifer nannofossil ooze, clay-rich diatom nannofossil ooze, nannofossil-bearing foraminifer-rich clay, foraminifer ooze, and ash

Unit I is mainly composed of greenish gray nannofossil ooze with variable amounts of clay, foraminifers, and siliceous microfossils. The unit is divided into three lithologic subunits based on minor changes in lithology and sedimentological features. Subunit IA is dominated by clay-bearing to clay-rich nannofossil ooze, whereas in Subunit IB diatoms become an important and occasionally major sedimentary component (Figure **F7**). Subunit IC is characterized by the occurrence of several intervals showing soft-sediment deformation with thicknesses that range between ~3 and 25 m (Figure **F8**; Table **T2**). Throughout Unit I, sediment color alternates from light greenish gray to dark greenish gray, with occasional brownish gray intervals. These cyclic variations occur on decimeter to meter scales and exhibit gradual transitions. The sediment is moderately to heavily bioturbated throughout, and several tephra layers are present within the sediment succession (Figures **F9**, **F10**; Table **T3**). XRD mineralogical analysis was performed on bulk sediment samples from the three dominant color intervals: darker greenish gray, lighter greenish gray, and brownish gray (Figure **F11**). Despite color differences, all analyses show similar mineral compositions with calcite as the dominant mineral.

Subunit IA

Intervals: 363-U1483A-1H-1, 0 cm, through 7H-1, 45 cm; 363-U1483B-1H-1, 0 cm, through 7H-5, 79 cm; 363-U1483C-1H-1, 0 cm, through 7H-4, 62 cm
Depths: Hole U1483A = 0–56.55 mbsf, Hole U1483B = 0–56.15 mbsf, Hole U1483C = 0–58.92 mbsf
Thickness: Hole U1483A = 56.55 m, Hole U1483B = 56.15 m, Hole U1483C = 58.92 m
Age: middle Pleistocene to recent
Lithology: clay-rich foraminifer nannofossil ooze, clay-rich nannofossil ooze, clay-bearing foraminifer-rich nannofossil ooze, nannofossil-rich clay, diatom-bearing clay-rich nannofossil ooze, and ash

Subunit IA is mainly composed of greenish gray clay-bearing and clay-rich nannofossil ooze. The top of the subunit consists of ~3.5 cm of light brownish nannofossil-rich clay above a ~2–4 cm thick very dark brown nannofossil-rich clay layer, marking the redox transition. Below this interval, sediment color gradually changes to light greenish gray. This subunit shows multiple meter-scale alternations between dark greenish gray and light greenish gray layers (Figure **F12**). Color variations correspond to lithologic changes, which are also apparent in natural gamma radiation (NGR) and L* variations (Figure **F6**). Smear slide analysis suggests that higher NGR and lower L* values correspond to higher clay content in the sediment. The sediment is moderately to heavily bioturbated. Sponge spicules and molluscan shell fragments are common throughout the subunit, whereas pteropods are only observed in the upper ~40 mbsf. Dark green vertically elongated spots, which might be burrows filled with clay minerals, are observed in the uppermost ~20 mbsf. A 1.7–2.0 cm thick dark gray tephra layer consisting mostly of vesicular glass fragments (Figure **F10A**) corresponds to a distinct magnetic susceptibility peak (see **Physical properties**) in all holes (intervals 363-U1483A-3H-6, 118–120 cm; 363-U1483B-4H-3, 98–100 cm; and 363-U1483C-4H-2, 73–75 cm).

The lithologic boundary between Subunits IA and IB is located at 363-U1483A-7H-1, 45 cm (56.55 mbsf); 363-U1483B-7H-5, 79 cm (56.15 mbsf); and 363-U1483C-7H-4, 62 cm (58.92 mbsf). The boundary is defined at the first downhole appearance of brownish gray diatom-rich nannofossil ooze, which becomes more abundant in Subunit IB.

Figure F6. Lithologic summary, Site U1483. cps = counts per second.

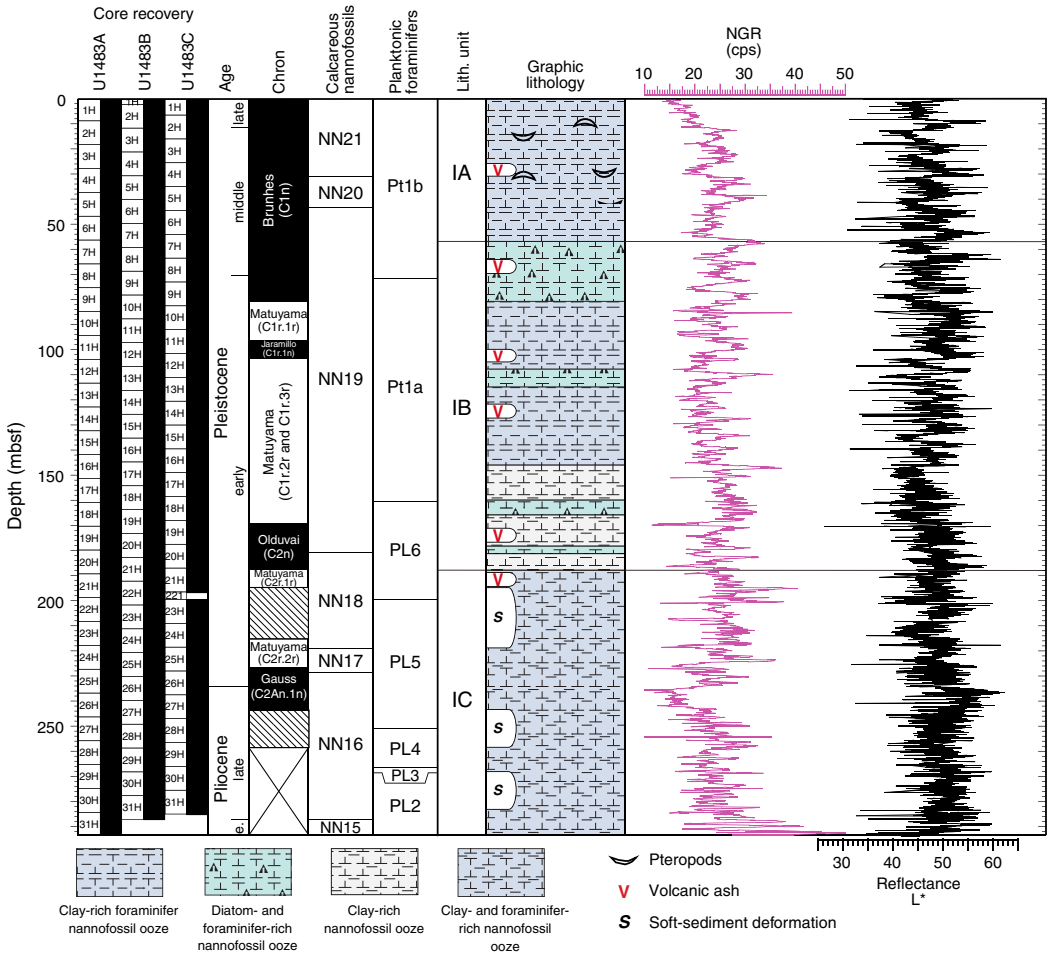

Subunit IB

Intervals: 363-U1483A-7H-1, 45 cm, through 20H-6, 80 cm; 363-U1483B-7H-5, 79 cm, through 21H-1, 0 cm; 363-U1483C-7H-4, 62 cm, through 21H-1, 0 cm

Depths: Hole U1483A = 56.55–187.30 mbsf, Hole U1483B = 56.15–182.50 mbsf, Hole U1483C = 58.92–186.80 mbsf

Thickness: Hole U1483A = 130.75 m, Hole U1483B = 126.35 m, Hole U1483C = 127.88 m

Age: early to middle Pleistocene

Lithology: clay-rich nannofossil ooze, diatom-rich nannofossil clay, clay-rich diatom nannofossil ooze, and ash

Subunit IB is mainly composed of greenish gray clay-rich nannofossil ooze, diatom-rich nannofossil clay, and clay-rich diatom-nannofossil ooze. This subunit is characterized by higher biosiliceous content than Subunit IA (Figure **F7A, F7B**), and the clay content increases in the lower part of the subunit (Figure **F6**). Gradual sediment color changes occur in cycles that have approximately the length of a section (~1.5 m) (Figure **F13**), which is of shorter amplitude than the color alternations observed in Subunit IA. We found a general correlation between higher abundances of diatoms in smear slides (as well as radiolarians, silicoflagellates, and organic debris) and olive-gray to dark greenish gray sediment color. Sediment that has lower abundances of diatoms is light greenish gray to greenish gray. The sediment is moderately to heavily bioturbated, and sponge spicules and shell fragments are common. Bulk XRD analyses indicate only small differences in mineralogical composition between sediment with different colors (Figure **F11**). Two ~3 cm thick layers with sharp erosional bases that contain higher concentrations of foraminifers were observed in intervals 363-U1483A-19H-5, 112–115 cm, and 363-U1483B-20H-1, 123–126 cm. In interval 363-U1483B-8H-7, 62–65 cm, we observed an ~2 cm × 2 cm large white concretion with large mineral faces visible to the unaided eye. The concretion is composed of two parts: (1) an intergrowth of euhedral gypsum crystals at the top and (2) a gray-brown nodule at the bottom with biotite and another unknown mineral (possibly barite) (Figure **F14**). Tephra layers of various colors with thicknesses of 1–5 cm occur within this subunit (Figure **F9**; Table **T3**).

The lithologic boundary between Subunits IB and IC is located at 363-U1483A-20H-6, 80 cm (187.30 mbsf), 363-U1483B-21H-1, 0 cm (182.50 mbsf), and 363-U1483C-21H-1, 0 cm (186.80 mbsf). The boundary is defined by a significant reduction in the abundance of diatoms and radiolarians below these depths.

Subunit IC

Intervals: 363-U1483A-20H-6, 80 cm, through 31H-CC, 63 cm (total depth); 363-U1483B-21H-1, 0 cm, through 31H-CC, 17 cm (total depth); 363-U1483C-21H-1, 0 cm, through 31H-CC, 22 cm (total depth)

Depths: Hole U1483A = 187.30–293.37 mbsf (total depth), Hole U1483B = 182.50–287.12 mbsf (total depth), Hole U1483C = 186.80–285.14 mbsf (total depth)
Thickness: Hole U1483A = 106.07 m, Hole U1483B = 104.62 m, Hole U1483C = 98.34 m
Age: early Pliocene to early Pleistocene
Lithology: foraminifer-rich nannofossil clay, clay- and foraminifer-rich nannofossil ooze, foraminifer-bearing clay-rich nannofossil ooze, nannofossil-bearing foraminifer-rich clay, foraminifer ooze, and ash

Subunit IC is mainly composed of greenish gray foraminifer-rich nannofossil clay and greenish gray foraminifer-bearing clay-rich nannofossil ooze (Figure F15). Large portions of this subunit show features such as folding, tilting, and fine-scale sediment foliation indicative of soft-sediment deformation (Figure F8; Table T2). Several distinct types of structures were observed in the deformed intervals, including inclined bedding, folding, microfaulting, foliation, and homogeneous sections (Figure F8), indicating complex deformational processes. Coarser grains are mainly planktonic foraminifers, and several layers with concentrations of foraminifers show sharp basal erosional contacts and fining-upward graded bedding. Overall, in the three holes cored at Site U1483, soft-sediment deformation is concentrated within two major intervals separated by a relatively undisturbed portion of sediment. The upper interval, which is about 24 m thick in all holes (Table T2), is topped by a prominent ash layer and contains mainly tilted and folded beds often outlined by a prominent dark gray, stiff clay layer. The lower deformed interval is less continuous between the holes and is thickest in Holes U1483B and U1483C. The main types of deformation include foliation and folding. Dark gray clay layers are also present, and some occur at a high angle relative to bedding. It is worth noting that the top and base of each deformed interval are not always clearly defined.

Two tephra layers 1–4 cm thick are found within Subunit IC (Figures F9, F10; Table T3). The upper tephra layer is located in intervals 363-U1483A-21H-4, 41–42 cm; 363-U1483B-21H-7, 123–127 cm; and 363-U1483C-21H-6, 91–94 cm, and is 2–20 cm above the uppermost deformed interval, whereas the lower tephra is located in intervals 363-U1483A-30H-1, 32–34 cm, and 363-U1483B-30H-7, 20–22 cm, and is within or below the lowermost deformed interval.

Figure F7. Main sedimentary components, Subunit IB, Site U1483. A, B. Diatom-rich nannofossil ooze. C, D. Clay-rich nannofossil clay. E, F. Nannofossil ooze. A, C, and E: plane-polarized light (PPL); B, D, and F: cross-polarized light (XPL).

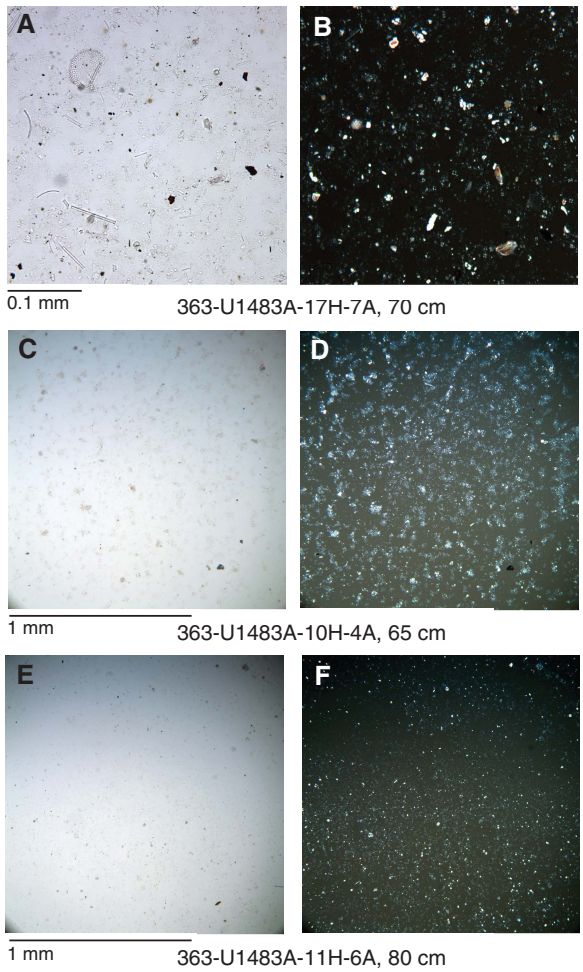

Figure F8. Soft-sediment deformation in Subunit IC, Site U1483. A. Mixture of fine-grained sediment with foraminifer-rich coarser layers (U1483A-22H-1A, 72–100 cm). B. Homogenized clay-rich dark layers (U1483A-22H-2A, 57–85 cm). C. Laminations with variable grain sizes and colors (U1483A-22H-2A, 72–100 cm). D. Inclined, fine, and foliated sediment (U1483B-27H-2A, 112–140 cm). E. Folding (U1483A-28H-2A, 110–139 cm).

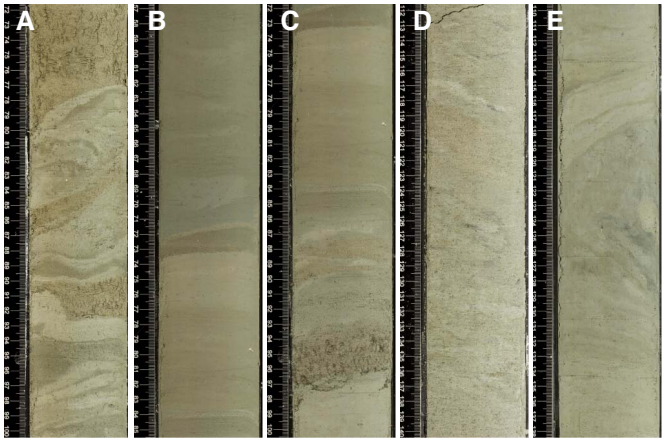

Table T2. Intervals of soft-sediment deformation, Site U1483. **Download table in CSV format.**

Top		Base		
Core, section, interval (cm)	Depth (mbsf)	Core, section, interval (cm)	Depth (mbsf)	Thickness (cm)
363-U1483A-		363-U1483A-		
21H-4, 44	193.78	23H-CC, 5	218.02	24.24
26H-5, 134	243.41	28H-2, 140	258.22	14.81
363-U1483B-		363-U1483B-		
22H-1, 0	192.00	24H-4, 144	216.46	24.46
27H-2, 80	241.80	27H-7, 110	249.09	7.29
28H-5, 0	254.75	28H-6, 150	257.70	2.95
30H-1, 0	268.00	31H-4, 142	280.54	12.54
363-U1483C-		363-U1483C-		
21H-6, 114	195.13	25H-1, 88	219.18	24.05
27H-5, 123	244.19	28H-3, 76	250.38	6.19
28H-7, 78	256.24	30H-7, 137	275.92	19.68

Figure F9. Tephra layers (red arrows), Site U1483. A. Subunit IA. B–G. Subunit IB. H, I. Subunit IC.

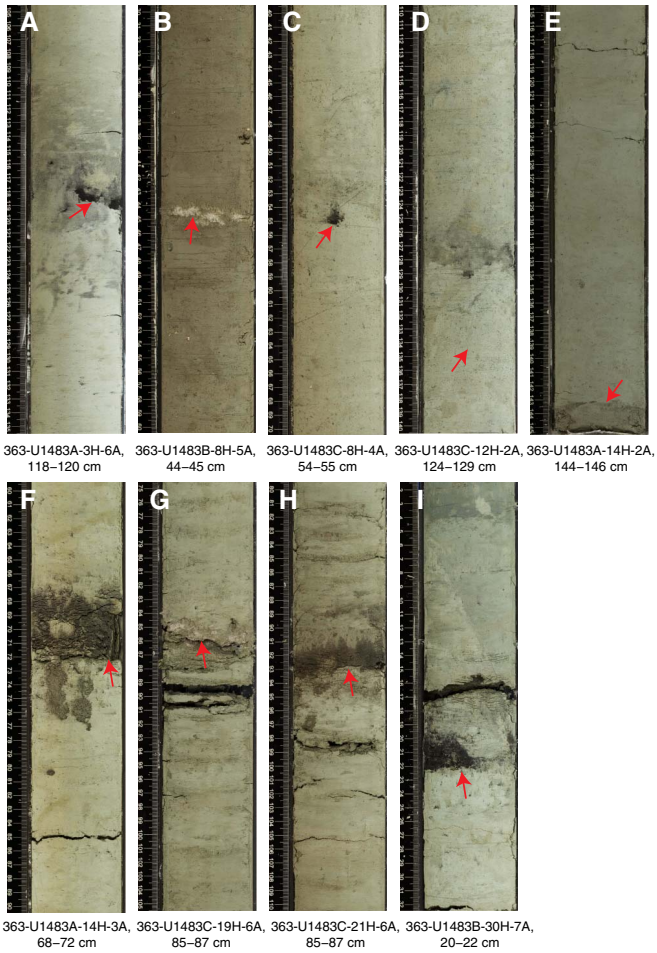

Figure F10. SEM photomicrographs of selected tephra samples, Site U1483.

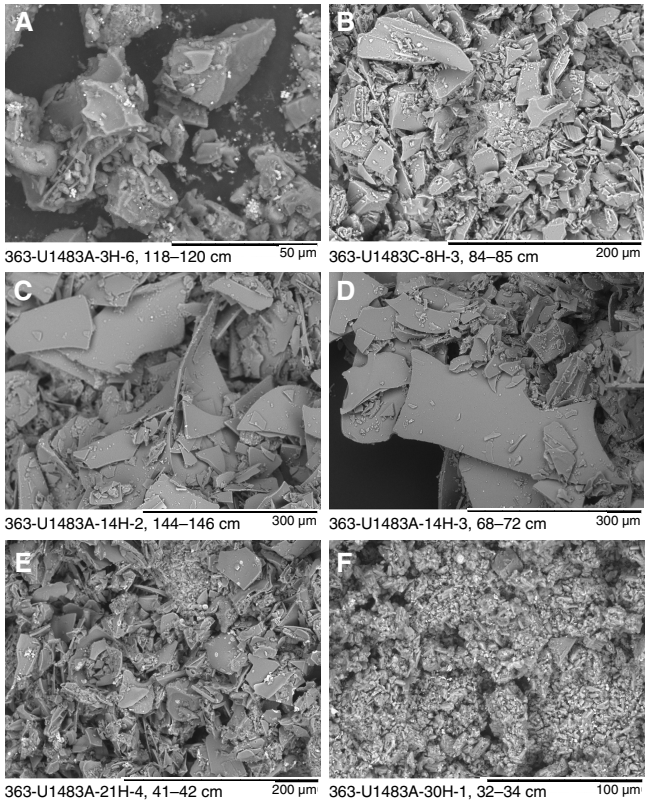

Table T3. Tephra layers, Site U1483. **Download table in CSV format.**

Core, section, interval (cm)	Approximate thickness (cm)	Color
363-U1483A-		
3H-6, 118–120	2	Dark gray
8H-1, 65–66	1	White
14H-2, 114–146	2	Gray
14H-3, 68–72	4	Gray
21H-4, 41–42	1	Gray
30H-1, 32–34	2	Dark gray
363-U1483B-		
4H-3, 98–100	2	Dark gray
8H-5, 44–45	1	White
21H-7, 123–127	4	Gray
30H-7, 20–22	2	Dark gray
363-U1483C-		
4H-2, 73–75	2	Dark gray
8H-3, 84–85	1	White
8H-4, 54–55	1	Gray
12H-2, 124–129	5	Dark gray
14H-6, 115–120	5	Gray
19H-6, 85–87	2	White
21H-6, 91–94	3	Gray

Discussion

Only one lithologic unit is defined at this site because the composition of the sediment does not change markedly throughout the sequence. To investigate clay mineral composition, we conducted XRD analysis of eight samples from the three different subunits. We analyzed the acidified residues from the samples previously analyzed for carbonate analysis (Figure **F16**). The results show differences in the proportions of clay minerals. A gradual decrease in the proportion of chlorite with depth suggests either changes in the source of the clay minerals, weathering processes, transportation of fine grains, and/or other processes relating to clay mineral deposition through the Pliocene–Pleistocene. The shipboard age model indicates a constant sedimentation rate of ~10 cm/ky for Subunits IA and IB (see **Biostratigraphy**), implying a relatively stable sedimentary environment at the site since the early Pleistocene. In contrast, multiple intervals of soft-sediment deformation in Subunit IC indicate sedimentary disturbances during the Pliocene to earliest Pleistocene. The erosional surfaces in some deformed intervals suggest depositional hiatuses in Subunit IC, which agrees with observations based on calcareous nannofossils and planktonic foraminifers (see **Biostratigraphy**).

Spectrophotometry data (L*, a*, b*) measured at 2.5 cm intervals on the archive halves from Holes U1483A–U1483C using the Section Half Multisensor Logger (SHMSL) show distinct meter-scale variations downhole. In particular, L* displays well-defined cyclicity with clear correlations between L* data across the three holes. Downhole variations in L* appear to track biogenic carbonate concentration in the bulk sediment with lighter colored, carbonate-rich intervals corresponding to higher L* measurements. The frequency of the L* cyclicity changes at ~82 mbsf, which may be associated with the mid-Pleistocene transition. Color reflectance a* and b* data

Figure F11. XRD results from selected bulk sediment samples in Subunit IB, Site U1483. A. Darker greenish gray sediment (U1483A-13H-1, 59–61 cm). B. Lighter greenish gray sediment (U1483A-13H-5, 39–41). C. Brownish gray sediment (U1483B-15H-2, 79–81 cm).

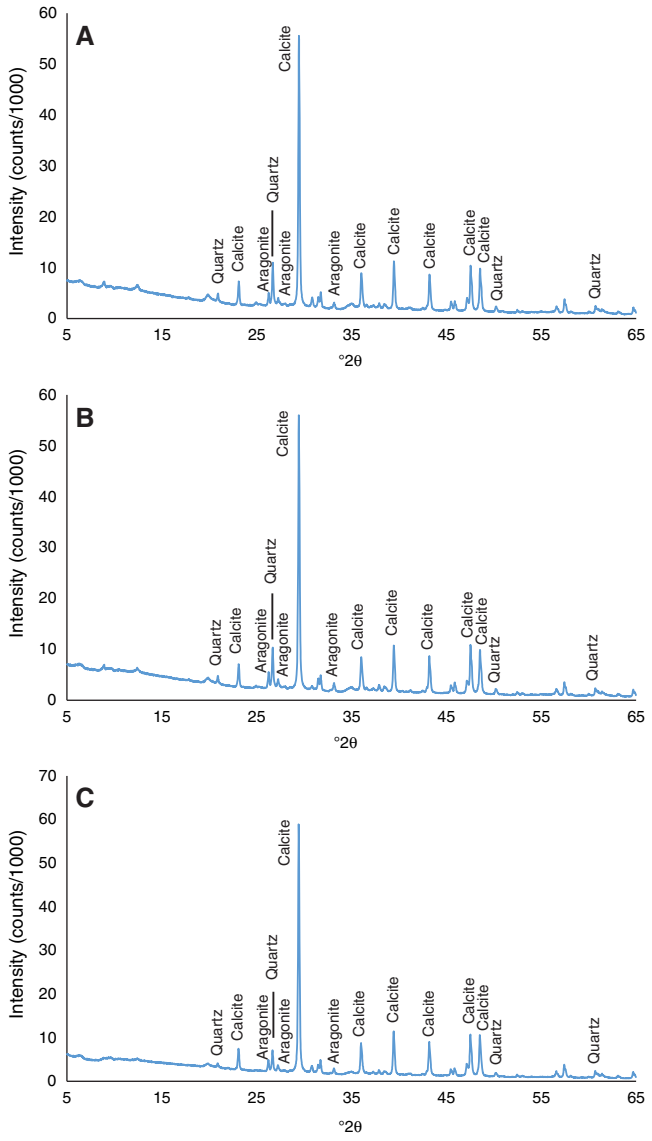

Figure F12. Characteristic lithology and color alternations in Subunit IA, Hole U1483A.

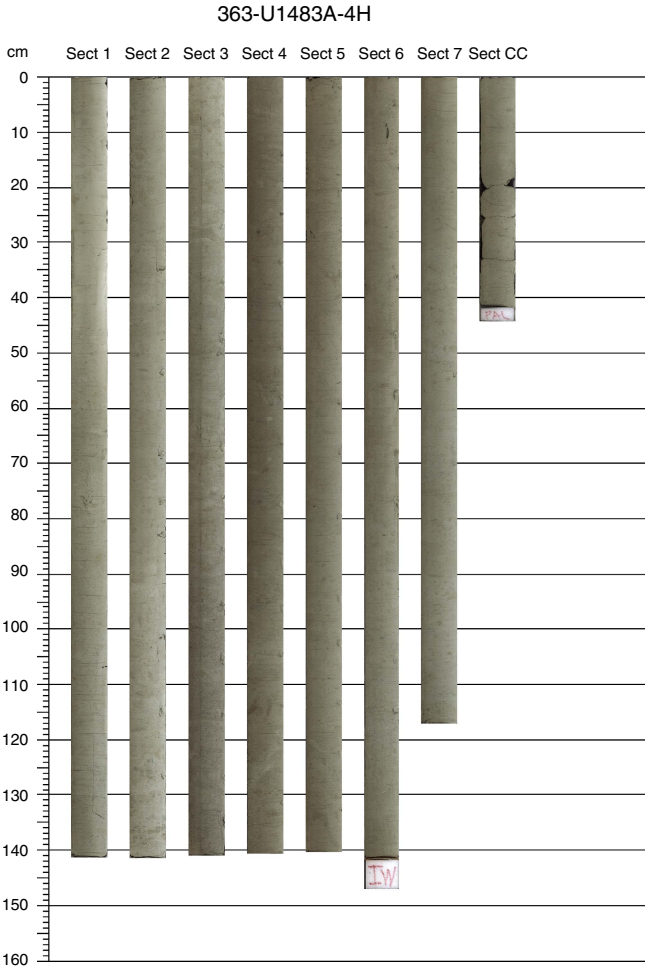

also display meter-scale variability, although the correlation between holes appears less consistent.

A relatively large portion of the sediment recovered in Subunit IC (as much as ~50 m in Hole U1483C) shows sediment deformation features including (1) "plastic" deformation such as inclined bedding and folding and (2) "brittle" deformation of the sediment fabric such as microfaulting and sediment foliation (Figure **F8**). The deformed sediment is concentrated in two intervals, with relatively undisturbed sediment in between. The two intervals record different types of deformation features, with plastic deformation primarily in the shallower interval and brittle deformation in the deeper interval, suggesting either multiple deformation events and/or a complex mechanism for sediment deformation that has disrupted and dislocated the originally undisturbed sediment after deposition. It is worth noting that thick clay layers were observed only in the disturbed intervals, suggesting a causal relationship between the occurrence of this lithology and the disturbance.

These disturbed intervals in Subunit IC contain mixtures of microfossil assemblages of different ages, and planktonic foraminifer biostratigraphy indicates probable hiatuses (see **Biostratigraphy**) of <200 ky for the shallower disturbed interval, whereas the hiatus is more significant in the deeper interval (~500 ky). By extrapolating the sedimentation rates from the undisturbed intervals, the total thickness of missing sediment can be estimated as ~100 m (see **Biostratigraphy**).

Based on sedimentologic and biostratigraphic observations, we suggest two possible mechanisms (not mutually exclusive) as potential cause(s) for the formation of these deformed intervals. The first hypothesis envisages the occurrence of two separate and unrelated events (at ~2.8 and ~2.1 Ma), which resulted in remobilization of sediment by mass gravity flow (e.g., slumping or debris flow) and concurrent soft-sediment deformation. Because of the presence of folded beds, the deformed sediment must have already experienced some degree of burial and early diagenesis (i.e., it was lithified enough to behave cohesively). According to this hypothesis, the sediment missing from Site U1483 must have slid and then accumulated in another location.

A second hypothesis interprets the two deformed intervals as the result of a single event that occurred at ~2.1 Ma. This hypothesis is based on the observation that the deeper disturbance (with the longer hiatus) shows the most evidence of brittle deformation,

Figure F13. Characteristic lithology and color alternations in Subunit IB, Hole U1483B.

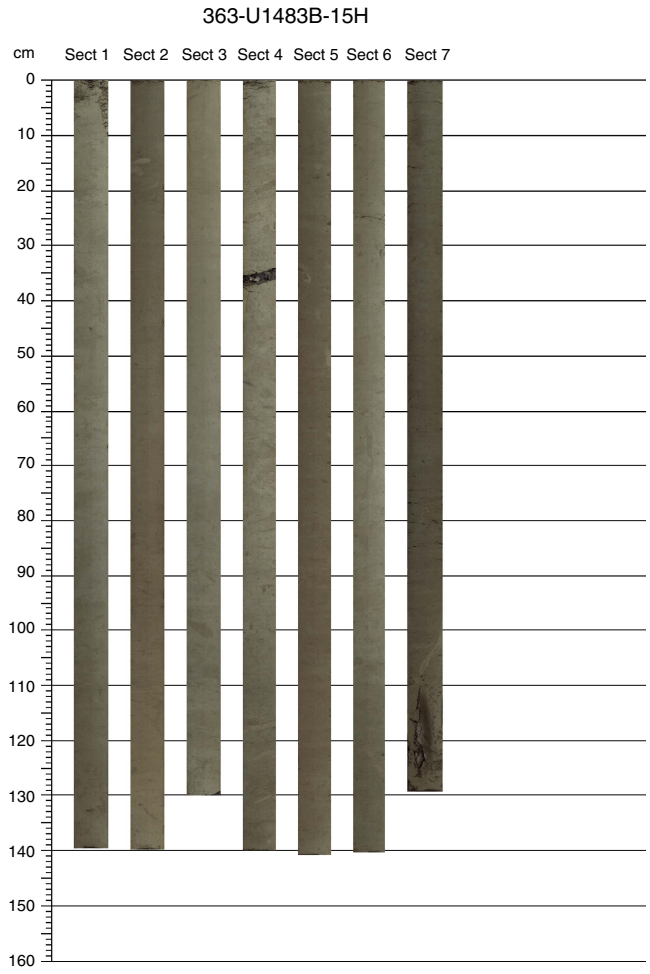

Figure F14. Mineral concretion (interval 363-U1483B-8H-7A, 62–65 cm). A. Core image. B. Close-up view.

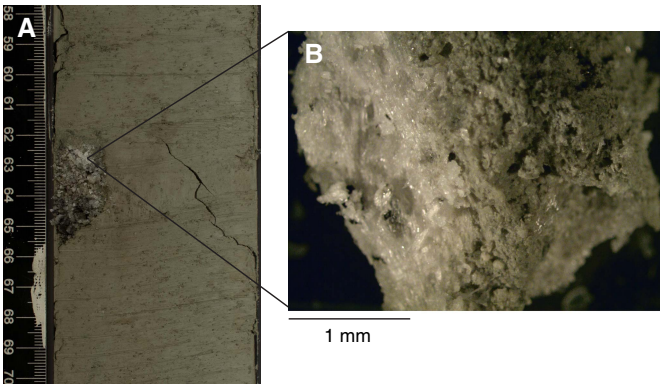

whereas the shallower disturbance exhibits mainly plastic deformation features. According to this hypothesis, the base of the lowermost disturbance acted as a "décollement" for one large detachment (either a submarine landslide and/or thrust fault) over which the entire interval encompassing the two disturbances slid, rafting relatively undisturbed sediment in between. The dark clay layers found as folded beds or dike-like structures within the disturbed interval could have facilitated the detachment. However, the biostratigraphic data suggest that the clay layers did not originate from a single layer prior to deformation (see **Biostratigraphy**).

This initial shipboard characterization does not allow us to establish which of the two hypotheses is most likely and whether the disturbances were formed during one or two events. However, the thickness of the sedimentary interval impacted by deformation and the potentially large amount of missing section indicate that the event(s) affected a large portion of the seafloor; therefore, this disturbance should be recorded in other locations. Site U1482 has a similar, although less extensive, disturbed portion of sediment dated to ~2 Ma, which might be correlative to the disturbed interval observed at Site U1483. Finally, the presence of clay beds in the deformed intervals indicates that clay lithologies occur at some depth at this site. This lithology is very different from the nannofossil ooze–dominated sediment recovered in the undisturbed sequence above the deformed intervals and represents a markedly different depositional environment that we have not documented.

Figure F15. Characteristic lithology and color alternations in Subunit IC, Hole U1483A.

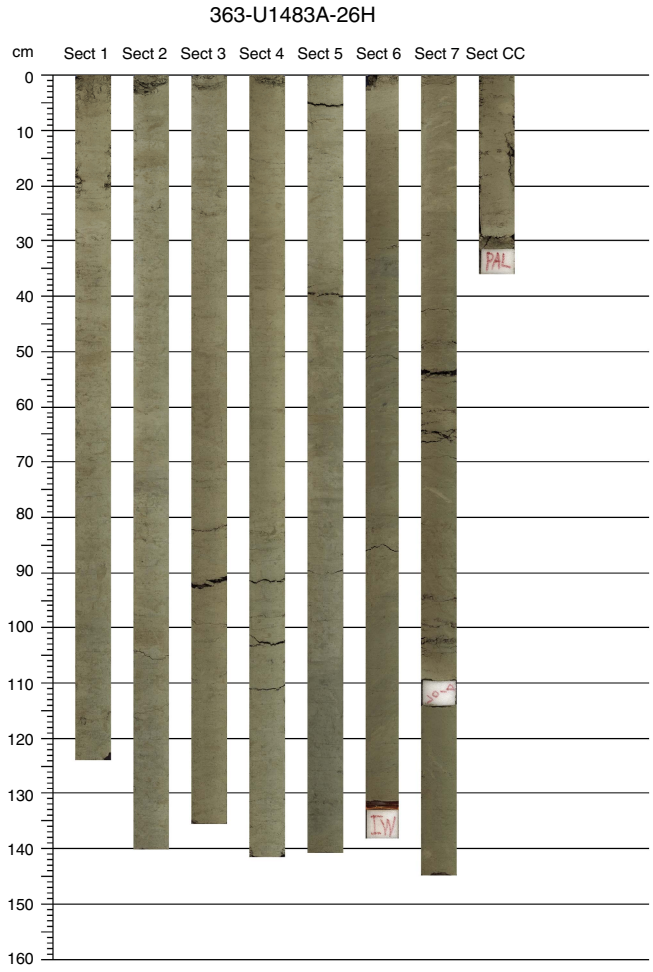

Figure F16. A. XRD results from carbonate residue analysis, Hole U1483A. B. Detail of 23°–28°2θ in A.

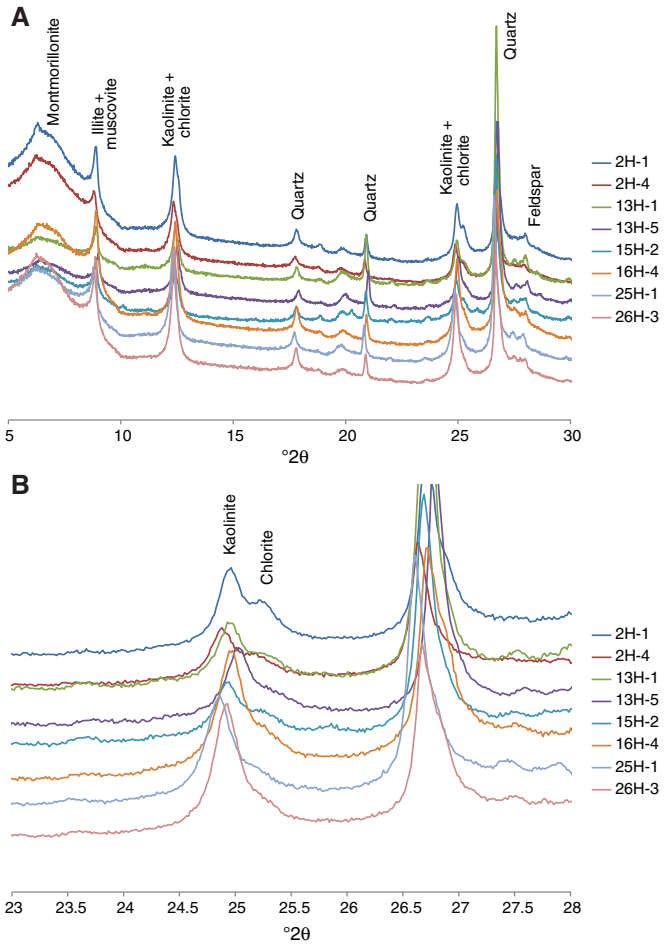

Biostratigraphy

Site U1483 recovered a 293 m thick sequence of lower Pliocene to Pleistocene clay, nannofossil clay, and nannofossil ooze, with varying proportions of diatoms and foraminifers (see **Core description**). Planktonic foraminifers, benthic foraminifers, and calcareous nannofossils are present throughout the succession. In the >150 µm size fraction, planktonic foraminifers are the dominant sediment component (>90% of particles). Radiolarians are present in many of the residues, particularly in samples taken from the diatom-rich subunits (see **Core description**). Although a minor decline in preservation with depth is noted in calcareous nannofossils, planktonic foraminifers, and benthic foraminifers, the preservation is generally excellent to very good for each group through the whole succession. The results from each fossil group (calcareous nannofossils, planktonic foraminifers, and benthic foraminifers) are presented in sections below, followed by a detailed characterization of both benthic and planktonic foraminifer preservation state using shipboard scanning electron microscope (SEM) observations. An integrated bio- and magnetostratigraphy is presented in the final section. Shipboard taxon occurrence data are available for download from the Laboratory Information Management System (LIMS) database (**http://web.iodp.tamu.edu/LORE**).

Calcareous nannofossils

Calcareous nannofossil biostratigraphy is based on analysis of core catcher samples and three additional samples from working-half sections (usually 50–52 cm in Sections 2, 4, and 6 of each core) in Hole U1483A, providing a sampling resolution of ~3 m. Depth positions and age estimates of key biohorizons are given in Table **T4**. Observations were undertaken using plane- (PPL), cross- (XPL), and circular-polarized light (CPL), as well as the shipboard desktop SEM (Hitachi TM3000) to confirm the presence of *Emiliania huxleyi* and to check preservation state.

At Site U1483, the preservation of calcareous nannofossils is generally excellent to very good. Intact coccospheres are frequently observed, and dissolution-susceptible taxa are consistently present (*Syracosphaera* and *Rhabdosphaera*). In the lower Pliocene, a thin central-area net is typically observed in specimens of *Reticulofenestra pseudoumbilicus* (XPL/CPL), whereas very small *Gephyrocapsa* spp. and *E. huxleyi* are abundant and well preserved in the middle to upper Pleistocene (SEM/CPL). When thin-rayed discoasters are present, some are fragmented but do not show any signs of overgrowth, with gracile ray-tip morphology and details of central-area bosses and knobs preserved (Figure **F17**). To determine the biohorizon top of *Discoaster brouweri*, we rely only on specimens that are not fragmented in order to avoid misinterpretation due to reworked discoasters that are often partly broken and/or recrystallized. Reworked calcareous nannofossils represent, in most instances, less than 1/10,000 of the assemblage. For example in Sample 363-U1483A-3H-2, 75 cm (20.34 mbsf), 20 reworked Cretaceous and Paleogene taxa are present in one slide transect (40 mm long) containing more than 100,000 calcareous nannofossils (estimated from 4 fields of view). The reworked taxa belong to the following genera: *Prediscosphaera, Watznaueria, Cretarhabdus, Micula, Sphenolithus,* and *Cyclicargolithus*. This amount of reworking persists throughout the hole, except at two levels (around 215 and 250 mbsf) where it significantly increases (see discussion below).

Calcareous nannofossil assemblages from Site U1483 are dominated by *Florisphaera profunda* (always extremely abundant) and the Noelaerhabdaceae (genera include *Gephyrocapsa, Emiliania, Pseudoemiliania*, and *Reticulofenestra*). In the Pleistocene succession, single Noelaerhabdaceae species often dominate within particular stratigraphic intervals, forming distinct, biostratigraphically useful acme events.

Pleistocene

The calcareous nannofossils provide a well-constrained biostratigraphy of the Pleistocene. Fourteen biohorizons have been identified with a sample resolution of about 1.5 m, and most of them are distributed along an age-depth line that indicates an almost constant sedimentation rate in the Pleistocene. The base of common *E. huxleyi* at 0.09 Ma occurs between Samples 363-U1483A-2H-2, 75 cm, and 2H-4, 75 cm (10.85–13.85 mbsf). This shift in abundance is well constrained, although *E. huxleyi* never dominates the assemblage. Besides *F. profunda*, *Gephyrocapsa oceanica* and *Gephyrocapsa ericsonii* are more abundant than *E. huxleyi*. The base of Zone NN21 is identified by biohorizon base *E. huxleyi* at 0.29 Ma between Samples 4H-2, 75 cm, and 4H-4, 75 cm (29.77–32.61 mbsf). The base of Zone NN20 is identified by biohorizon top *Pseudoemiliania lacunosa* (0.44 Ma) between Samples 5H-4, 75 cm, and 5H-6, 75 cm (42.08–44.90 mbsf). The base of Zone NN19 is identi-

Table T4. Calcareous nannofossil bioevents, Site U1483. B = base, T = top, Bc = base common, Ba = base acme, Ta = top acme. **Download table in CSV format.**

Bioevent number	Marker species	Age (Ma)	Zone base	Top core, section, interval (cm)	Bottom core, section, interval (cm)	Top depth (mbsf)	Bottom depth (mbsf)	Midpoint depth (mbsf)	± (m)
				363-U1483A-	363-U1483A-				
1	*Bc Emiliania huxleyi*	0.09		2H-2, 75	2H-4, 75	10.85	13.85	12.35	1.50
2	*Ta Gephyrocapsa caribbeanica*	0.28		4H-2–75	4H-4, 75	29.77	32.61	31.19	1.42
3	*B Emiliania huxleyi*	0.29	NN21	4H-2–75	4H-4, 75	29.77	32.61	31.19	1.42
4	*T Pseudoemiliania lacunosa*	0.44	NN20	5H-4, 75	5H-6, 75	42.08	44.90	43.49	1.41
5	*Ba Gephyrocapsa caribbeanica*	0.60		5H-CC	6H-CC	47.03	56.48	51.76	4.72
6	*T Reticulofenestra asanoi*	0.91		9H-6, 50	9H-CC	82.64	84.76	83.70	1.06
7	*Bc Reticulofenestra asanoi*	1.14		12H-2, 50	12H-4, 50	105.56	108.53	107.05	1.49
8	*T Gephyrocapsa >5.5 µm*	1.25		12H-4, 50	12H-6, 50	108.53	111.50	110.02	1.49
9	*T Helicosphaera sellii*	1.26		14H-2, 50	14H-4, 50	124.56	127.43	126.00	1.44
10	*T Calcidiscus macintyrei*	1.60		16H-4, 50	16H-6, 50	146.42	149.24	147.83	1.41
11	*T Discoaster brouweri*	1.93	NN19	19H-CC	20H-2, 50	180.06	181.51	180.79	0.72
12	*T Discoaster triradiatus*	1.95		19H-CC	20H-2, 50	180.06	181.51	180.79	0.72
14	*T Discoaster pentaradiatus*	2.39	NN18	23H-CC	24H-2, 50	217.97	219.44	218.71	0.73
15	*T Discoaster surculus*	2.49	NN17	24H-CC	25H-2, 51	227.88	229.01	228.45	0.56
	Pliocene/Pleistocene boundary	2.58							
16	*T Discoaster tamalis*	2.80		26H-CC	27H-2, 50	246.66	248.00	247.33	0.67
17	*T Sphenolithus spp.*	3.54		29H-CC	30H-2, 50	274.97	276.53	275.75	0.78
18	*T Reticulofenestra pseudoumbilicus*	3.70	NN16	31H-2, 50	31H-5, 50	285.95	288.82	287.39	1.44

Figure F17. Calcareous nannofossils, Hole U1483A. A, B. *Calcidiscus macintyrei* (31H-CC). C. *Ceratolithus cristatus* (24H-CC). D. *Coccolithus pelagicus* (24H-CC). E. *Florisphaera profunda* (18H-CC). F, G. *Gephyrocapsa oceanica*; (F) 2H-CC; (G) 8H-2, 50 cm. H. *Helicosphaera carteri* (30H-CC). I. *Pontosphaera discopora* (10H-CC). J, K. *Pseudoemiliania lacunosa* (10H-CC). L. *Reticulofenestra asanoi* (9H-6, 50 cm). M. *Reticulofenestra pseudoumbilicus* (31H-CC). N. *Sphenolithus abies* (31H-CC). O. *Umbilicosphaera sibogae* (18H-CC). P. *Discoaster asymmetricus* (31H-CC). Q. *Discoaster brouweri* (31H-CC). R. *Discoaster variabilis* (3-rayed form) (31H-CC). S. *Discoaster variabilis* (31H-CC). T. *Discoaster variabilis* (4-rayed form) (9H-4, 50 cm). All photos are at same magnification (scale bar in A).

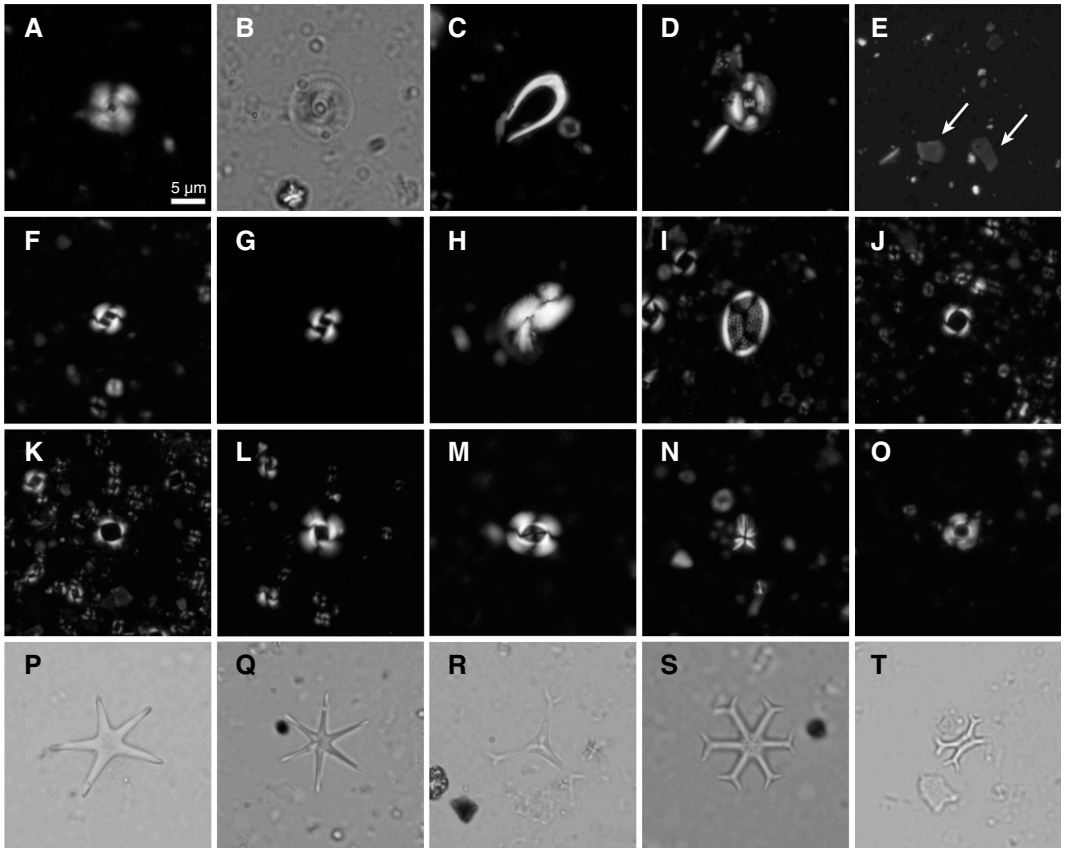

fied by biohorizon top *D. brouweri* (1.93 Ma) between Samples 19H-CC and 20H-2, 50 cm (180.06–181.51 mbsf). This bioevent occurs ~10 m above a sharp drop in the abundance of discoasters between Samples 20H-CC and 21H-2, 51 cm (189.62–191.02 mbsf). Below this interval, the abundance of *D. brouweri* is similar to that of the reworked discoasters. Specimens of *D. brouweri* are considered in place when they have complete and well preserved rays.

Calcareous nannofossil biostratigraphy of the lower Pleistocene is complicated by reworking in an interval of disturbed sediment between Cores 21H and 23H (see **Core description**). Immediately above this disturbance (Sample 21H-4, 17 cm; 193.51 mbsf), the sediment age is constrained to >1.93 Ma by the consistent presence of *D. brouweri*. Twelve samples studied within this interval show variable abundances of species indicative of a component of significantly older, early Pliocene specimens, including *Sphenolithus abies* and *Reticulofenestra pseudoumbilicus*. In Cores 21H and 22H, the darker clay-rich clasts and horizons contain the greatest proportion of these early Pliocene taxa (Samples 21H-4, 82 cm, and 22H-2, 60 cm; 194.16 and 200.62 mbsf, respectively). Below the most heavily deformed intervals of Cores 21H and 22H, biohorizon top *Discoaster pentaradiatus* (2.49 Ma) is placed between Samples 23H-CC and 24H-2, 50 cm (217.97–219.44 mbsf), based on a marked increase in the abundance of this taxon, and a shift from fragmented forms, to more intact specimens. Given the intensity of reworking through this interval, this placement is somewhat uncertain. To trace the presence of reworking and disturbed, possibly mixed sediment, the abundance of *Sphenolithus abies* was quantified against the abundance of discoasters and *Helicosphaera* (Figure **F18**). In the upper Pliocene to lower Pleistocene interval of sediment disturbance, *S. abies* should be completely absent and so its presence in the sediment can be used to trace the presence of reworked early Pliocene material. This guides the interpretation of assemblages near the final extinction of the discoasters, where it is hard to distinguish primary discoaster assemblages from reworked, and so place biohorizon tops of *D. pentaradiatus*, *D. triradiatus*, and *D. brouweri*. It is important to note that below and above the disturbed sequence, reworked *S. abies* specimens are absent, and the calcareous nannofossil biohorizons are found in correct stratigraphic order. The biohorizon top *Discoaster surculus* (2.49 Ma) marks the base of Zone NN17 and occurs between Samples 24H-CC and 25H-2, 51 cm (227.88–229.01 mbsf).

Pliocene

The recovered Pliocene interval is 65 m thick and corresponds to Zone NN16, between biohorizon top *D. surculus* and biohorizon top *R. pseudoumbilicus* at 3.70 Ma, which marks the base of Zone NN16. The latter bioevent is found between Samples 363-U1483A-31H-2, 50 cm, and 31H-5, 50 cm (285.95–288.82 mbsf). The Pliocene calcareous nannofossil biohorizons, when shown as age-depth plots, are not aligned along the constant sedimentation rate of the Pleistocene. They rather indicate a substantially lower sedimentation rate or an unconformity. The abundance of reworked specimens of *S. abies* in the interval from Samples 26H-6, 50 cm (243.99 mbsf), to 27H-4, 50 cm (250.85 mbsf), indicates another disturbed interval, similar to the one identified at the base of Zone NN18 (~194–203 mbsf) (Figure **F18**).

Planktonic foraminifers

The most detailed planktonic foraminifer biostratigraphy was conducted in Hole U1483A, from which the core catcher sample and three additional samples per core were taken. Foraminifers occur throughout the sediment but are sometimes found concentrated in certain horizons and burrows. A mudline sample taken in Hole U1483A contains a recent, diverse, tropical assemblage, which is generally excellently preserved although minor iron oxide staining is evident on some tests.

Figure F18. Relative abundance of the *Discoaster*, *Helicosphaera*, and *Sphenolithus* based on 50–150 individuals, Site U1483. Red circles mark depth of analyzed samples.

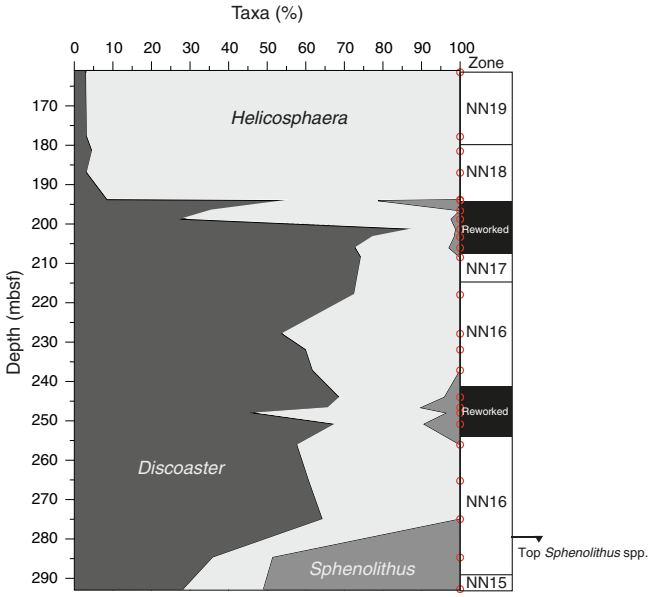

Pleistocene

Sample 363-U1483A-1H-2, 75–77 cm (2.25 mbsf), is assigned to the uppermost part of Subzone Pt1b (<0.07 Ma) based on the absence of *Globigerinoides ruber* (pink) and *Globorotalia flexuosa*. Biohorizon base *Globigerinella calida* has a calibrated age of 0.22 Ma (Wade et al., 2011); however, this morphospecies is found deeper in the section than expected and is present in Sample 6H-6, 50–52 cm (54.20 mbsf), below biohorizon base *G. flexuosa* (found between Samples 5H-7, 50–52 cm, and 5H-CC; 44.65–47.03 mbsf), which has an older calibrated age of 0.40 Ma. Detailed investigation at other sites is required to determine whether there is a need for bioevent recalibration or whether this is a local discrepancy.

A single sample contains numerous *Globigerinoides* sp. cf. *conglobatus* (pink) (Sample 363-U1483A-9H-2, 50–52 cm; 77.0 mbsf) (see **Biostratigraphy** in the Site U1482 chapter [Rosenthal et al., 2018b] for discussion of morphological characteristics). This correlates well with the short stratigraphic interval at Site U1482 (Samples 363-U1482B-5H-6, 49–51 cm, and 5H-CC; 42.59–44.54 mbsf) with similar *G.* sp. cf. *conglobatus* (pink), providing a useful tie point between the two sites. Both occurrences are found slightly below the base of Subzone Pt1b (black star in Figure **F19**) suggesting more widespread correlation potential.

Biohorizon top *Globorotalia tosaensis* (0.61 Ma), marking the base of Subzone Pt1b, is found between Samples 363-U1483A-8H-4, 50–52 cm, and 8H-6, 50–52 cm (70.36–73.16 mbsf). This biohorizon is difficult to locate precisely during shipboard studies because many individuals need to be examined closely to find the top occurrence, and intergradation between *G. tosaensis* and *Globorotalia truncatulinoides* is common.

Saito's (1976) L1 excursion of sinistral *Pulleniatina* occurs between Samples 363-U1483A-9H-2, 50–52 cm, and 9H-4, 50–52 cm (77.00–79.82 mbsf), just below the level with *G.* sp. cf. *conglobatus* (pink) (Table **T5**; Figure **F19**). Previous work (figure 2 in Saito, 1976) has shown that the L1 "event" is closely associated with the

Matuyama/Brunhes magnetochron boundary (0.781 Ma), although it is not clear on which side of the boundary the event falls. The bioevent has previously been calibrated approximately to 0.80 Ma based on low-resolution sampling (Wade et al., 2011). The Matuyama/Brunhes boundary in Hole U1483A is located at 80.60 mbsf (see **Paleomagnetism**). The downhole transition between dominantly dextral and sinistral populations is located within the lowermost part of the Brunhes magnetochron, whereas the downhole return to dextral values is within the uppermost Matuyama magnetochron.

Figure F19. Coiling patterns in *Pulleniatina*, Hole U1483A.

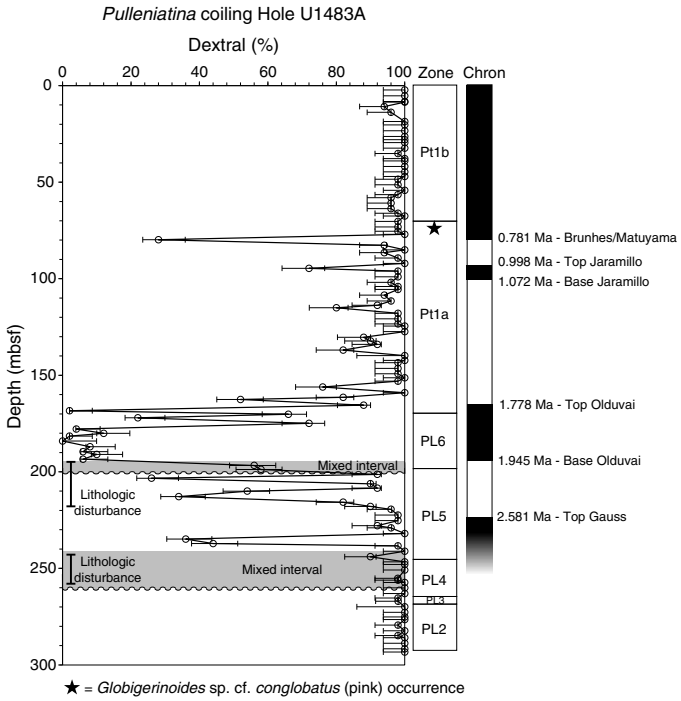

Biohorizon top *Globigerinoidesella fistulosa* (1.88 Ma), marking the base of Subzone Pt1a, is found between Samples 363-U1483A-17H-6, 49–51 cm, and 17H-CC (159.07–161.45 mbsf). Individuals of *G. fistulosa* are rare close to this biohorizon, but very distinctive and continuously present.

An interval of severe disturbance topped by a prominent ash layer was observed in Cores 363-U1483A-21H and 23H. Two samples were taken in Core 21H above the interval of disturbance, Samples 21H-2, 50–52 cm, and 21H-4, 16–18 cm (191.01 and 193.50 mbsf, respectively), the latter taken 20 cm above the first visible disturbance. These samples contain *G. fistulosa* and *Pulleniatina finalis* but no *Globigerinoides extremus* and are assigned to the upper part of Zone PL6 (corresponding to 1.98–2.04 Ma). Note that a single specimen of *Globorotalia limbata* in Sample 21H-2, 50–52 cm (191.01 mbsf), is interpreted as reworked. Both samples lack *G. truncatulinoides*, although that is interpreted as being due to the rarity of that marker, which also has an uncertain age calibration in the Indian Ocean and appears to be diachronous. Sample 22H-2, 130–132 cm (201.32 mbsf), was taken from about 20 cm below the disturbed interval. This contains a set of top biohorizon markers (disregarding the biostratigraphically mixed interval immediately above it, which is described below) that indicate a substantially older age: *G. extremus* (>1.98 Ma), *Globorotalia pseudomiocenica* (>2.30 Ma), and frequent *G. limbata* (>2.39 Ma). The absence of *P. finalis* and presence of rare *G. fistulosa, G. tosaensis*, and *G. truncatulinoides* locate this sample, and those that follow immediately below it, to the middle part of Zone PL5 (corresponding to 2.39–3.33 Ma). Within the disturbed interval itself, two samples were studied, Samples 21H-6, 50–52 cm, and 21H-CC (196.72 and 198.79 mbsf, respectively). These assemblages appear mixed, containing elements of both older material (including *G. pseudomiocenica* and *G. limbata*) and younger material (*P. finalis*). Coiling ratios of *Pulleniatina* in the disturbed interval are approximately 55% dextral,

Table T5. Planktonic foraminifer bioevents, Site U1483. * = calibration follows Dowsett (1988), † = calibration follows Chaisson and Pearson (1997), ‡ = calibration follows Berggren et al. (1995). B = base, T = top, X = coiling reversal, s = sinistral, d = dextral. **Download table in CSV format.**

Bioevent number	Event	Age (Ma)	Zone base	Top core, section, interval (cm)	Bottom core, section, interval (cm)	Top depth (mbsf)	Bottom depth (mbsf)	Midpoint depth (mbsf)	± (m)
				363-U1483A-	363-U1483A-				
1	T *Globorotalia flexuosa*	0.07		1H-4, 75-77	1H-6, 75–77	5.25	8.25	6.75	1.50
2	T *Globigerinoides ruber* (pink)	0.12		1H-CC	2H-2, 74–76	8.58	10.84	9.71	1.13
3	B *Globigerinella calida*	0.22		6H-6, 50–52	6H-CC	54.20	56.48	55.34	1.14
4	B *Globorotalia flexuosa*	0.40		5H-7, 50–52	5H-CC	44.65	47.03	45.84	1.19
6	T *Globorotalia tosaensis*	0.61	Pt1b	8H-4, 50–52	8H-6, 50–52	70.36	73.16	71.76	1.40
8	X *Pulleniatina* s to d "L1"	0.80		9H-2, 50–52	9H-4, 50–52	77.00	79.82	78.41	1.41
11	T *Globigerinoidesella fistulosa*	1.88	Pt1a	17H-6, 49–51	17H-CC	159.07	161.45	160.26	1.19
13	T *Globigerinoides extremus*	1.98		21H-4, 16–18	21H-6, 50–52	193.50	196.72	195.11	1.61
14	B *Pulleniatina finalis*	2.04		21H-CC	22H-2, 130–132	198.79	201.32	200.06	1.27
17	T *Globorotalia pseudomiocenica*	2.30	PL6	21H-4, 16–18	21H-6, 50–52	193.50	196.72	195.11	1.61
18	T *Globorotalia limbata*	2.39		21H-4, 16–18	21H-6, 50–52	193.50	196.72	195.11	1.61
12	B *Globorotalia truncatulinoides*	2.47*		23H-6, 50–52	23H-CC	215.77	217.97	216.87	1.10
	Pliocene/Pleistocene boundary	2.58							
23	T *Dentoglobigerina altispira*	3.13†	PL5	26H-4, 50–52	26H-6, 50–52	241.42	243.99	242.71	1.28
21	B *Globigerinoidesella fistulosa*	3.33		28H-2, 49–51	28H-4, 49–51	257.31	260.13	258.72	1.41
22	B *Globorotalia tosaensis*	3.35		27H-2, 50–52	27H-4, 50–52	248.00	250.85	249.43	1.43
25	T *Sphaeroidinellopsis seminulina*	3.59	PL4	28H-CC	29H-2, 49–51	265.32	266.99	266.16	0.83
28	T *Globorotalia margaritae*	3.60‡	PL3	29H-2, 49–51	29H-4, 49–51	266.99	269.91	268.45	1.46
29	X *Pulleniatina* s to d "L9"	4.08		31H-CC	Below hole	>293.32			

Table T6. Coiling count data for *Pulleniatina*, Hole U1483A. **Download table in CSV format.**

whereas the sediment above is <10% dextral and below is >90% dextral (Tables **T5**, **T6**; Figure **F19**). This may indicate thorough mixing between these two extremes on a grain by grain level or that an interval of mixed coiling existed in a missing time interval from which sediment has been redeposited. A summary of this evidence, considered in conjunction with nannofossil and other information, is presented in **Shipboard age model**.

Pliocene

Biohorizon base *G. truncatulinoides* is found between Samples 363-U1483A-23H-6, 50–52 cm, and 23H-CC (215.77–217.97 mbsf). As at Site U1482, this biohorizon is clearly within the upper part of the range of *G. pseudomiocenica* and *G. limbata*, implying that its correct calibration in this area is >2.39 Ma, as previously discussed (see **Biostratigraphy** in the Site U1482 chapter [Rosenthal et al., 2018b]). A local calibration of 2.47 Ma is adopted for both Indian Ocean sites following Dowsett (1988).

A second downcore interval of significant disturbance was found extending from the lower part of Section 363-U1483A-26H-5 through Section 28H-2 (see **Core description**). The sample above this, 26H-4, 50–52 cm (243.99 mbsf), contains the following markers: *G. pseudomiocenica* (indicating >2.30 Ma), *G. limbata* (>2.39 Ma), *G. fistulosa* (<3.33 Ma), and *G. tosaensis* (<3.35 Ma). Missing from the assemblages is the distinctive and generally frequent species *Dentoglobigerina altispira* (indicating <3.13 Ma based on the preferred Atlantic calibration; see **Biostratigraphy** in the Site U1482 chapter [Rosenthal et al., 2018b]). Hence, the age of the sediment above the disturbed interval is bracketed in the range 2.39–3.13 Ma. This is biostratigraphically similar to the level below the shallower interval of sediment disturbance discussed above, except for the absence of *G. truncatulinoides*, for which the age calibration is uncertain. The first sample below the disturbed interval, 28H-4, 49–51 cm (260.13 mbsf), contains *D. altispira*, the marker for Zone PL4 (indicating >3.13 Ma), in the absence of *G. fistulosa* (>3.33) and *G. tosaensis* (>3.35). The upper age limit for this sample is constrained by the absence of *Sphaeroidinellopsis seminulina* (indicating <3.59 Ma) and *Globorotalia margaritae* (<3.85 Ma). Hence, the age of the sediment below the disturbed interval appears to be in the range 3.35–3.59 Ma. Within the disturbed interval, seven samples were studied: 363-U1483A-26H-6, 50–52 cm (243.99 mbsf); 26H-CC (246.66 mbsf); 27H-2, 50–52 cm (248.00 mbsf); 27H-4, 50–52 cm (250.85 mbsf); 27H-7, 50–52 cm (255.16 mbsf); 27H-CC (256.70 mbsf); and 28H-2, 49–51 cm (257.31 mbsf). Interestingly, these samples are not homotaxial. The distinctive *G. fistulosa* and *D. altispira* can be used to identify relatively older and younger components; the former occurs only in the upper two samples studied from the disturbed interval, whereas the latter occurs throughout except in Sample 26H-CC (246.66 mbsf). *Pulleniatina* coiling is strongly dextral, as it is above and below the disturbed interval (Figure **F19**).

Within the disturbed interval are some prominent clay-rich layers (see **Core description**). Four additional samples from Hole U1483C were taken from these layers to test the hypothesis that the clay could have been from a single stratigraphic layer prior to deformation and may have acted as a décollement surface for downslope mass transport. Sample 363-U1483C-24H-3, 116–118 cm (212.72 mbsf), is excellently preserved and contains *G. truncatulinoides, P. finalis, G. fistulosa, G. pseudomiocenica*, and *G. limbata* but no *D. altispira* and therefore is assigned to Zone PL5 (2.39–3.13 Ma). Sample 29H-3, 34–36 cm (259.52 mbsf), has very good to good preservation with large amounts of pyrite in the residue and contains *D. altispira* in the absence of *S. seminulina*. It is therefore assigned to Zone PL4 (3.13–3.59 Ma), although a small component of younger material appears to have been mixed with it as evidenced by single specimens of *P. finalis* and *G. truncatulinoides*. Sample 29H-7, 47–49 cm (265.44 mbsf), has very good preservation and is also assigned to Zone PL4 (3.13–3.59 Ma) with no apparent evidence of mixing. Sample 31H-5, 70–72 cm (281.21 mbsf), has excellent preservation and contains *D. altispira* and several very well preserved specimens of *G. margaritae* but no *Globoturborotalita nepenthes*; it is assigned to Zone PL2. *Pulleniatina* coiling is dextral, so it probably belongs to the upper part of this zone (3.60–4.08 Ma). From these observations, it is clear that the clay layers did not originate from a single layer prior to deformation. This evidence is discussed further in conjunction with the nannofossil and paleomagnetic evidence in **Shipboard age model**.

Biohorizon top *S. seminulina* (3.59 Ma), denoting the base of Zone PL4, occurs between Samples 363-U1483A-28H-CC and 29H-2, 49–51 cm (265.32–266.99 mbsf). Problems with the calibration of biohorizon top *G. margaritae* were discussed for Site U1482 (see **Biostratigraphy** in the Site U1482 chapter [Rosenthal et al., 2018b]). In Hole U1483A this biohorizon, which denotes the base of Zone PL3, occurs between Samples 29H-2, 49–51 cm (266.99 mbsf), and 29H-4, 49–51 cm (269.91 mbsf), hence a very short stratigraphic interval corresponding to Zone PL3 implied by our preferred calibration (3.60 Ma following Berggren et al., 1995) appears to be present at this site. No further biohorizons were identified down to the lowermost sample examined, Sample 31H-CC (293.32 mbsf).

Table T7. Benthic foraminifer distribution, Hole U1483A. **Download table in CSV format.**

Benthic foraminifers

Benthic foraminifers were studied from assemblages recovered in all core catcher samples from Hole U1483A. The planktonic:benthic foraminifer ratio is about 99:1 throughout the hole. Calcareous and agglutinated benthic foraminifers occur in all core catcher samples at this site, with the recorded abundance of species and generic groups for each sample shown in Table **T7**. The assemblages are dominated by calcareous forms, with lower abundances of agglutinated forms; the latter typically represent <5% of the assemblages. The most common species are *Pyrgo* spp., *Laevidentalina* spp., *Uvigerina* spp., *Planulina wuellerstorfi*, and *Hoeglundina elegans*. The epifaunal species *P. wuellerstorfi* is recorded in all samples, but its abundance is generally low. The infaunal genus *Uvigerina* is also present in most samples, except for Samples 363-U1483A-12H-CC (113.76 mbsf), 13H-CC (123.39 mbsf), 15H-CC (142.27 mbsf), 22H-CC (208.47 mbsf), and 30H-CC (284.81 mbsf). Within samples, the generic diversity ranges from 10 to 26 (Table **T7**). The highest species diversity is found in Sample 10H-CC (94.60 mbsf) and the lowest diversity in Sample 20H-CC (189.57 mbsf). Paleodepth estimates generated from benthic foraminifer genera and species indicate a bathyal bathymetric zone. Tests are very well preserved with rare to no evidence of abraded tests (see **Foraminifer preservation**).

Foraminifer preservation

Four core catcher samples from Hole U1483A were selected to assess foraminifer preservation and diagenesis. The samples are spaced at ~90 m intervals and range in age from late Pleistocene (~0.1 Ma) to early Pliocene (~4.0 Ma). Foraminifer preservation is generally excellent and glassy, possibly due to the relatively clay rich

Figure F20. Downcore foraminifer preservation states, Site U1483. A. Light microscope images to assess the extent of fragmentation and staining and whether the tests are glassy or opaque. B. SEM images of *T. trilobus* and *P. wuellerstorfi* as whole tests, umbilical side upward. C. High-magnification images of outer wall surfaces to examine additional features such as spine holes, pustules, etc. D. High-magnification images of wall cross sections to find original microgranules or diagenetic crystallites. E. High-magnification images of inner wall surfaces, focusing on evidence for internal overgrowth and cementation.

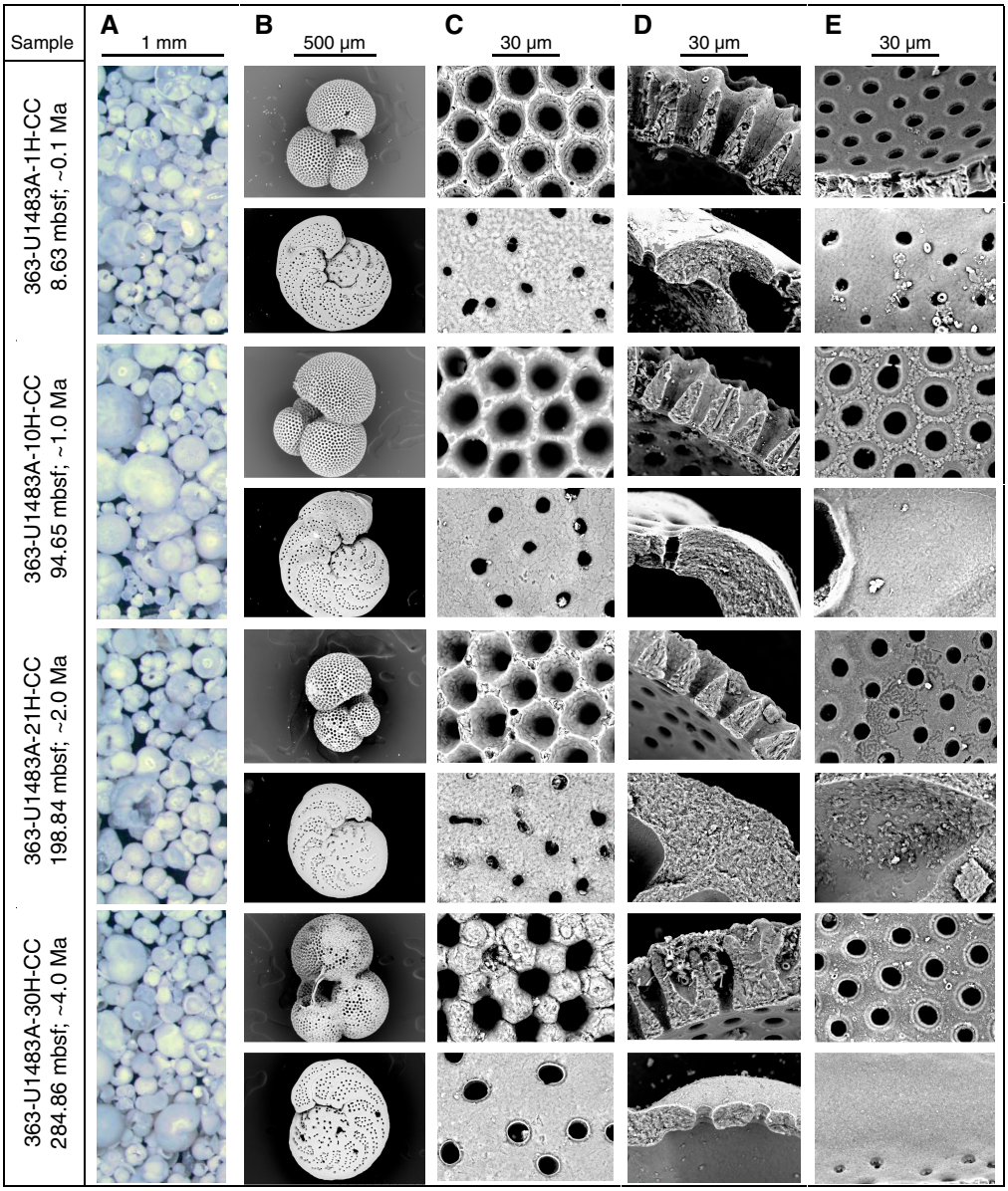

sediment as at Site U1482 (see **Biostratigraphy** in the Site U1482 chapter [Rosenthal et al., 2018b]). However, there is evidence for minor dissolution on the outer walls of some planktonic foraminifer specimens, even at very shallow depth. Minor calcite overgrowth becomes progressively more evident at greater depth, but no recrystallization and cementation is observed, even in the deepest part of the stratigraphy. Images of selected specimens are shown in Figure **F20**. The full set of images is available online from the Laboratory Information Management System (LIMS) database (**http://web.iodp.tamu.edu/LORE**).

Sample 363-U1483A-1H-CC (8.58 mbsf; late Pleistocene; ~0.1 Ma) shows excellent preservation. Foraminifers have a glassy appearance under the light microscope. In cross section, the wall of *Trilobatus trilobus* shows the platy microgranules typical of the species, and in some specimens spines embedded in the wall and the distinctive texture of the gametogenic crust was also observed. Minor superficial etching of the outer chamber surfaces of some specimens, especially the interpore ridges, suggests some dissolution. The wall cross section of *P. wuellerstorfi* shows microgranules throughout. The inner wall surface of both species is smooth. There is no evidence of recrystallization, overgrowth, infilling, or cementation.

Sample 10H-CC (94.60 mbsf; latest early Pleistocene; ~1.0 Ma) shows excellent preservation. Foraminifers have a glassy appearance under the light microscope. Wall cross sections of both *T. trilobus* and *P. wuellerstorfi* show the biogenic microgranular textures typical of the species. *T. trilobus* shows embedded spines and gametogenic calcite in some specimens, and the outer wall shows very

Figure F21. Age-depth plot for Site U1483 showing integrated biomagnetochronology in Hole U1483A. Average sedimentation rates are ~10 cm/ky. Two disturbed intervals (shaded boxes) are associated with intervals of mixed planktonic foraminifer (PF) assemblages, calcareous nannofossil reworking, and lithologic disturbance. Biohorizon numbers correspond to those given in Tables T4 and T5.

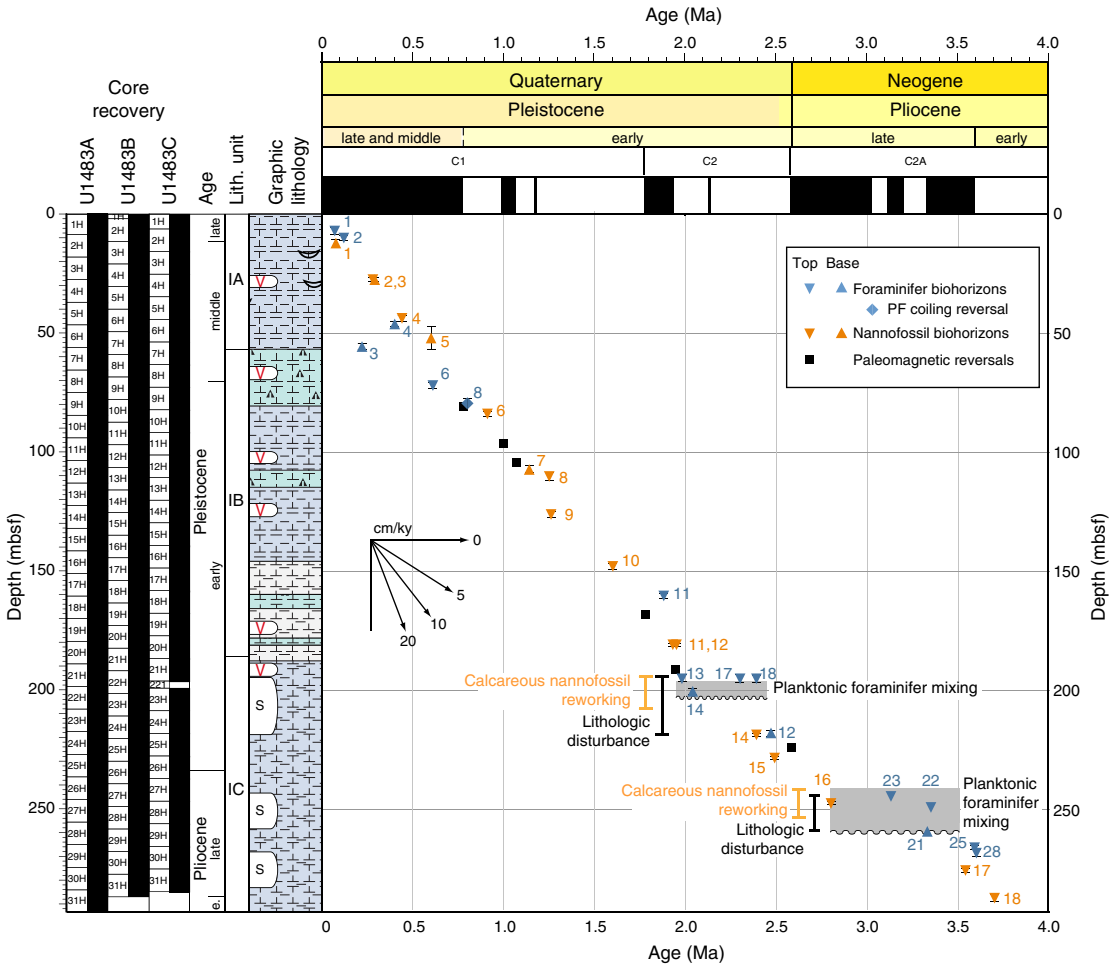

minor evidence of dissolution. The inner wall surface of both species is generally smooth with minor overgrowth. There is no evidence of recrystallization, infilling, or cementation.

Sample 21H-CC (198.79 mbsf; early Pleistocene; ~2.0 Ma) shows excellent preservation. Foraminifers have a glassy appearance under the light microscope. Wall cross sections of both *T. trilobus* and *P. wuellerstorfi* show biogenic microgranular textures. *T. trilobus* shows embedded spines and gametogenic calcite, and the outer walls show evidence of minor dissolution. The inner wall surface of both species is generally smooth. Some specimens show minor overgrowth of calcite crystals on the test.

Sample 30H-CC (284.81 mbsf; early Pliocene; ~4.0 Ma) shows excellent preservation. Foraminifers have a glassy appearance under the light microscope. Wall cross sections of both *T. trilobus* and *P. wuellerstorfi* show biogenic microgranular textures. *T. trilobus* shows embedded spines in the wall cross section. The outer wall surface of some *T. trilobus* specimens show stronger evidence of dissolution etching than is present in shallower samples. Inner wall surfaces are generally smooth but usually show minor overgrowth of radially directed calcite crystals forming a layer about 1 µm thick. There is no evidence of recrystallization or cementation.

Shipboard age model

An age-depth plot including all biostratigraphic biohorizons and magnetostratigraphic horizons (see **Paleomagnetism**) is shown in Figure **F21**. Sedimentation rates through the middle to late Pleistocene were relatively high and constant at ~10 cm/ky, although this may have varied during shorter-term climate cycles. Calcareous nannofossil and planktonic foraminifer biohorizons show good agreement throughout this interval down to the middle part of Core 363-U1483A-21H (193.50 mbsf). The base of the hole is assigned an early Pliocene age, older than 3.70 Ma, based on the presence of *Reticulofenestra pseudoumbilicus*.

Below 193.5 mbsf the stratigraphy is more disturbed, which includes biostratigraphic evidence (see especially **Planktonic foraminifers**) for two hiatuses, one minor and one of longer duration, above which there is physical mixing of different aged components. These biostratigraphically mixed intervals correspond to pulses of reworking of the late Pliocene species *Sphenolithus abies* into younger aged sediment (see **Calcareous nannofossils**) and severe disturbance in the sedimentary fabrics (see **Core description**). The intervals of microfossil mixing and reworking are shown on Figure **F21**, alongside the extent of lithologic disturbance. The age-depth

plot shows the downhole trend in sediment age above and below the disturbed intervals. From this it can be inferred that there is likely a relatively short hiatus at the base of the top mixed interval (<200 ky) but a more significant hiatus at the base of the bottom mixed interval (with ~500 ky missing).

To reconcile all our observations with the evidence from core description we offer two alternative models. In the first model, the hiatuses represent erosional disconformities that were formed in the early phases of energetic downslope mass transport events which then deposited the biostratigraphically mixed sediment above them. Within each mixed interval, more sediment was stripped off at this site (and presumably exported downslope) than was deposited (presumably from upslope). The mass transport events would have occurred at ~2.8 Ma, producing the lower hiatus and mixed interval, and at ~2.1 Ma, producing the upper one. There may also have been other such events that produced disturbed sedimentary fabrics that were not resolved by our biostratigraphic data. The lower disturbed interval, in particular, could be a composite of more than one mass movement event because the biostratigraphically mixed sediment within it has older components in the lower part and younger, but still mixed, components in the upper part. The sediment between the disturbed intervals (~205–240 mbsf), which includes several biohorizons and the top Gauss magnetic reversal (226.15 mbsf), represents more coherent stratigraphy.

In the second model (see **Core description**) all of the observed disturbance at the site could be related to a single process in which the sedimentary pile moved and internally deformed, producing faulted dislocations that are observed as biostratigraphic hiatuses. In this interpretation the event occurred at ~2.1 Ma and involved a substantial thickness (possibly ~100 m of sediment). The slip may have involved one or more décollement surfaces on clay-rich beds, which could have been the progenitor for injected clay dikes observed at various levels in the three holes. The observed mixed and deformed intervals represent deformation within the lower and upper parts of the moving mass of sediment, whereas the less disturbed sedimentary succession between the hiatus levels may have rafted downslope without much physical disturbance. The biostratigraphic data cannot easily distinguish between these two explanatory models, although it is clear that the observed clay-rich intervals were not all derived from a single stratigraphic level.

A more readily interpretable biostratigraphy is observed beneath the lower disturbed interval (below ~260 mbsf) down to the base of Hole U1483A, with approximately the same sedimentation rate (~10 cm/ky) as above the disturbed intervals.

Paleomagnetism

Measurements summary

Paleomagnetic investigations at Site U1483 involved measurement of the natural remanent magnetization (NRM) of archive-half cores from Holes U1483A–U1483C before and after demagnetization in a peak alternating field (AF) of 15 mT. In addition to measuring 632 core sections, we took two discrete samples per core (typically in Sections 3 and 6) from Hole U1482A (62 samples) to characterize the NRM demagnetization behavior and to investigate the rock magnetic properties of the sediment. For one of the discrete samples from each core (typically those from Section 3), NRM was measured before and after AF demagnetization in peak fields of 5, 10, 15, 20, 30, 40, and 60 mT; the other samples were only demagnetized at 15 and 40 mT. Rock magnetic investigations comprised measurements of magnetic susceptibility (χ), susceptibility of anhysteretic remanent magnetization (χARM) imparted using a 100 mT AF demagnetization and 0.05 mT direct current bias field, and isothermal remanent magnetization (IRM) acquired in 300 and 1000 mT (saturation IRM [SIRM]) fields. All sample measurements were mass corrected. The Icefield MI-5 orientation tool was deployed with nonmagnetic hardware for all cores, which permitted azimuthal correction of declination. Azimuthally corrected declination is largely coherent between cores; however, absolute values in Holes U1483A and U1483B cluster around 180° for normal polarity and 0° for reversed polarity, suggesting that the issues of baseline offset in azimuthally corrected declination experienced throughout this expedition and during previous expeditions (McNeill et al., 2017) affected these measurements. In Hole U1483C, absolute values during normal (reversed) polarity intervals mainly cluster around the correct value of 0° (180°); however, declination values of some cores are 45°–60° offset to this in absolute terms. McNeill et al. (2017) suggest a simple −180° correction could be applied to the corrected declination data. This correction would rotate Holes U1483A and U1483B back to expected values for the respective polarity and match them up with data from Hole U1483C. However, we leave declination uncorrected for this additional offset in the plotted figures, so care should be employed for future calculations of virtual geomagnetic poles using these data.

Rock magnetic characterization

Whole-Round Multisensor Logger (WRMSL) magnetic susceptibility values average 3.8×10^{-5} SI (see **Physical properties**) and, when coupled with average χ ($2.4 \times 10^{-8} \pm 1.9 \times 10^{-8}$ m^3/kg as 2 standard deviations [2σ]) and SIRM ($5.4 \times 10^{-5} \pm 4.3 \times 10^{-5}$ Am^2/kg as 2σ) values, suggest relatively low (ferri)magnetic mineral concentration in the sediment deposited at Site U1483 (Figure **F22**). Aside from one sample from the top of Hole U1483A, all samples acquire >90% of their SIRM remanence in a field of 300 mT, suggesting that ferrimagnetic minerals (e.g., [titano]magnetite [$Fe_xTi_xO_4$] and/or maghemite [γ-Fe_2O_3]) control the remanence carrying properties of the sediment and that high-coercivity minerals (e.g., hematite [Fe_2O_3]) are relatively minor remanence carrying phases by comparison. Although average magnetic susceptibility values are lower than those at the other Northwest Australian margin site (U1482), SIRM values and χARM/SIRM ratios are higher, indicating greater concentrations of fine ferrimagnetic minerals at this site than at Site U1482. NRM_{15mT} intensity is higher (~10^{-4} A/m) in the upper ~75 mbsf of each hole, decreases between 75 and 85 mbsf, and remains low (~10^{-4} to 10^{-5} A/m) and variable below ~85 mbsf, occasionally approaching the measurement noise level of the magnetometer (see **Paleomagnetism** in the Expedition 363 methods chapter [Rosenthal et al., 2018a]). These changes occur around the same time interstitial water sulfate concentration decreases to almost zero and methane concentration peaks (Figure **F23**), associated with the sulfate–methane transition zone (SMTZ) and anaerobic oxidation of methane (see **Geochemistry**), indicating that early sediment diagenesis (e.g., Karlin and Levi, 1983; Rowan et al., 2009) is likely influencing the magnetic assemblage deposited at Site U1483 below ~75 mbsf. All other things being equal, the higher χARM/SIRM ratios at Site U1483 than at Site U1482 suggest that alteration of the (assumed) primary detrital ferrimagnetic oxides at Site U1483 may not be as severe as that experienced at Site U1482 because the finest grains are usually the first to be lost from the magnetic assemblage during early sediment diagenesis.

Figure F22. Archive-half NRM intensity after 15 mT AF demagnetization, discrete sample χ and SIRM, and discrete sample χARM/SIRM and IRM_{300mT}/IRM_{1000mT} ratios, Hole U1483A. Shading = intervals of soft-sediment deformation identified during core description.

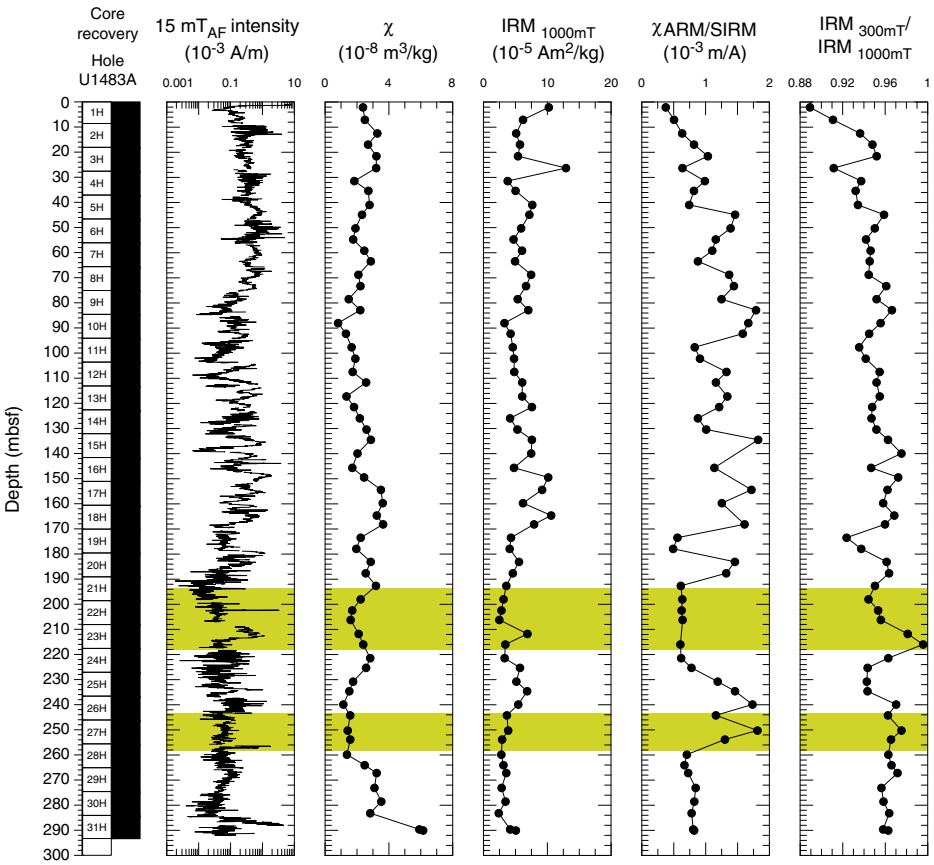

Paleomagnetic data and core orientation

NRM demagnetization behavior and IRM_{300mT}/IRM_{1000mT} ratios in the upper ~92 mbsf of Site U1483 are consistent with (titano)magnetite being the primary remanence-carrying mineral species in sediments deposited at Site U1483 (Figure **F22**). The drill string overprint is effectively removed after AF demagnetization in a 5–15 mT field, and following exposure to higher AF demagnetization steps, inclination and declination trend to the origin on Zijderveld diagrams (Zijderveld, 1967), indicating a single component to the magnetization (Figure **F24**). Origin-anchored maximum angular deviation values of the principal component analysis (PCA) calculated over the 15–40 mT range average 4.5° (range = 1°–9°) for the upper ~92 mbsf (Figures **F23**, **F24**), suggesting paleomagnetic directions are relatively stable and should yield reliable estimates for magnetostratigraphy (Stoner and St-Onge, 2007). Lower NRM_{15mT} intensity below ~92 mbsf is associated with higher average maximum angular deviation values (average = 13°; range = 2°–41°) and slightly more scattered directions on Zijderveld diagrams and stereoplots (Figure **F24**). Scatter in superconducting rock magnetometer (SRM) measurement directions is greatest and the maximum angular deviation values are highest during periods when NRM_{15mT} intensity is less than ~5×10^{-5} (Figure **F23**), suggesting that higher maximum angular deviation values likely reflect lower signal-to-noise ratios and/or result from sedimentological variability rather than geomagnetic instability. During several intervals of relatively high NRM_{15mT} intensity (particularly between 117 and 183 mbsf), maximum angular deviation values are relatively low, suggesting that paleomagnetic directions below ~92 mbsf can be as well resolved as those above ~92 mbsf (Figures **F23**, **F24**).

For all APC cores, declination was corrected using the Icefield MI-5 tool (see **Operations**). In Holes U1483A and U1483B, azimuthally corrected declination is consistent between adjacent cores within each hole and absolute values cluster around ~0° and ~180° (Figures **F23**, **F25**). However, assuming the uppermost sediment in each hole was deposited during normal polarity associated with the Brunhes Chron (see **Biostratigraphy**), declination values experience an offset of ~180° in absolute terms because declination should cluster around 0° (180°) during periods of normal (reversed) polarity. This phenomenon was a persistent issue during Expedition 363 and was also experienced during Expedition 362 (McNeill et al., 2017). In Hole U1483C, corrected declination values cluster between 270° and 360° for periods of normal polarity and between ~135° and 180° for periods of reversed polarity (Figure **F26**). Between-core offsets were not observed in the other holes at this site and likely result from incorrect correction from the Icefield MI-5 tool. Reevaluation of the Icefield MI-5 tool data for Hole U1483C revealed the original magnetic tool face picks to be robust. Consultation with the Operations Superintendent revealed that there was no difference in the hardware used (drill collars, core barrels, sinker bars, BHA, etc.) to recover sediment from Hole U1483C, and the Icefield MI-5 tool used (tool #2007) had previously given values of ~180° for periods of resolvable normal polarity in the upper ~70 mbsf of Hole U1482B. Although the origins of both the ~180° baseline offset in Holes U1483A and U1483B and the shallower 45°–90° offset in Hole U1483C are not immediately clear, they appear sys-

Figure F23. NRM intensities before and after 15 mT AF demagnetization, WRMSL magnetic susceptibility (MS), interstitial water (IW) sulfate and methane concentrations, maximum angular deviation (MAD), and inclination (dashed lines = predicted values assuming a geocentric axial dipole [GAD] field for normal (–25°) and reversed (25°) polarity for the site latitude) and azimuthally corrected declination after 15 mT AF demagnetization, Hole U1483A. Magnetostratigraphy and GPTS shown at right. Black = normal polarity, white = reversed polarity, gray = no magnetostratigraphic interpretation. Black squares = discrete samples, shading = intervals of soft-sediment deformation identified during core description.

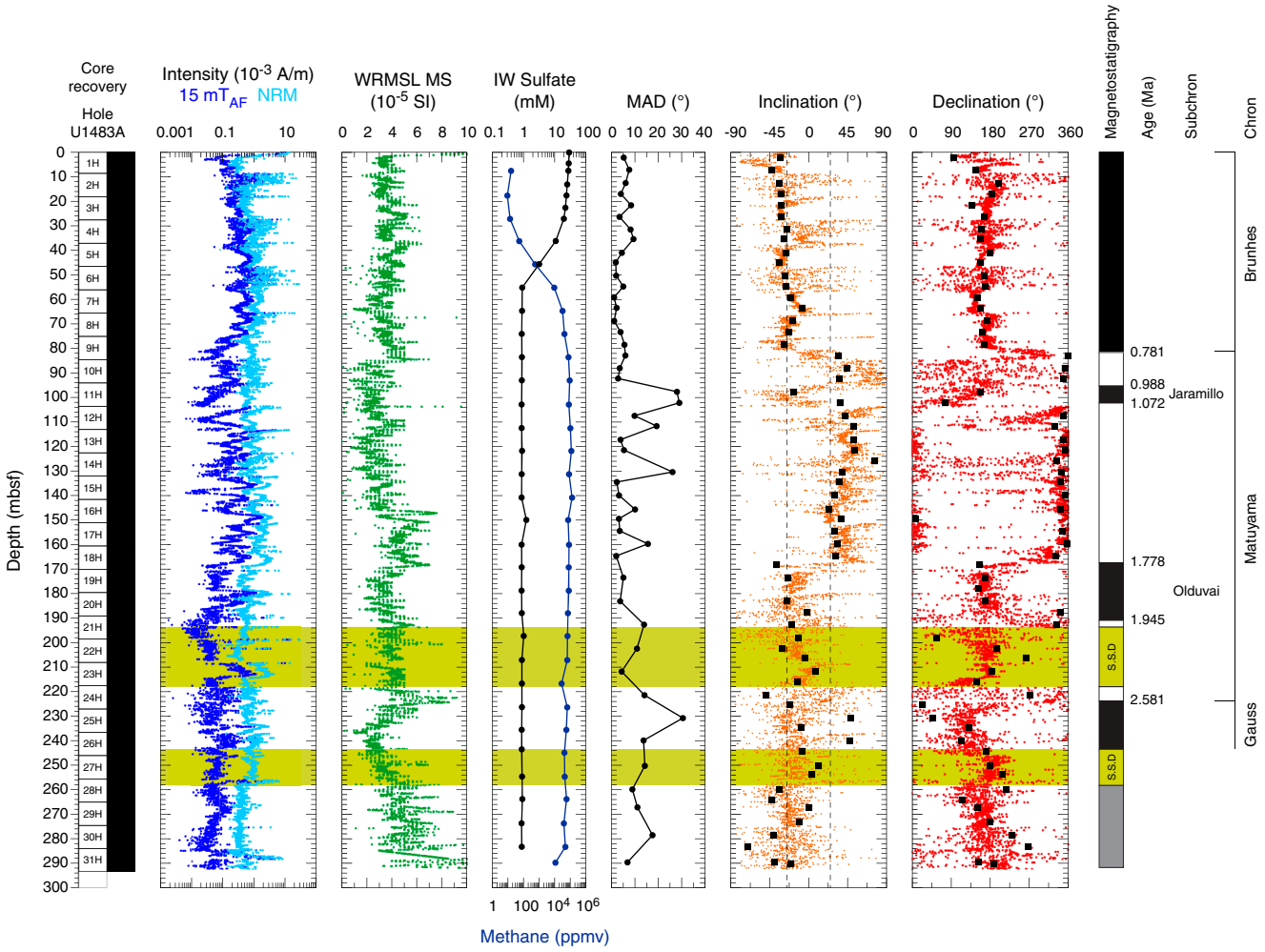

tematic (the two declination clusters are ~180° offset to each other during deployment of each tool respectively), and we assume that declination values rotated 180° relative to the uppermost sediment values reflect periods of reversed polarity.

NRM intensity before and after 15 mT AF demagnetization, WRMSL magnetic susceptibility, and inclination and azimuthally corrected declination after 15 mT AF demagnetization are shown for Holes U1483A, U1483B, and U1483C in Figures **F23**, **F25**, and **F26**, respectively. Displayed inclination and declination values were cleaned of visibly disturbed intervals and voids (see **Paleomagnetism** in the Expedition 363 methods chapter [Rosenthal et al., 2018a]). Inclination and declination measured on discrete samples are in excellent agreement with those measured on the archive-half sections (Figure **F23**) and plot around the expected values of approximately ±25° for the site latitude assuming a geocentric axial dipole (GAD) field. Declination shows a similar, relatively stable pattern with data points clustering around values of inferred normal and reversed polarity, suggesting that paleomagnetic directions measured at Site U1483 are sensitive to geomagnetic field behavior.

Magnetostratigraphy

Sediment in all three holes appears to have been deposited (quasi)continuously with no major hiatus or erosional surfaces downhole to ~194–195 mbsf. Below this depth, a series of intervals of soft-sediment deformation and discontinuities affect the record (see **Core description** and **Biostratigraphy**). Because the depositional and stratigraphic history of the deformed intervals is unclear, we highlight these regions in Figures **F23**, **F25**, and **F26** and exclude them from any geomagnetic interpretation. Low concentrations of ferrimagnetic minerals coupled with reduced geomagnetic field strength during the reversal process (e.g., Valet et al., 2005) result in transitional directions at Site U1483 that are often more scattered than stable polarity. Nevertheless, we observe five distinct ~50° shifts in inclination and five coeval ~180° changes in declination across all three holes in the interval above the deformation at ~194–195 mbsf. Interpretation of these horizons as reversals of the geomagnetic field allows correlation to the geomagnetic polarity timescale (GPTS; Cande and Kent, 1995) of the geologic timescale (Hilgen et al., 2012) and an assignment of age. The

Figure F24. A–F. Discrete sample AF demagnetization results, Hole U1483A. Left plots: intensity variation through progressive AF demagnetization steps. Middle and right plots: NRM vector measurements after each AF demagnetization treatment on orthogonal (Zijderveld; blue = horizontal projections, red = vertical projections) and stereographic (solid squares = positive inclination, open squares = negative inclination) projections, respectively. MAD = maximum angular deviation.

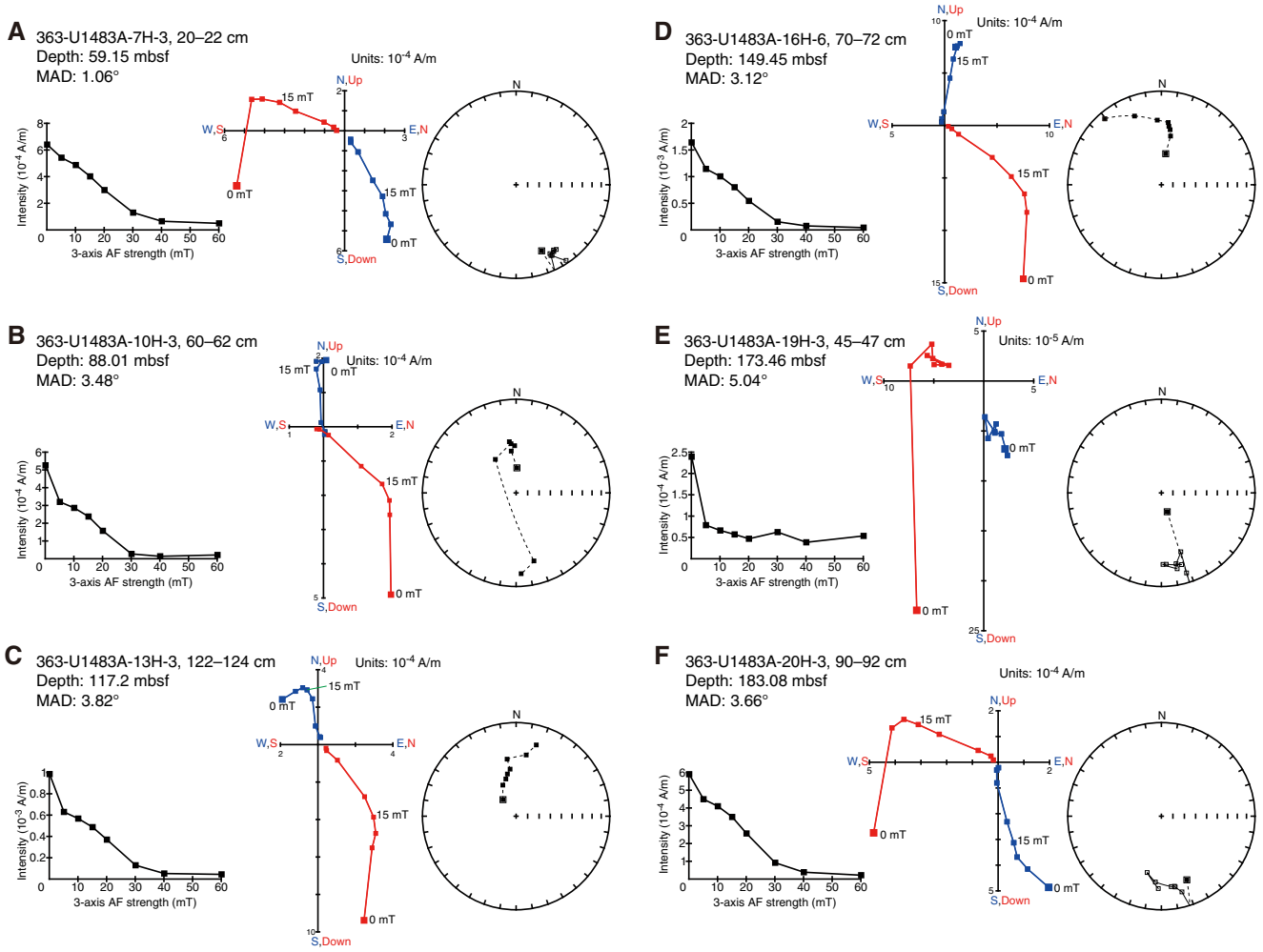

Matuyama/Brunhes boundary (0.781 Ma) is identified at 77.88–82.78 mbsf (note that these ranges encompass the minimum and maximum depths across all three holes; see Table **T8** for the depths of each boundary in each hole). Below this depth, we observed the upper (89.67–97.32 mbsf; 0.988 Ma) and lower (96.32–103.72 mbsf; 1.072 Ma) boundaries of the Jaramillo normal and the upper (163.77–174.71 mbsf; 1.778 Ma) and lower (182.55–189.65 mbsf; 1.945 Ma) boundaries of the Olduvai normal, with the lower Olduvai occurring a few meters above the first interval of sediment deformation. These reversal horizons are in excellent agreement with both the calcareous nannofossil and planktonic foraminifer datums and yield a sedimentation rate of ~10 cm/ky since the middle Pleistocene (see **Biostratigraphy**). In sediment between the two deformed intervals in Hole U1483A, we observe a transition from reversed polarity to normal polarity in both inclination and declination between ~221.6 and 229.1 mbsf during a period of relatively high NRM_{15mT} intensity (~10^{-4} A/m) and magnetic susceptibility (Figure **F23**). This same behavior is observed in Holes U1483B and U1483C, suggesting that it is the same stratigraphic horizon (Figures **F25**, **F26**). Biostratigraphic datums constrain this sediment package between the intervals of soft-sediment deformation to be ~2.4–2.8 Ma (see **Biostratigraphy**), and the only reversed-to-normal transition during this time frame is the Gauss/Matuyama boundary (2.581 Ma). Thus, guided by the biostratigraphic data, we can tentatively assign an age of 2.581 Ma to the reversal horizon between ~221.6 and 229.1 mbsf at Site U1483 (see Table **T8** for the depths in each hole). Below this event, inclination and declination in all three holes are either normal polarity and/or highly scattered and difficult to interpret. Given evidence of postdepositional deformation and slumping deeper in the record at this site, it is difficult to make any further magnetostratigraphic interpretation. As such, the normal polarity signature of the lower part of the record should not be simply interpreted as Gauss Chron (C2An.1n) in age without further investigation.

Figure F25. NRM intensities before and after 15 mT AF demagnetization, WRMSL MS, and inclination (dashed lines = predicted values assuming a GAD field for normal (−25°) and reversed (25°) polarity for the site latitude) and azimuthally corrected declination after 15 mT AF demagnetization, Hole U1483B. Magnetostratigraphy and GPTS shown at right. Black = normal polarity, white = reversed polarity, gray = no magnetostratigraphic interpretation. Green shading = intervals of soft-sediment deformation identified during core description.

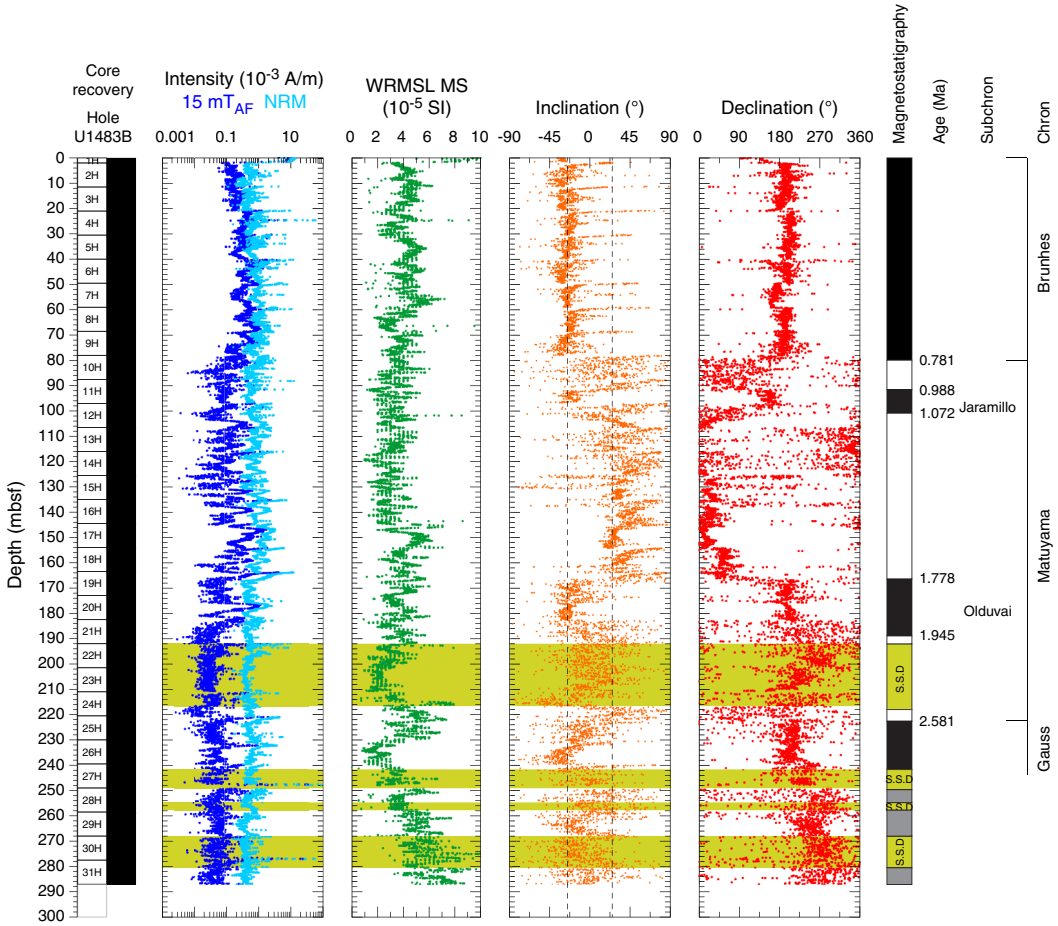

Figure F26. NRM intensities before and after 15 mT AF demagnetization, WRMSL MS, and inclination (dashed lines = predicted values assuming a GAD field for normal (–25°) and reversed (25°) polarity for the site latitude) and azimuthally corrected declination after 15 mT AF demagnetization, Hole U1483C. Magnetostratigraphy and GPTS shown at right. Black = normal polarity, white = reversed polarity, gray = no magnetostratigraphic interpretation. Green shading = intervals of soft-sediment deformation identified during core description.

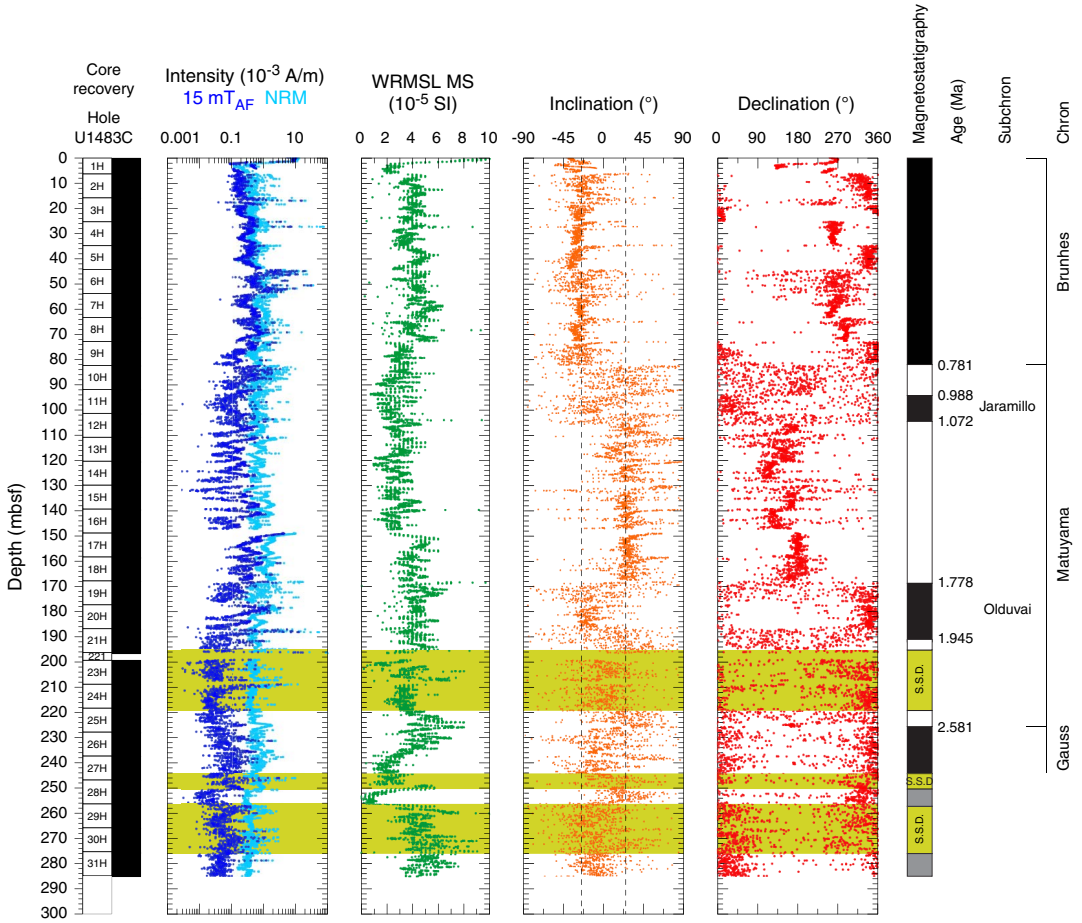

Table T8. Top and base depths of identified reversal boundaries determined from last and first points of stable polarity in Holes U1483A, U1483B, and U1483C. * = guided by biostratigraphic datums. Ages are determined using the geologic timescale of Hilgen et al. (2012). **Download table in CSV format.**

Horizon	Age (Ma)	Top depth (mbsf)	Base depth (mbsf)	Midpoint depth (mbsf)	Range (m)
Hole U1483A					
Matuyama/Brunhes	0.781	80.17	80.85	80.51	0.34
Upper Jaramillo	0.988	94.95	97.32	96.14	1.18
Lower Jaramillo	1.072	103.46	103.72	103.59	0.13
Upper Olduvai	1.778	167.40	171.60	169.50	2.10
Lower Olduvai	1.945	186.20	189.65	187.93	1.72
Gauss/Matuyama*	2.581	224.20	228.10	226.15	1.95
Hole U1483B					
Matuyama/Brunhes	0.781	77.89	78.53	78.21	0.32
Upper Jaramillo	0.988	89.68	92.42	91.05	1.37
Lower Jaramillo	1.072	96.33	97.48	96.90	0.57
Upper Olduvai	1.778	163.78	168.66	166.22	2.44
Lower Olduvai	1.945	182.55	187.91	185.23	2.68
Gauss/Matuyama*	2.581	221.60	223.00	222.30	0.70
Hole U1483C					
Matuyama/Brunhes	0.781	82.18	82.78	82.48	0.30
Upper Jaramillo	0.988	94.41	95.28	94.85	0.43
Lower Jaramillo	1.072	101.27	102.53	101.90	0.63
Upper Olduvai	1.778	167.50	174.71	171.11	3.60
Lower Olduvai	1.945	185.26	187.23	186.24	0.98
Gauss/Matuyama*	2.581	226.33	229.10	227.71	1.39

Physical properties

Physical properties were measured on whole-round cores, split cores, and discrete samples from all three holes cored at Site U1483 to provide basic data for characterizing the core sections. Gamma ray attenuation (GRA) bulk density and magnetic susceptibility were measured on all core sections from Holes U1483B and U1483C with the Special Task Multisensor Logger (STMSL) immediately after the cores were brought on board. All core sections were measured with the GRA bulk densitometer, magnetic susceptibility loop, and *P*-wave logger (PWL) on the WRMSL. PWL measurements were discontinued after Cores 363-U1483A-14H, 363-U1483B-11H, and 363-U1483C-13H when the data became unreliable due to expansion cracks in the core. After WRMSL scanning, whole-round sections were logged for NGR before splitting. Point-sensor magnetic susceptibility and color spectrophotometry (color reflectance) were measured on split core sections using the Section Half Multisensor Logger (SHMSL). Discrete thermal conductivity, *P*-wave velocity, and moisture and density (MAD) measurements were made for Hole U1483A samples. Discrete *P*-wave measurements (*z*- and *x*-axes) were made using the *P*-wave caliper (PWC) system on the Section Half Measurement Gantry (SHMG). Discrete *z*-axis measurements were discontinued after Core 363-U1483A-7H and *x*-axis measurements after Core 11H due to lack of clear signals in the indurated and cracked sediment. Preconditioning treatments were applied to the data to aid in interpretation of noisy or spiky data (for details, see **Physical properties** in the Expedition 363 methods chapter [Rosenthal et al., 2018a]). All data shown in figures are from the preconditioned data sets. Tables presented in this section contain raw and treated data for NGR, WRMSL GRA bulk density, magnetic susceptibility, and *P*-wave velocity. Raw data for all data sets are available from the LIMS database.

GRA bulk density

GRA bulk density values were measured using the STMSL and the WRMSL on whole-round core sections (see **Physical properties** in the Expedition 363 methods chapter [Rosenthal et al., 2018a]). Long-term trends of GRA bulk density in Holes U1483A–U1483C (WRMSL) are comparable (Figure **F27**; Tables **T9**, **T10**, **T11**). For description purposes, we thus consider Hole U1483A as

Figure F27. Physical property measurements, Holes U1483A and U1483C. GRA, MS, and PWL data were measured on the WRSMSL. Yellow shading = intervals of soft-sediment deformation observed in all holes. cps = counts per second.

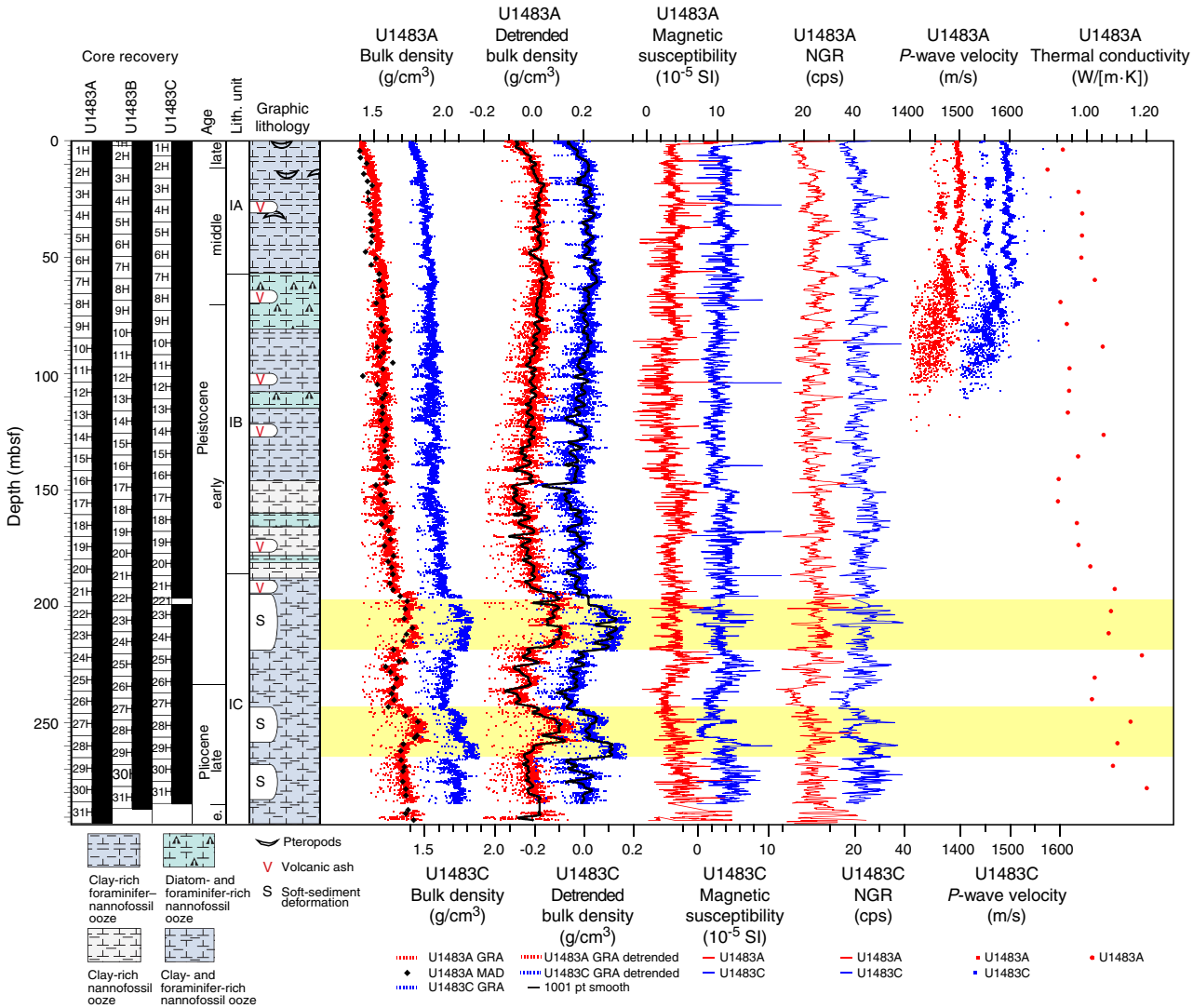

Table T9. Raw, cleaned, and detrended Whole-Round Multisensor Logger gamma ray attenuation (GRA) bulk density data, Hole U1483A. **Download table in CSV format.**

Table T10. Raw, cleaned, and detrended Whole-Round Multisensor Logger gamma ray attenuation (GRA) bulk density data, Hole U1483B. **Download table in CSV format.**

Table T11. Raw, cleaned, and detrended Whole-Round Multisensor Logger gamma ray attenuation (GRA) bulk density data, Hole U1483C. **Download table in CSV format.**

Figure F28. Bulk density, WRMSL MS, and NGR overlaid on core photos (generated using Code for Ocean Drilling Data [CODD] [Wilkens et al., 2017]) from Hole U1483A, 0–145 mbsf. cps = counts per second.

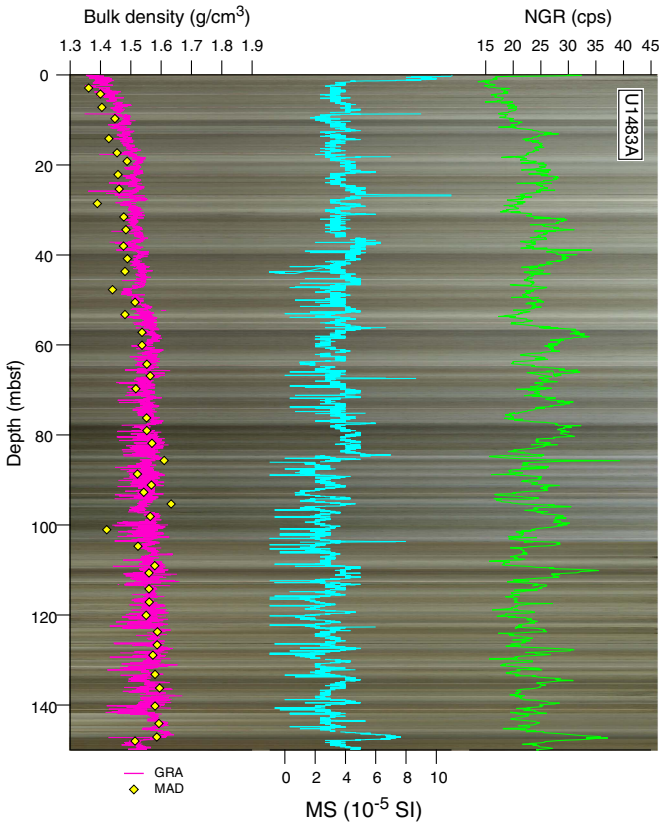

representative of all holes. GRA bulk density in Hole U1483A progressively increases with depth, which is in good agreement with long-term changes in MAD bulk density (Figure **F27**) and is consistent with compaction. GRA bulk density increases from ~1.37 g/cm^3 at the seafloor to 1.5 g/cm^3 at 20 mbsf with low-amplitude short-term variability. Between 20 and 50 mbsf, GRA bulk density remains stable at ~1.5 g/cm^3. This interval mostly corresponds to lithologic Subunit IA. A second increase in GRA bulk density from 1.5 to 1.6 g/cm^3 occurs at ~50 mbsf, below which the GRA bulk density values remain stable at 1.6 g/cm^3 until 150 mbsf. At 150 mbsf, GRA bulk density drops to 1.5 g/cm^3 and then progressively increases to 1.65 g/cm^3 between 150 and 200 mbsf. These subtle variations in GRA bulk density between ~50 and 200 mbsf largely occur within lithologic Subunit IB. A broad maximum in GRA bulk density occurs from 200 to 225 mbsf with values of ~1.8 g/cm^3. Values then decrease rapidly to 1.6 g/cm^3 between 225 and 240 mbsf. Between 240 and 250 mbsf, GRA bulk density increases to 1.8 g/cm^3 and then remains above this value until ~260 mbsf, where it decreases to 1.7 g/cm^3. Between 260 mbsf and the base of the record at 292 mbsf, GRA bulk density increases from 1.7 to 1.8 g/cm^3. The last core in Hole U1483A (31H) had to be pumped out of the core barrel. During this process, a small amount of heat was applied to the outside of the core barrel until the plastic core liner began to move. The core liner was heavily cracked during this process, and as a result, the first three sections of Core 31H could not be measured on the STMSL or WRMSL. The GRA bulk density, magnetic susceptibility, and NGR data obtained on Core 31H may have been affected during exposure of the core to heat and should be treated cautiously. In Subunit IC, two bulk density peaks centered at 215 and 250 mbsf deviate from the overall trend. These coincide with two distinct intervals of soft-sediment deformation observed in all holes (yellow shading in Figure **F27**) (see **Core description**).

Linearly detrending the GRA bulk density record allows us to correct for the downhole compaction effect and highlight subtle variations in the record that may be due to lithology. The detrended record shows a change from values increasing downhole in Subunit IA to values decreasing downhole in Subunit IB, coinciding with a downhole change from nannofossil ooze to diatom-rich nannofossil ooze (Figure **F27**). Within Subunit IB, a change in the slope of the trend at ~150 mbsf coincides with a shift to clay-dominated sediment (see **Core description**). At Site U1483, the relationship among the short cycles in NGR, magnetic susceptibility, and GRA bulk density is different from that at Site U1482. The short-term meter-scale variations in bulk density at Site U1483 (Figure **F28**; Table **T9**; see also **Magnetic susceptibility** and **Natural gamma radiation**) are smaller in amplitude than those at Site U1482. In addition, in the upper 80 mbsf of Hole U1483A we did not observe the positive correlation between NGR, magnetic susceptibility, and GRA bulk density or the light–dark sedimentary cycles seen at Site U1482. This difference probably reflects the more complex lithology at Site U1483, with the presence of light greenish gray, greenish gray, and brown layers (see **Core description**). Below 80 mbsf in Hole U1483A, short wavelength variations in NGR, magnetic susceptibility, and sometimes GRA bulk density appear to be better correlated than in the interval above 80 mbsf (Figure **F28**).

Magnetic susceptibility

Site U1483 has overall low magnetic susceptibility, with most values ranging from 0.3 × 10^{-5} to 8.3 × 10^{-5} SI (Figures **F27**, **F29**; Tables **T12**, **T13**, **T14**). Over the entire record, the median value in all three holes is 3.67 × 10^{-5} SI with standard deviations of 1.53, 1.41, and 1.40 in Holes U1483A, U1483B, and U1483C, respectively. Long-term WRMSL magnetic susceptibility variability among Holes U1483A, U1483B, and U1483C are comparable, so for description purposes we consider Hole U1483A representative of all holes. Between 0 and ~80 mbsf, average magnetic susceptibility is constant at ~3.7 × 10^{-5} SI. Between 80 and 140 mbsf, average magnetic susceptibility decreases slightly to ~2.9 × 10^{-5} SI. Between 140 and 175 mbsf, average magnetic susceptibility increases to ~4.3 × 10^{-5} SI. At 175 mbsf, average magnetic susceptibility decreases to ~3.7 × 10^{-5} SI, where it remains until ~210 mbsf. Between 210 and 235 mbsf, magnetic susceptibility displays a broad maximum, with values starting at ~4 × 10^{-5} and increasing to ~8 × 10^{-5} SI at ~222 mbsf before decreasing to ~2 × 10^{-5} SI by 235 mbsf. From 235 mbsf to the base of the record (292 mbsf), magnetic susceptibility progressively increases from ~2 × 10^{-5} to ~6 × 10^{-5} SI. The magnetic susceptibility values from the deepest core in Hole U1483A (Core

363-U1483A-31H) were probably affected by exposure to heat while pumping out the core liner after it became stuck in the core barrel (see **GRA bulk density**).

Short-term cycles are superimposed on the long-term trends described above (Figure **F28**). In the upper 80 mbsf, these magnetic susceptibility cycles are multiple meter–scale variations with amplitudes from ~2 × 10^{-5} to 3 × 10^{-5} SI. Deeper than 80 mbsf, the cycles become shorter, roughly 1–2 m in length, and display higher amplitudes from ~2 × 10^{-5} to 5 × 10^{-5} SI. Through the deformed intervals and in the deepest part of the record (250 mbsf and below), amplitudes are even higher, from ~5 × 10^{-5} to 8 × 10^{-5} SI (Figure **F27**). The magnetic susceptibility data do not delineate the intervals of soft-sediment deformation that are apparent in the GRA bulk density record (yellow shading in Figure **F27**).

Figure F29. Comparison of despiked WRMSL MS data, Holes U1483A (red), U1483B (green), and U1483C (blue). Green shading = magnetic susceptibility spikes associated with tephra identified by core describers, yellow shading = magnetic susceptibility spikes that occur at similar depths to identified tephras in other holes but were not identified by core describers in the relevant hole, orange shading = magnetic susceptibility spikes not associated with tephras but with other features in the sediment core.

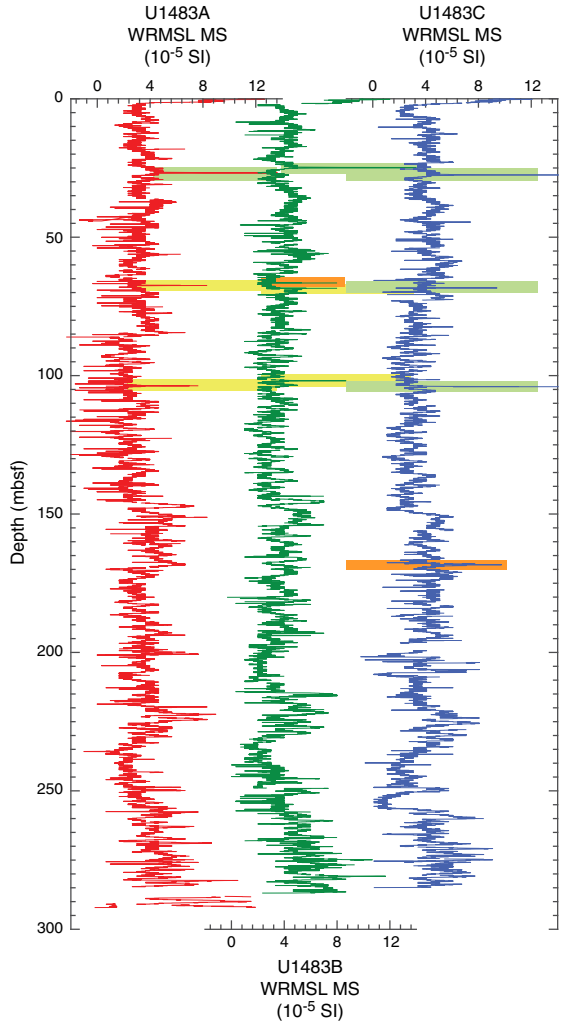

Table T12. Raw and cleaned Whole-Round Multisensor Logger magnetic susceptibility (MS) data, Hole U1483A. **Download table in CSV format.**

Table T13. Raw and cleaned Whole-Round Multisensor Logger magnetic susceptibility (MS) data, Hole U1483B. **Download table in CSV format.**

Table T14. Raw and cleaned Whole-Round Multisensor Logger magnetic susceptibility (MS) data, Hole U1483C. **Download table in CSV format.**

Magnetic susceptibility spikes at ~25–27 mbsf in all three holes correspond to a tephra layer (green bar in Figure **F29**). A peak in magnetic susceptibility in Hole U1483C (~68.3 mbsf; green bar in Figure **F29**) also corresponds to a tephra layer, and magnetic susceptibility spikes are noted at similar depths in Holes U1483A and U1483B (67.4 and 66.5 mbsf, respectively; yellow bars in Figure **F29**); however, tephra layers were not identified during visual examination of the cores at these depths. Similarly, another tephra layer visually identified in Hole U1483C was detected by magnetic susceptibility (104.0 mbsf; green bar in Figure **F29**) and may have corresponding peaks in Holes U1483A and U1483B (103.7 and 101.8 mbsf, respectively; yellow bars in Figure **F29**), although no tephra layers were visually identified at those depths in these holes. Two spikes unrelated to tephra layers are also identified (orange bars in Figure **F29**). The first of these peaks is found in Hole U1483B at 68.4 mbsf and corresponds to a concentration of gypsum associated with a concretion that may be composed of biotite and barite (see **Core description**; Figure **F14**). Based on the susceptibility of common minerals (Blum, 1997), gypsum has negative magnetic susceptibility values, but biotite is associated with very high magnetic susceptibility values, which may explain the high peak in the magnetic susceptibility data in Hole U1483B. The second magnetic susceptibility peak occurs in Hole U1483C at 168.3 mbsf. Although nothing is visible in the sediment to explain the presence of this peak, it may relate to sediment disturbance caused by gas expansion.

Natural gamma radiation

Both long-term trends and short-term variability in NGR records are similar among holes at Site U1483. In the uppermost 25 mbsf of all holes, NGR progressively increases from 15 to ~27 counts/s (Figure **F27**; Tables **T15**, **T16**, **T17**). Between 25 and 100 mbsf, distinct cyclicity, approximately 9–10 m in length, is observed and appears to be unrelated to core breaks (Figure **F28**), with NGR counts varying from 17 to 33 counts/s. From 100 to 185 mbsf, the cycles are shorter, ~2–5 m in length, and of lower amplitude, ~10 counts/s. Below 185 mbsf in Subunit IC, the cycles are even shorter, ~1–2 m in length, and although the variability of ~10 counts/s is similar to that in the interval above, the record from Subunit IC also occasionally shows prominent short-term variability up to 30 counts/s for higher peaks, which is present in the intervals of soft-sediment deformation. NGR data from Core 363-U1483A-31H also seem to be affected by the process used to extract the stuck core liner from the core barrel (see **GRA bulk density**).

P-wave velocity

Compressional *P*-wave velocity measurements were performed on whole-round sections using the PWL for all of the holes cored at

Table T15. Raw and cleaned Natural Gamma Radiation Logger natural gamma radiation (NGR) data, Hole U1483A. **Download table in CSV format.**

Table T16. Raw and cleaned Natural Gamma Radiation Logger natural gamma radiation (NGR) data, Hole U1483B. **Download table in CSV format.**

Table T17. Raw and cleaned Natural Gamma Radiation Logger natural gamma radiation (NGR) data, Hole U1483C. **Download table in CSV format.**

Site U1483. Outliers above 1750 m/s were removed from the PWL velocity data (Figures **F27**, **F30**; Tables **T18**, **T19**, **T20**). A downhole decrease in PWL velocity occurs at ~60 mbsf in all holes at Site U1483 (Figure **F30**), which is different from that at Site U1482, where the marked decrease in PWL velocity occurs at ~170 mbsf. The PWL data range between 1350 and 1530 m/s downhole for all holes (Figure **F30**). *P*-wave velocity increases from ~1500 to 1530 m/s between 0 and 60 mbsf and then decreases deeper than 60 mbsf, with the lowest values of ~1350 m/s at ~91 mbsf, possibly due to abundant cracks in the sediment. All of the holes have similar average *P*-wave velocity values. Differences in average values between the intervals shallower and deeper than 60 mbsf are in the range of 40–46 m/s. There are no apparent downhole cyclic variations and no obvious correlation between PWL velocity and NGR or magnetic susceptibility, which contrasts with the noticeable correlations at Site U1482 (see Figure **F32B** in the Site U1482 chapter [Rosenthal et al., 2018b]).

Figure F30. Discrete and whole-round *P*-wave measurements, Site U1483. The *z*-axis *P*-wave values excluded as outliers are circled.

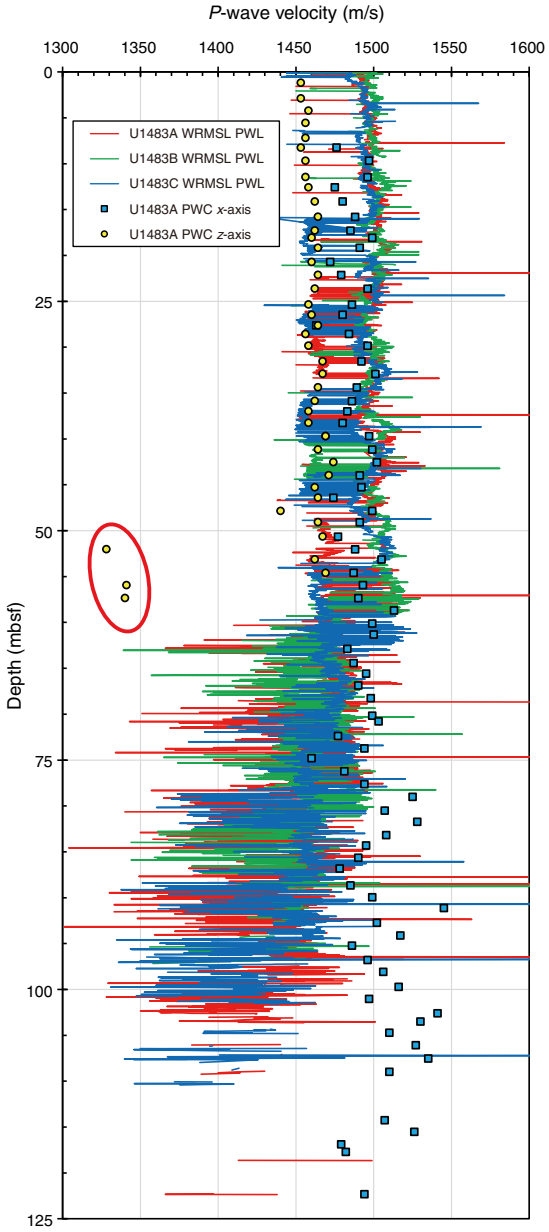

Table T18. Raw and cleaned Whole-Round Multisensor Logger *P*-wave logger data, Hole U1483A. **Download table in CSV format.**

Table T19. Raw and cleaned Whole-Round Multisensor Logger *P*-wave logger data, Hole U1483B. **Download table in CSV format.**

Table T20. Raw and cleaned Whole-Round Multisensor Logger *P*-wave logger data, Hole U1483C. **Download table in CSV format.**

PWC *x*- and *z*-axes velocity values show a slight increasing trend with depth. PWC *x*-axis velocity values increase from 1476 m/s at 8 mbsf to 1526 m/s at 120 mbsf. The *z*-axis values range from 1450 m/s at the seafloor to 1470 at 60 mbsf and are offset to lower values by about 20 m/s from the *x*-axis values. The *z*-axis values also display less variability than the *x*-axis measurements, likely because the *z*-axis is measuring over a greater length of the core, effectively smoothing the measurement. Three *z*-axis measurements from ~50 to 60 mbsf were excluded as outliers (red circle in Figure **F30**). These data points were acquired shortly before the *z*-axis measurement was discontinued because the data quality had considerably decreased downhole.

Moisture and density

Bulk density, dry density, grain density, and porosity were calculated from mass and volume measurements on discrete samples taken from the working halves of split cores from Hole U1483A (downhole to ~292 mbsf). The bulk density calculated using the MAD method corresponds well with the bulk density estimated from GRA bulk density, including within the interval affected by sediment deformation (Figure **F31**). In the upper 50 mbsf, corresponding to Subunit IA, MAD bulk density is offset to lower values by an average of ~0.05 g/cm^3 from the GRA bulk density. This offset is most likely due to water loss from the cores between measurement on the WRMSL and discrete sampling for MAD.

MAD bulk density increases downhole in Hole U1483A due to compaction with a best-fit slope of 0.11 g/cm^3/100 m. MAD dry density increases at a higher rate of 0.17 g/cm^3/100 m from the seafloor to the bottom of the hole. These rates vary slightly within different lithologic subunits, with a steeper slope in Subunit IA than in Subunit IB. Rates were not calculated for Subunit IC because sediment deformation and compaction appears to cause the slope to increase. MAD bulk and dry densities converge at ~50 mbsf, reflecting the downhole increase in compaction and reduction in porosity and water content. Porosity (percent pore space in the wet sediment volume) generally decreases with depth from 80% at the seafloor to ~55% at ~300 mbsf, with the exception of the deformed intervals in Subunit IC. Grain density is fairly constant throughout the site, with only a slight downhole increase from 2.66 to 2.72 g/cm^3.

Two outliers in MAD bulk density, one high and one low, occur at ~95 and 101 mbsf, respectively (black arrows on Figure **F31**). These values propagate through MAD calculations and appear as outliers in subsequent measurements and should be interpreted cautiously. Although the values have not been removed from the data set, figures have been scaled to maximize long-term trends and these outliers may not be visible in every panel.

Figure F31. MAD discrete sample dry, bulk, and grain densities and porosity, WRMSL GRA bulk density, and thermal conductivity, Hole U1483A. Black arrows indicate two unexplained outliers.

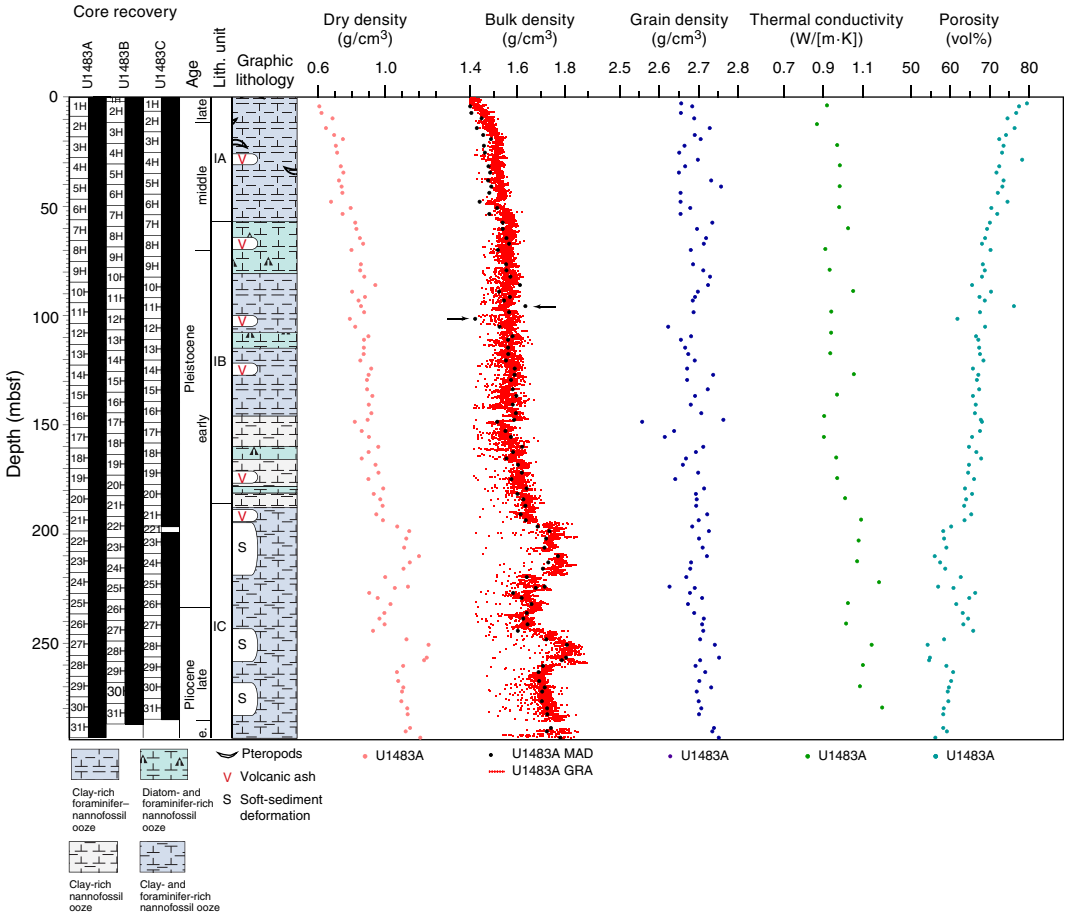

Thermal conductivity

A thermal conductivity profile was obtained at ~10 m resolution using a thermal conductivity needle (Figures **F27**, **F31**). Thermal conductivity measurements increase with depth from 0.09 to 1.15 W/(m·K) with average values of ~1 W/(m·K) and standard deviation of 0.06 W/(m·K). The trend from the top of Hole U1483A to the bottom (~279 mbsf) is not really clear (R^2 = 0.49), possibly because of variability in the lithology. Thermal conductivity results correlate well with the dry density values and are inversely correlated with porosity (Figure **F31**). This observation can be explained by the compaction effect. In comparison to Site U1482 at the same depth, thermal conductivity values are lower at Site U1483; however, the downhole trend in increasing thermal conductivity is steeper at Site U1483.

Downhole temperature measurements

Standard downhole temperature measurements were made on Cores 363-U1483A-4H (37.1 mbsf), 7H (65.6 mbsf), 10H (94.1 mbsf), and 13H (122.6 mbsf) using the APCT-3. The first measurement on Core 4H was unreliable, probably due to unstable hole conditions. An exponential decrease in temperature is observed between 60 and 600 s after penetration and was used to estimate ambient temperature (unshaded area in Figure **F32**). Formation temperature increases with depth from 7.4°C at 65.6 mbsf to 11.11°C at 122.6 mbsf. The correlation between downhole temperatures and depth is excellent (R^2 = 0.99994). Using the slope of the temperature-depth relationship, we estimated that the bottom water temperature at Site U1483 is 3.1°C, yielding a geothermal gradient of 65°C/km (Figure **F33**).

Figure F32. APCT-3 temperature-time series, Hole U1483A. Unshaded area = time interval with exponential decrease in temperature.

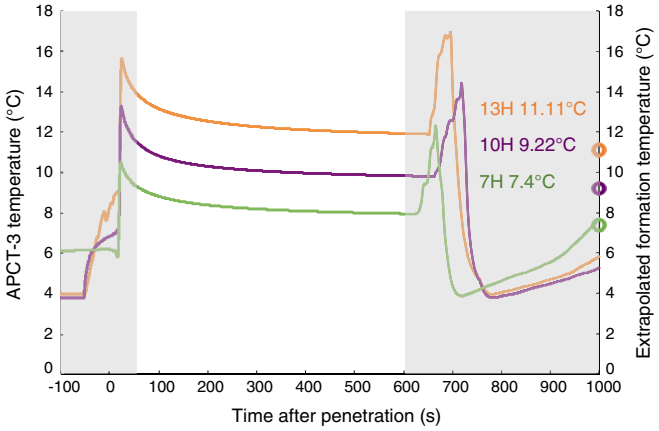

We estimated a thermal conductivity profile (with ~10 m resolution) (Figure **F33**) using laboratory-determined thermal conductivity data (see **Physical properties** in the Expedition 363 methods

Figure F33. Heat flow calculations, Hole U1483A. Green line = calculated thermal resistance, gray vertical line = average thermal conductivity value used for calculation of thermal resistance, solid diamonds and dashed line = corrected thermal conductivity, open diamonds = uncorrected thermal conductivity.

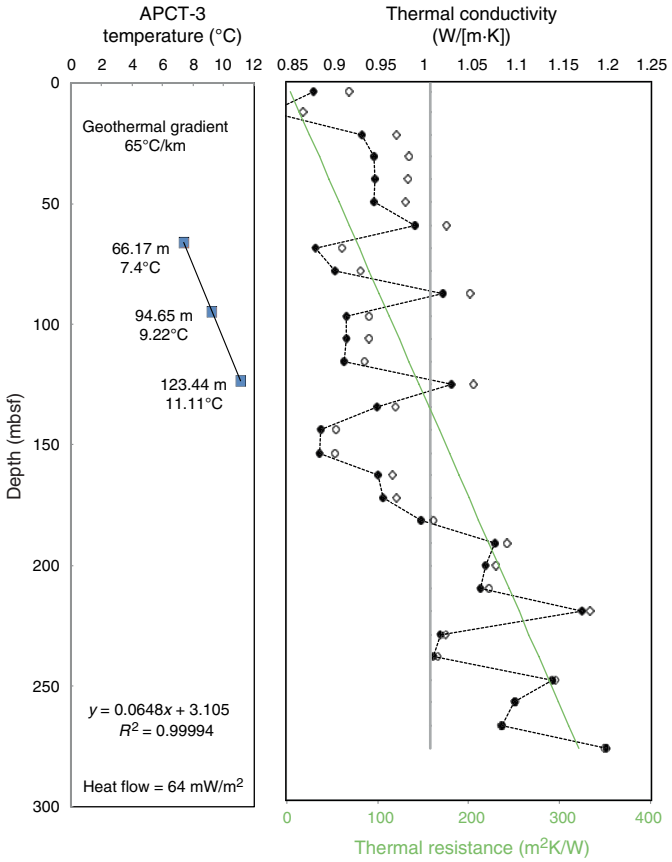

chapter [Rosenthal et al., 2018a]). Based on the in situ condition correction, thermal resistance was calculated using an average thermal conductivity of 0.99 W/(m·K) measured in Hole U1483A following the "average approach" outlined in Pribnow et al. (2000). The corrected thermal conductivity is lower relative to uncorrected values until ~200 mbsf, after which the corrected and uncorrected values converge. The offset between corrected and uncorrected values is greater at shallower depth and gradually decreases downhole. The slope of the linear fit between temperature and thermal resistance indicates a heat flow of 64 mW/m^2 for Site U1483 (calculated using the method described in Pribnow et al., 2000).

Stratigraphic correlation

Correlations between holes at Site U1483 were accomplished using Correlator software (version 2.1). Tie points were established mainly with Whole-Round Multisensor Logger (WRMSL) magnetic susceptibility data, although some were based primarily on L* data (Table **T21**). WRMSL gamma ray attenuation (GRA) bulk density and NGR data were helpful in making correlations (e.g., Figure **F34**), but because magnetic susceptibility data provided the most consistent means of correlation, it is the only data type shown in Figure **F35**. We constructed two spliced intervals, one from 0 to 211.5 m core composite depth below seafloor (CCSF) and the other

Table T21. Affine table, Site U1483. Note that there are two spliced intervals (0.0–211.5 and 239.8–266.8 m CCSF). L* = lightness, MS = magnetic susceptibility, GR = growth rate. (Continued on next page.) **Download table in CSV format.**

Core	Depth (mbsf)	Depth CCSF (m)	Offset (m)	Tie point depth CCSF (m)	Shift type	Data used	Reference hole, core
363-U1483A-							363-
1H	0.00	–0.07	–0.07	1.00	Tied to	L*	U1483C-1H
2H	8.60	8.98	0.38	11.96	Tied to	L*	U1483B-2H
3H	18.10	18.52	0.42	20.78	Tied to	MS	U1483B-3H
4H	27.60	28.59	0.99	32.36	Tied to	MS	U1483C-4H
5H	37.10	38.37	1.27	40.86	Tied to	MS	U1483B-5H
6H	46.60	48.37	1.77	51.63	Tied to	L*	U1483B-6H
7H	56.10	58.90	2.80	60.99	Tied to	MS	U1483B-7H
8H	65.60	68.10	2.50	71.25	Tied to	MS	U1483B-8H
9H	75.10	78.29	3.19	81.19	Tied to	MS	U1483B-9H
10H	84.60	88.27	3.67	90.31	Tied to	MS	U1483B-10H
11H	94.10	98.15	4.05	100.84	Tied to	MS	U1483B-11H
12H	103.60	109.46	5.86	112.08	Tied to	MS	U1483B-12H
13H	113.10	120.23	7.13	124.35	Tied to	MS	U1483C-13H
14H	122.60	131.56	8.96	134.25	Tied to	MS	U1483C-14H
15H	132.10	142.37	10.27	147.16	Tied to	MS	CU1483-15H
16H	141.60	153.24	11.64	154.84	Tied to	MS	U1483B-16H
17H	151.10	164.20	13.10	166.41	Tied to	MS	U1483B-17H
18H	160.60	174.66	14.06	178.12	Tied to	MS	U1483B-18H
19H	170.10	184.75	14.65	187.91	Tied to	MS	U1483C-19H
20H	179.60	195.73	16.13	199.43	Tied to	MS	U1483B-20H
21H	189.10	206.44	17.34	207.88	Tied to	MS	U1483B-21H
22H	198.60	216.87	18.27		Set; GR = 1.022		U1483A-21
23H	208.10	227.25	19.15		Set; GR = 1.092		U1483A-22
24H	217.60	238.07	20.47	245.82	Tied to	MS	U1483C-25H
25H	227.10	248.91	21.81	252.63	Tied to	MS	U1483B-25H
26H	236.60	260.00	23.40	262.47	Tied to	MS	U1483B-26H
27H	246.10	270.47	24.37		Set; GR = 1.100		U1483A-26
28H	255.60	282.44	26.84		Set; GR = 1.100		U1483A-27
29H	265.10	303.24	38.14	305.46	Tied to	MS	U1483B-30H
30H	274.60	317.44	42.84	322.01	Tied to	MS	U1483C-31H
31H	284.10	324.10	40.00		Set; GR = 1.156		U1483A-30H
363-U1483B-							363-
1H	0.00	–0.10	–0.10	0.98	Tied to	L*	U1483C-1H
2H	2.00	3.08	1.08	4.28	Tied to	L*	U1483C-1H
3H	11.50	12.46	0.96	14.16	Tied to	MS	U1483C-2H
4H	21.00	23.29	2.29	26.95	Tied to	MS	U1483A-3H
5H	30.50	33.26	2.76	34.96	Tied to	MS	U1483A-4H
6H	40.00	42.47	2.47	46.96	Tied to	MS	U1483A-5H
7H	49.50	52.73	3.23	54.22	Tied to	MS	U1483A-6H
8H	59.00	62.37	3.37	63.57	Tied to	MS	U1483A-7H
9H	68.50	72.36	3.86	73.53	Tied to	MS	U1483A-8H
10H	78.00	82.20	4.20	84.42	Tied to	MS	U1483A-9H
11H	87.50	92.23	4.73	93.22	Tied to	MS	U1483A-10H
12H	97.00	102.91	5.91	103.80	Tied to	MS	U1483A-11H
13H	106.50	113.38	6.88	116.61	Tied to	MS	U1483A-12H
14H	116.00	124.13	8.13	127.16	Tied to	MS	U1483A-13H
15H	125.50	135.58	10.08	138.85	Tied to	MS	U1483A-14H
16H	135.00	146.66	11.66	151.61	Tied to	MS	U1483A-15H
17H	144.50	157.57	13.07	161.04	Tied to	MS	U1483A-16H
18H	154.00	168.81	14.81	169.73	Tied to	MS	U1483A-17H
19H	163.50	179.65	16.15	183.16	Tied to	MS	U1483A-18H
20H	173.00	190.46	17.46	191.31	Tied to	MS	U1483A-19H
21H	182.50	201.34	18.84	204.92	Tied to	MS	U1483A-20H
22H	192.00	211.97	19.97		Set; GR = 1.104		U1483B-21H
23H	201.50	222.46	20.96		Set; GR = 1.104		U1483B-22H
24H	211.00	232.95	21.95		Set; GR = 1.104		U1483B-23H
25H	220.50	243.39	22.89	245.82	Tied to	MS	U1483C-25H
26H	230.00	253.56	23.56	255.43	Tied to	MS	U1483A-25H
27H	239.50	267.07	27.57	273.14	Tied to	MS	U1483A-27H
28H	249.00	276.91	27.91	278.73	Tied to	MS	U1483A-27H
29H	258.50	287.36	28.86	288.89	Tied to	MS	U1483A-28H
30H	268.00	298.56	30.56		Set; GR = 1.114		U1483B-29H
31H	277.50	309.69	32.19		Set; GR = 1.114		U1483B-20H

Table T21 (continued).

Core	Depth (mbsf)	Depth CCSF (m)	Offset (m)	Tie point depth CCSF (m)	Shift type	Data used	Reference hole, core
363-U1483C-							363-
1H	0.00	0.00	0.00	Mudline			
2H	6.30	5.89	–0.41	11.961	Tied to	L*	U1483B-2H
3H	15.80	14.83	–0.97	21.85	Tied to	MS	U1483A-3H
4H	25.30	24.98	–0.32	26.954	Tied to	MS	U1483A-3H
5H	34.80	34.78	–0.02	40.86	Tied to	MS	U1483B-5H
6H	44.30	44.42	0.12	46.96	Tied to	MS	U1483A-5H
7H	53.80	54.28	0.48	60.99	Tied to	MS	U1483B-7H
8H	63.30	64.86	1.56	69.87	Tied to	MS	U1483B-8H
9H	72.80	74.13	1.33	80.27	Tied to	MS	U1483B-9H
10H	82.30	84.53	2.23	90.31	Tied to	MS	U1483B-10H
11H	91.80	94.68	2.88	100.80	Tied to	MS	U1483B-11H
12H	101.30	105.07	3.77	112.08	Tied to	MS	U1483B-12H
13H	110.80	115.40	4.60	116.612	Tied to	MS	U1483A-12H
14H	120.30	126.36	6.06	127.155	Tied to	MS	U1483A-13H
15H	129.80	138.01	8.21	138.848	Tied to	MS	U1483A-14H
16H	139.30	148.91	9.61	154.84	Tied to	MS	U1483B-16H
17H	148.80	160.05	11.25	166.41	Tied to	MS	U1483B-17H
18H	158.30	171.43	13.13	178.12	Tied to	MS	U1483C-18H
19H	167.80	182.00	14.20	183.156	Tied to	MS	U1483A-18H
20H	177.30	192.77	15.47	199.43	Tied to	MS	U1483B-20H
21H	186.80	203.16	16.36	204.92	Tied to	MS	U1483A-20H
23H	199.30	217.04	17.74		Set; GR = 1.089		U1483C-21H
24H	208.80	227.38	18.58		Set; GR = 1.089		U1483C-23H
25H	218.30	237.31	19.01	242.159	Tied to	MS	U1483B-24H
26H	227.80	248.34	20.54	252.63	Tied to	MS	U1483B-25H
27H	237.30	258.78	21.48	262.47	Tied to	MS	U1483B-26H
28H	246.80	275.48	28.68	278.73	Tied to	MS	U1483A-27H
29H	256.30	287.02	30.72	288.89	Tied to	MS	U1483B-29H
30H	265.80	302.11	36.31	305.46	Tied to	MS	U1483B-30H
31H	275.30	315.68	40.38	316.21	Tied to	MS	U1483B-31H

from 239.8 to 266.8 m CCSF (Figures **F35**, **F36**; Table **T22**). We did not construct splices in two intervals (211.5–239.8 m CCSF and deeper than 266.8 m CCSF) that had WRMSL data variations indicating there was no stratigraphic continuity between holes due to soft-sediment deformation. We estimated offsets for the cores within the deformed intervals, as explained below.

The CCSF scale is anchored to the mudline of Core 363-U1483C-1H, which is assigned a depth of 0 m CCSF. From this anchor, we worked downhole, using Correlator to establish a composite stratigraphy on a core-by-core basis. The match between holes is very well constrained within the spliced intervals (0–211.5 and 239.8–266.8 m CCSF). The most tentative splice tie points are those that connect Cores 363-U1483A-4H to 363-U1483B-5H and 363-U1483B-5H to 363-U1483A-5H because of the very low amplitude variations in all data available for correlation. We approached the construction of the splice mainly by using Hole U1483B as the "backbone" where possible (0–112.08, 151.6–211.5, and 239.8–266.4 m CCSF) and using Hole U1483A to fill the core gaps in most sections. However, there were a few places where we decided to use Hole U1483C for the splice because it provided the most definitive splice tie points. We did not have time to build a second splice, but it appears that, if needed, a nearly complete second splice that does not require material from the first splice could be constructed as part of postcruise research. We have provided the exact position of the tie points that we used to determine the offsets for cores that were not used in the splice (Table **T21**); this information will make it easier for studies that utilize samples from intervals outside the splice to compare data to records from the splice.

Figure F34. Spliced NGR data plotted on spliced core images (core photo generated using CODD; Wilkens et al., 2017), Site U1483. cps = counts per second.

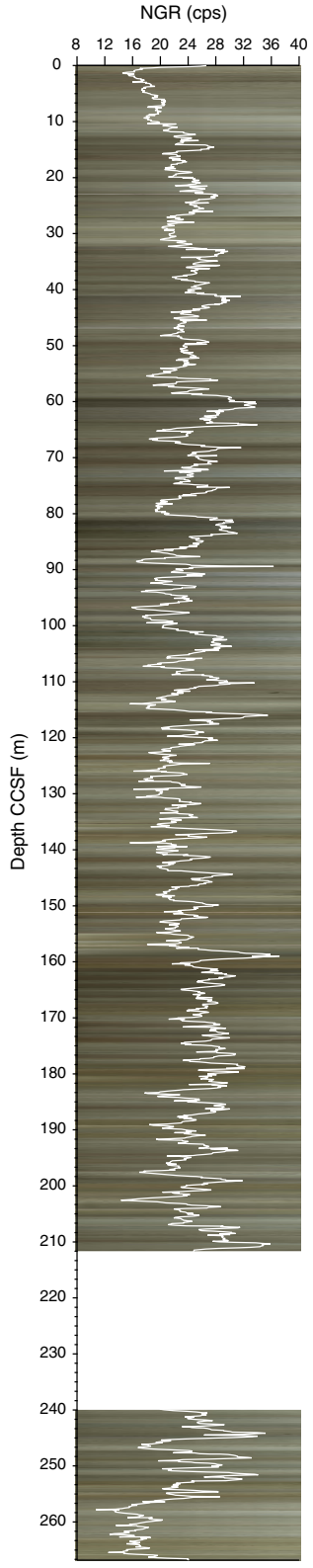

Figure F35. WRMSL MS for Holes U1483A–U1483C divided into 50 m intervals. Upper panel shows the MS splice constructed by combining data from all holes. (Continued on next three pages.)

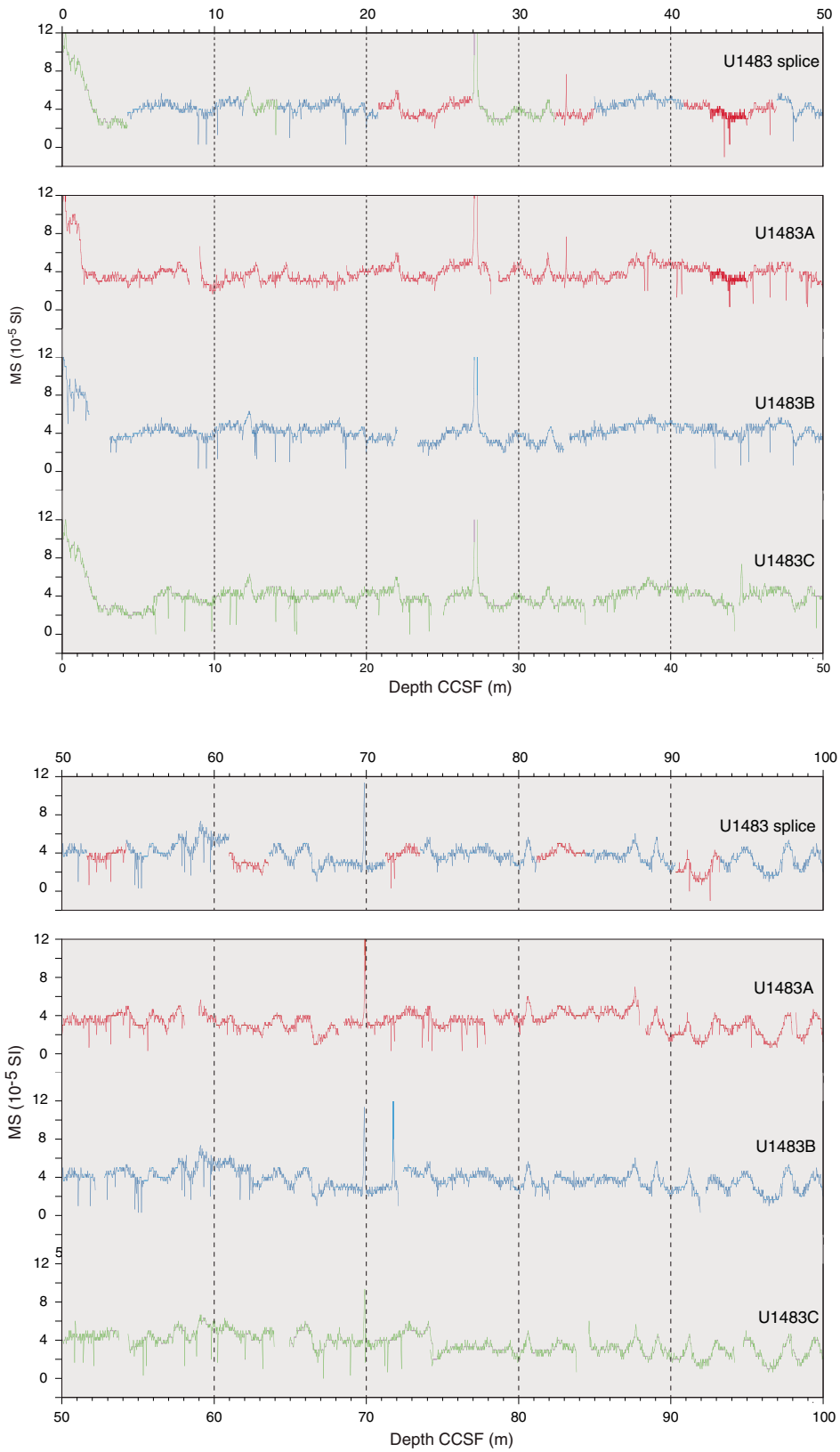

Figure F35 (continued). (Continued on next page.)

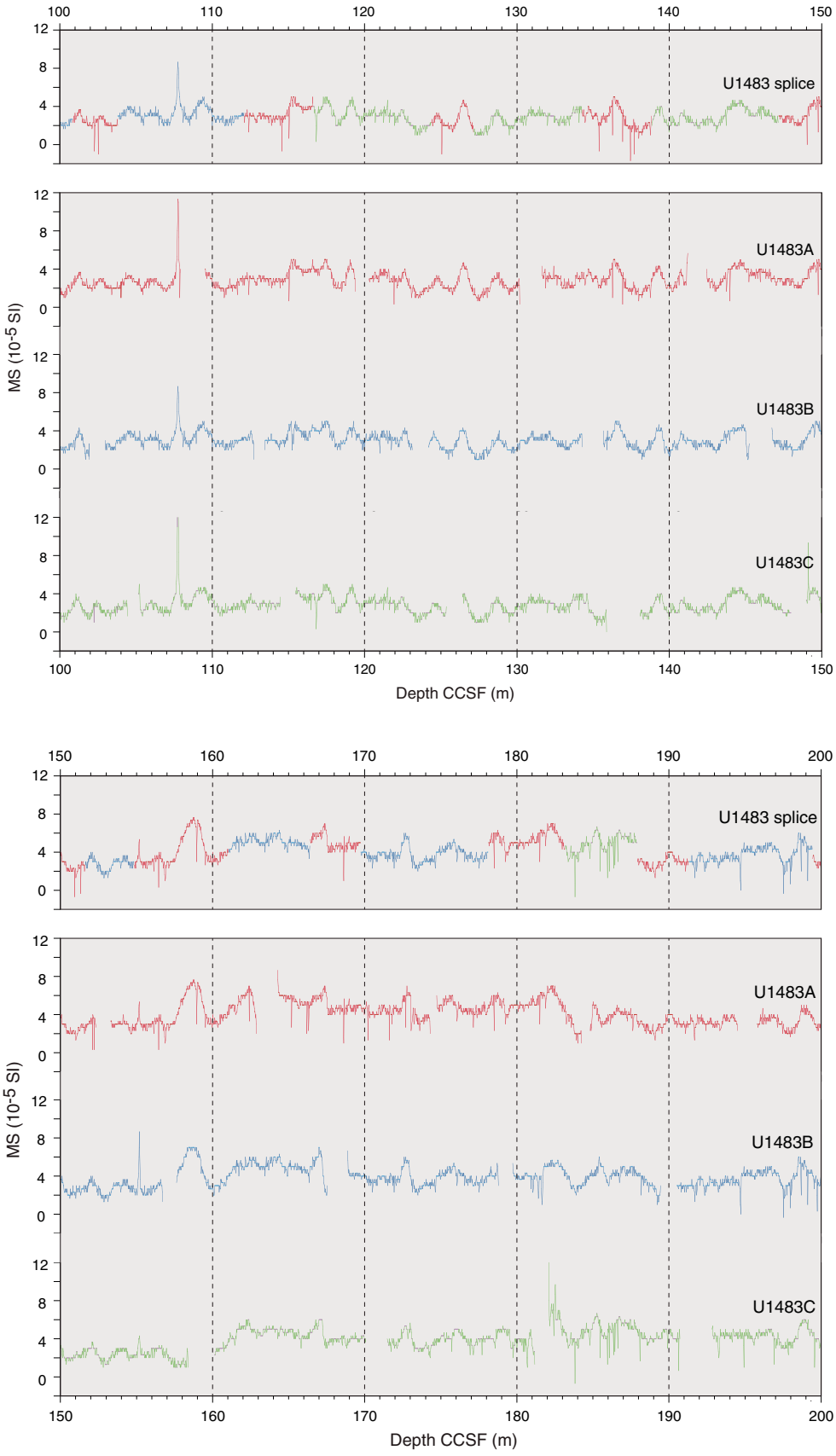

Figure F35 (continued). (Continued on next page.)

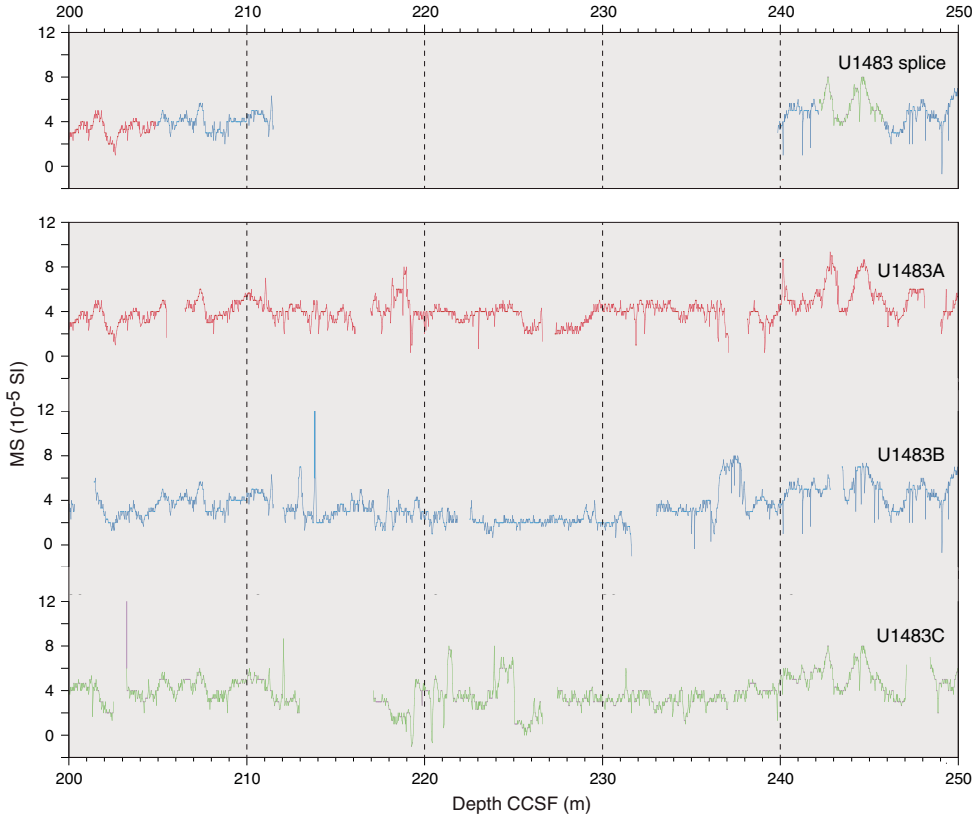

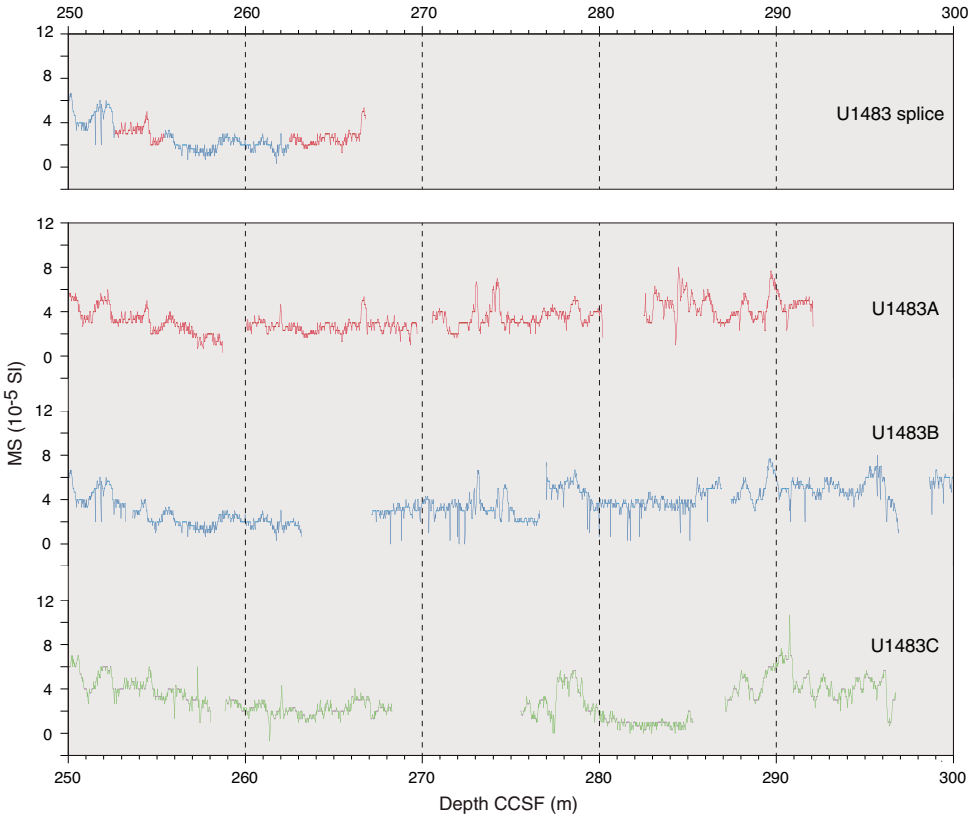

Figure F35 (continued).

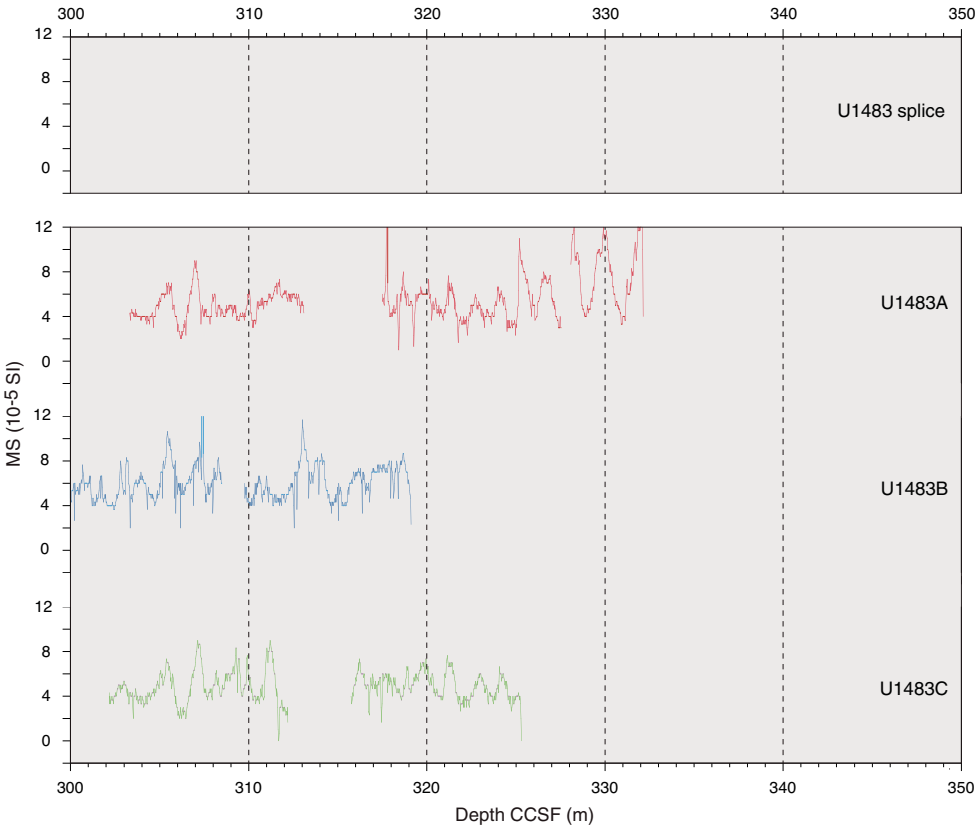

We constructed the splice only for the intervals with undeformed sediment (0.0–211.5 and 239.8–266.8 m CCSF). Within intervals of deformed sediment where we could not make correlations with confidence, we simply determined core-top offsets (211.5–239.8 m CCSF and deeper than 266.8 m CCSF). We ended the upper, longer splice at 211.5 m CCSF, the depth at the bottom of Core 363-U1483B-21H, because below this point visual confirmation of deformed structures in the sediment is evident (see **Core description**) and features detected in the WRMSL data could not be correlated between holes. Therefore, the offsets (Table **T21**) for the tops of the cores within this first deformed interval (211.5–239.8 m CCSF) were set using the growth factor from the previous core within the splice. The offsets for Cores 363-U1483B-22H, 23H, and 24H were set using 1.104, the growth factor of Core 363-U1483B-21H. The offsets for the tops of Cores 363-U1483A-22H and 23H were set using 1.092, the growth factor of Core 363-U1483A-21H. Offsets for Cores 363-U1483C-23H and 24H were set using 1.089, the growth factor of Core 363-U1483C-21H. The top of the next spliced interval occurs at 239.8 m CCSF, the point where the overlying deformed interval ends (Section 363-U1483B-24H-5, 143 cm). The bottom of this second, deeper spliced interval is at 266.8 m CCSF, the point where deformation begins again (Section 363-U1483A-26H-5, 134 cm).

Within the lowest deformed package of sediment (266.8 m CCSF to the bottom of recovered section) many intervals have WRMSL data features that do not correlate across holes, but there are a few features that do correlate. Thus, even though we did not construct a splice for this lowest deformed interval, we determined core offsets to place these cores on the CCSF scale. Our strategy was to use a growth factor to establish offsets for cores that did not correlate with cores in other holes and to use a tie point to establish offsets for cores that had some WRMSL data features that correlated to those in other holes. The offset for Cores 363-U1483A-27H and 28H was set using 1.100, the growth factor of Core 363-U1483A-26H. The offsets for Cores 363-U1483B-27H and 28H, as well as Core 363-U1483C-28H, were determined by correlating features in them to features in Core 363-U1483A-27H. The offsets for Cores 363-U1483B-29H and 363-U1483C-29H were determined using correlation tie points across holes. Core 363-U1483B-30H did not correlate to any other cores, so its offset was set using 1.114, the growth factor of Core 363-U1483B-29H. The offsets of Cores 363-U1483C-30H and 363-U1483A-29H were determined using correlation tie points across holes. We continued with this approach to the bottom of the holes; the offsets for Cores 363-U1483C-31H and 363-U1483A-30H were determined using correlation tie points across holes, and the offset for Cores 363-U1483B-31H and 363-U1483A-31H both had to be set using growth factors based on Cores 363-U1483B-30H and 363-U1483A-30H, respectively. More details are provided in the affine table (Table **T21**).

The splice interval table (Table **T22**) is intended to provide a sampling plan that can be used to generate high-resolution continuous records with minimal gaps; however, an "off-splice" sampling plan was also designed, mainly for low-resolution studies. An explanation of the strategy used to determine the off-splice sampling plan and a table of core intervals that should be used for off-splice sampling can be found in OFFSPLICE in **Supplementary material**.

The cumulative offset between the mbsf and CCSF depth scales is nearly linear (Figure **F37A**), but close inspection of the cumulative offset as a function of depth (mbsf) (Figure **F37B**) shows that, compared to the upper section (0 to ~60 mbsf), the lower section

Figure F36. Spliced L*, NGR, and WRMSL MS and GRA bulk density data, Site U1483. cps = counts per second.

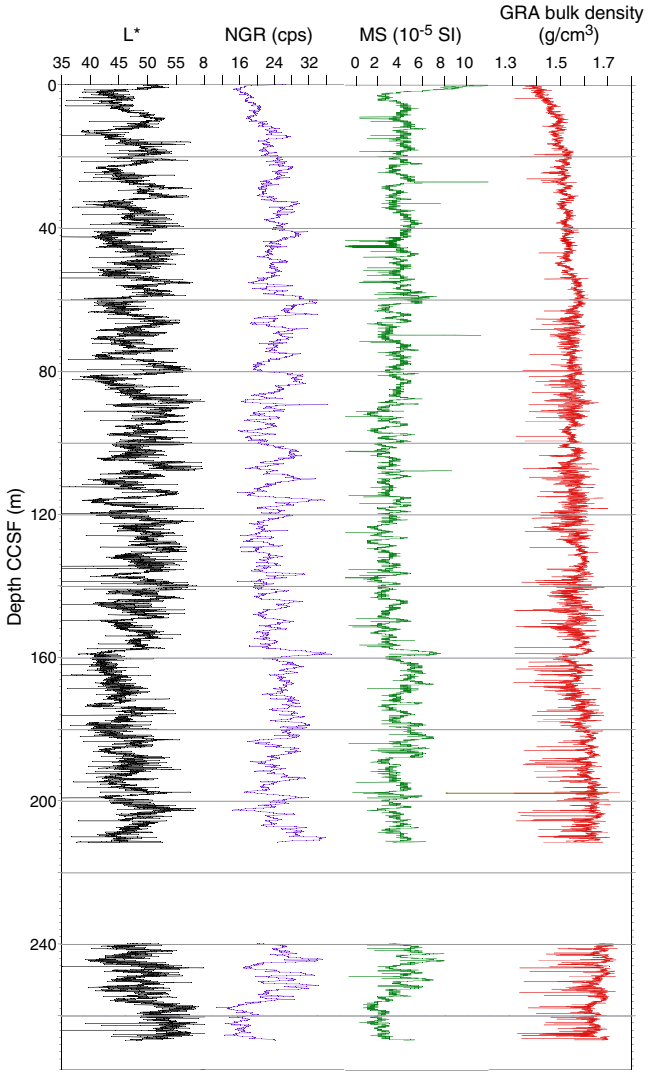

has a greater growth factor because of expansion associated with the release of overburden combined with methane gas expansion. This expansion is most prominent near the sulfate–methane transition zone (at ~55 mbsf at this site; see **Geochemistry**). The growth factors deeper than 243 mbsf are strongly affected by making hole-to-hole correlations within an interval of deformation where thinning and thickening of sediment packages, rather than core expansion, mainly affect the core offsets. Calculation of mass accumulation rates based on the CCSF scale should account for the expansion by dividing apparent depth intervals by the appropriate growth factor.

Table T22. Splice intervals, Site U1483. * = deformation below the end of this spliced interval and until splice starts again at 239.84 m CCSF, † = sediment deformation below the end of this spliced interval and to the bottom of all holes. Note that although offsets were determined for the entire site, stratigraphic continuity occurs only in the intervals for which we constructed splices. MS = magnetic susceptibility. **Download table in CSV format.**

Top of splice interval			Bottom of splice interval				
Hole, core, section, interval (cm)	Depth (mbsf)	Depth CCSF (m)	Hole, core, section, interval (cm)	Depth (mbsf)	Depth CCSF (m)	Splice type	Data used
363-			363-				
U1483C-1H-1, 0.00	0.00	0.00	U1483C-1H-3, 127.90	4.28	4.28	Tie	MS
U1483B-2H-1, 120.30	3.20	4.28	U1483B-2H-7, 9.50	10.89	11.96	Tie	MS
U1483C-2H-5, 6.80	12.37	11.96	U1483C-2H-6, 76.50	14.57	14.16	Tie	MS
U1483B-3H-2, 19.40	13.19	14.16	U1483B-3H-6, 81.60	19.82	20.78	Tie	MS
U1483A-3H-2, 76.40	20.36	20.78	U1483A-3H-6, 93.80	26.54	26.95	Tie	MS
U1483C-4H-2,47.90	27.28	26.95	U1483C-4H-5, 138.20	32.68	32.36	Tie	MS
U1483A-4H-3, 93.20	31.37	32.36	U1483A-4H-5, 69.90	33.98	34.96	Tie	MS
U1483B-5H-2, 20.50	32.21	34.96	U1483B-5H-6, 27.60	38.10	40.86	Tie	MS
U1483A-5H-2, 108.20	39.58	40.86	U1483A-5H-7, 6.20	45.68	46.96	Tie	MS
U1483B-6H-4, 14.80	44.49	46.96	U1483B-6H-7, 43.00	49.16	51.63	Tie	MS
U1483A-6H-3, 43.10	49.86	51.63	U1483A-6H-5, 18.50	52.46	54.22	Tie	MS
U1483B-7H-2, 3.20	50.99	54.22	U1483B-7H-6, 94.60	57.76	60.99	Tie	MS
U1483A-7H-2, 66.60	58.19	60.99	U1483A-7H-4, 41.50	60.78	63.57	Tie	MS
U1483B-8H-1, 120.30	60.20	63.57	U1483B-8H-7, 12.70	67.88	71.25	Tie	MS
U1483A-8H-3, 29.40	68.74	71.25	U1483A-8H-4, 116.50	71.03	73.53	Tie	MS
U1483B-9H-1, 116.80	69.67	73.53	U1483B-9H-7, 6.80	77.33	81.19	Tie	MS
U1483A-9H-3, 8.60	78.00	81.19	U1483A-9H-5, 49.60	81.23	84.42	Tie	MS
U1483B-10H-2,77.30	80.22	84.42	U1483B-10H-6, 82.90	86.11	90.31	Tie	MS
U1483A-10H-2, 63.90	86.64	90.31	U1483A-10H-4, 75.00	89.55	93.22	Tie	MS
U1483B-11H-1, 98.70	88.49	93.22	U1483B-11H-6, 132.10	96.11	100.84	Tie	MS
U1483A-11H-2, 122.60	96.79	100.84	U1483A-11H-4, 125.20	99.74	103.80	Tie	MS
U1483B-12H-1, 88.90	97.89	103.80	U1483B-12H-7, 42.30	106.17	112.08	Tie	MS
U1483A-12H-2, 115.50	106.22	112.08	U1483A-12H-5, 122.70	110.75	116.61	Tie	MS
U1483C-13H-1, 121.00	112.01	116.61	U1483C-13H-7, 24.20	119.75	124.35	Tie	MS
U1483A-13H-3, 125.60	117.23	124.35	U1483A-13H-5, 115.70	120.03	127.16	Tie	MS
U1483C-14H-1, 79.90	121.10	127.16	U1483C-14H-6, 81.40	128.19	134.25	Tie	MS
U1483A-14H-2, 122.60	125.29	134.25	U1483A-14H-6, 7.40	129.88	138.85	Tie	MS
U1483C-15H-1, 83.80	130.64	138.85	U1483C-15H-7, 49.20	138.95	147.16	Tie	MS
U1483A-15H-4, 46.70	136.90	147.16	U1483A-15H-7, 52.70	141.35	151.61	Tie	MS
U1483B-16H-4, 58.70	139.95	151.61	U1483B-16H-6, 87.30	143.17	154.84	Tie	MS
U1483A-16H-2, 18.20	143.20	154.84	U1483A-16H-6, 66.70	149.41	161.04	Tie	MS
U1483B-17H-3, 54.10	147.97	161.04	U1483B-17H-7, 4.80	153.34	166.41	Tie	MS
U1483A-17H-2, 74.40	153.31	166.41	U1483A-17H-4, 102.10	156.63	169.73	Tie	MS
U1483B-18H-1, 91.60	154.92	169.73	U1483B-18H-7, 56.30	163.31	178.12	Tie	MS
U1483A-18H-3, 52.10	164.06	178.12	U1483A-18H-6, 125.30	169.09	183.16	Tie	MS
U1483C-19H-1, 115.80	168.96	183.16	U1483C-19H-5, 25.30	173.71	187.91	Tie	MS
U1483A-19H-3, 26.10	173.26	187.91	U1483A-19H-5, 75.90	176.66	191.31	Tie	MS
U1483B-20H-1, 84.80	173.85	191.31	U1483B-20H-7,36.90	181.97	199.43	Tie	MS
U1483A-20H-3, 113.30	183.30	199.43	U1483A-20H-7, 82.10	188.79	204.92	Tie	MS
U1483B-21H-3, 71.30	186.08	204.92	U1483B-21H-7,138.00	192.69	211.53	End*	
U1483B-24H-5, 143.00	217.89	239.84	U1483B-24H-7, 87.20	220.21	242.16	Tie	MS
U1483C-25H-4, 57.70	223.15	242.16	U1483C-25H-6, 136.00	226.81	245.82	Tie	MS
U1483B-25H-2, 108.40	222.93	245.82	U1483B-25H-7, 61.90	229.74	252.63	Tie	MS
U1483A-25H-3, 86.30	230.81	252.63	U1483A-25H-5, 73.90	233.62	255.43	Tie	MS
U1483B-26H-2, 46.30	231.87	255.43	U1483B-26H-7, 69.40	238.91	262.47	Tie	MS
U1483A-26H-2,122.80	239.08	262.47	U1483A-26H-5, 134.00	243.41	266.81	End†	

Figure F37. A. Comparison of mbsf and composite depth scales in the Site U1483 splice (0–238.8 m CCSF). B. Comparison of the growth of cumulative depth offset and mbsf depth scale. Shaded areas are intervals with soft-sediment deformation where we did not construct splices.

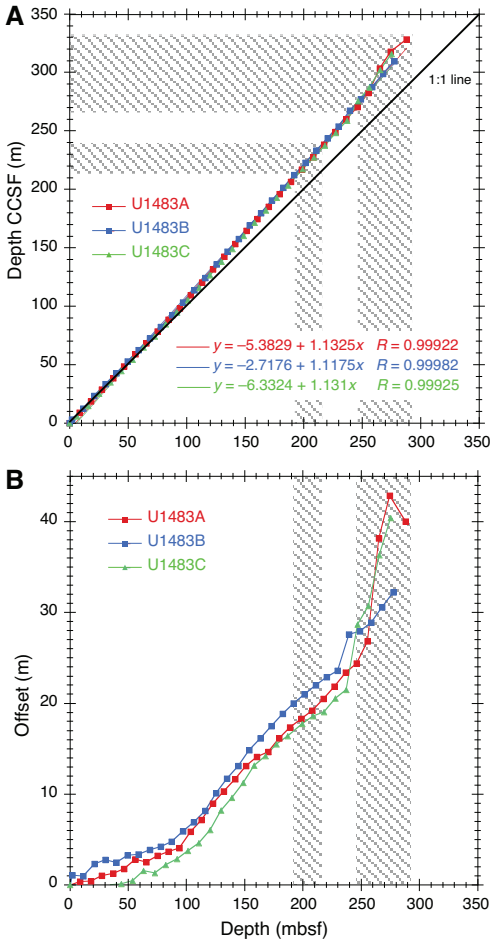

Geochemistry

Site U1483 was cored on the northwest Australian margin, ~260 km from Site U1482. The dominant processes that influence the interstitial water geochemistry at Site U1483 are similar to those observed at Site U1482, including sulfate (SO_4) reduction and methanogenesis of organic matter and interactions with clay and biogenic minerals. As observed at Site U1482, the clay-rich sediment at Site U1483 reduces diffusion, leading to good preservation of reaction profiles. For detailed background on organic matter remineralization and clay mineral alteration, see **Geochemistry** in the Site U1482 chapter (Rosenthal et al., 2018b).

Elevated methane concentration was found in headspace gas samples at Site U1483. High methane/ethane ratios suggest that the methane is mostly of biogenic origin. Calcium carbonate ($CaCO_3$) remains the dominant biogenic sediment component (average = 59 wt%) throughout the entire record. The total organic carbon (TOC) content of samples ranges from 0.4 to 1.4 wt%.

Results

Volatile hydrocarbons

Headspace gas samples were taken at a frequency of one sample per core in Hole U1483A as part of the routine environmental protection and safety-monitoring program (Table **T23**; Figure **F38**). Methane concentration varies between 9 and 53 ppmv from 7.5 to 36.2 mbsf, gradually increases between 45.6 and 140.8 mbsf to a maximum of 102,336 ppmv, and then decreases to ~11,200 ppmv at 289.7 mbsf. Ethane and propane occur in trace amounts throughout the cores. The C_1/C_2 ratio abruptly increases from 45.6 mbsf to a peak at 102.9 mbsf and then gradually decreases downhole with increasing maturity. The high C_1/C_2 ratios below 55.2 mbsf suggest that the methane is mostly of biogenic origin, rather than thermogenic.

Table T23. Volatile hydrocarbon concentrations, Hole U1483A. **Download table in CSV format.**

Figure F38. Methane, ethane, propane, and C_1/C_2 ratio profiles, Hole U1483A.

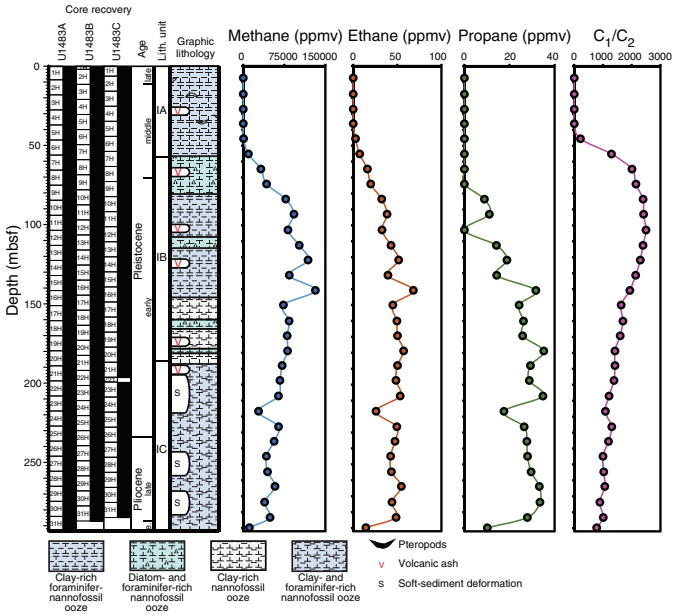

Bulk sediment geochemistry

$CaCO_3$, inorganic carbon (IC), TOC, and total nitrogen (TN) were measured on sediment samples from Hole U1483A (Table **T24**; Figure **F39**). $CaCO_3$ content ranges between 38 and 78 wt% with an average of 59 wt%. $CaCO_3$ gradually increases downhole in lithologic Subunits IA and IB. This trend is punctuated by a slight drop in $CaCO_3$ content from 53.6% to 44.0% at 147.1 mbsf and slightly lower values near the base of lithologic Subunit IB. The $CaCO_3$ content increases in Subunit IC, with a slight decrease (38 wt%) at 228.4 mbsf, before decreasing again from ~250 mbsf to the bottom of the hole at ~290 mbsf. We observed a general correspondence between $CaCO_3$ content and L* in the upper ~100 mbsf and with b* below ~200 mbsf.

TOC ranges between ~0.3 and 1.3 wt% with an average of 0.88 wt%, showing no discernible downhole trend. However, one sample has relatively high TOC (2.6 wt%; 363-U1483A-25H-1, 125–127 cm; 28.35 mbsf) and very low $CaCO_3$ content (38.0 wt%). The ratio of TOC to TN (C/N ratio) ranges from 4 to 38 with an average of 19 (Figure **F39**). The C/N ratio in most samples is higher than 10, possibly suggesting that the organic matter deposited at Site U1483 is predominately supplied by terrestrial input; however, caution should be taken when interpreting TOC and C/N data calculated from the subtraction method.

Table T24. Carbon, nitrogen, and carbon/nitrogen (C/N) ratio, Hole U1483A. **Download table in CSV format.**

Figure F39. Calcium carbonate, TOC, TN, and C/N ratio profiles, Hole U1483A. Ranges of marine and terrestrial organic matter based on C/N ratio are indicated by annotated bars at the base of the C/N ratio profile.

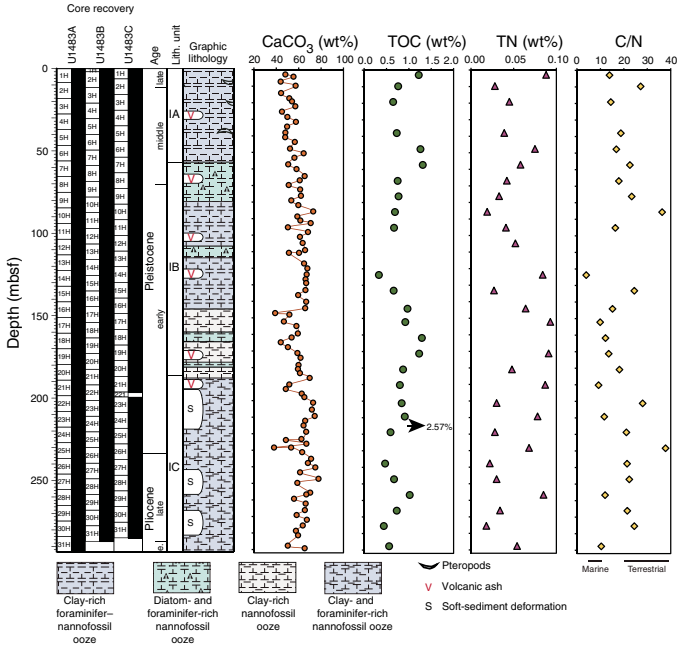

Interstitial water chemistry

A total of 35 whole-round samples and 1 mudline sample were taken from Hole U1483A for interstitial water analyses, spanning from 4.5 to 283.3 mbsf. For ammonium (NH_4) analysis, a number of samples from Site U1482 had NH_4 concentrations that fell above our standard curve. Because of concerns with the calibration curve linearity at concentrations >3.0 mM and evidence of high NH_4 concentration from the ion chromatograph run, sample aliquots were diluted so that their concentrations would fall within the range of the calibration curve, and the total volume of the aliquots was sufficient for longer take-up times. This practice was adopted for the remainder of the expedition when ion chromatograph peaks indicated high NH_4 at a site. Samples analyzed for phosphate (PO_4) were not diluted. Interstitial water chemistry data are reported in Table **T25**.

Chlorinity and salinity

Chloride (Cl) concentration increases steadily downhole from a mudline value of 557.4 mM to a local maximum of 567.4 mM at 55.1 mbsf and then decreases to 563.8 mM at 83.5 mbsf. Below that, Cl increases monotonically, reaching a maximum value of 597 mM at 238.3 mbsf (Figure **F40**). This 7% increase from the top of the hole to the bottom is larger than the 3% increase observed over the equivalent time interval at Site U1482. Water uptake through the alteration of kaolinite to illite may be responsible for the downhole increase in Cl, but upward diffusion of waters enriched in Cl from alteration of material at depth also likely influences the profile. Salinity has minor downhole variations (not shown), ranging from 36 to 34 between 0 and ~150 mbsf, and then remaining constant at 35 below ~150 mbsf, with one reading of 36 at 283.3 mbsf.

Alkalinity and pH

Site U1483 has downhole alkalinity and pH profiles that are similar to each other, particularly in the upper ~50 mbsf (Figure **F40**).

Table T25. Interstitial water geochemical data, Hole U1483A. **Download table in CSV format.**

The strong coupling of these two parameters can be explained in part by the rapid transitions through the stages of organic matter remineralization. Alkalinity increases from a mudline value of 2.4 mM to a maximum of 17.9 mM at 45.6 mbsf, whereas pH increases from 7.7 to 8.4 over the same range. The manganese (Mn) and sulfate (SO_4) profiles over the same interval indicate transitions from suboxic to anoxic organic matter remineralization and nearly complete SO_4 depletion by 55.1 mbsf. As observed at Site U1482, the sulfate–methane transition zone (SMTZ) is marked by peaks in alkalinity and pH. Alkalinity and pH gradually decrease over the remainder of the hole, reaching 3.3 and 7.6 mM, respectively, at the base of the hole (~283.3 mbsf).

Minor shifts in alkalinity and pH are observed at ~200 and ~245 mbsf (gray shading in Figure **F40**). These two depths coincide with the locations of two intervals of soft-sediment deformation (see **Core description**) where biostratigraphic evidence suggests that a substantial portion of the original sedimentary sequence has been removed (see **Biostratigraphy**). Changes in several other interstitial water profiles were observed at the same depths, indicating a tight link between lithology and interstitial water chemistry (see **Discussion**).

Sulfate and barium

SO_4 concentration decreases from seawater-like values (29.1 mM) at the mudline to almost complete depletion at the SMTZ (55.1 mbsf). The convex shape of the SO_4 profile indicates that anaerobic oxidation of methane is the dominant sink for interstitial water SO_4 at Site U1483 (Figure **F40**). Similar to what was observed at Site U1482, barium (Ba) concentration increases sharply below the SMTZ downhole to 74.0 mbsf (maximum = 431.66 µM), indicating barite dissolution within the methanogenesis zone. An altered gypsum-bearing authigenic concretion possibly containing barite was found at the same depth as the peak of dissolved Ba (see **Core description**) and may correspond to a former barite front (i.e., related to a paleo-SMTZ) that is currently undergoing partial dissolution. Deeper than 74.1 mbsf, Ba concentration decreases to 352.64 µM at 112.4 mbsf, followed by a gradual increase downhole to 406.85 µM at the base of Hole U1483A.

Phosphate, ammonium, and bromide

Phosphate (PO_4) concentration increases from 1.2 µM at the mudline to a peak of 24.0 µM at 45.6 mbsf (Figure **F40**), coincident with peaks in alkalinity and pH and depletion of SO_4. In contrast to Site U1482, the trend in PO_4 here mirrors changes in pH and alkalinity above the SMTZ, indicating that PO_4 released into interstitial water during organic matter degradation is not concomitantly reprecipitated as extensively as is proposed for Site U1482 (see **Geochemistry** in the Site U1482 chapter [Rosenthal et al., 2018b]). Deeper than 45.6 mbsf, PO_4 decreases sharply until ~103 mbsf and then more gradually to a value of 0.9 µM at 273.7 mbsf (PO_4 in the deepest sample is below detection limit). The observed PO_4 profile is influenced by remineralization of organic matter in the upper portion of the sedimentary sequence and diffusion in the lower portion of the sediment.

Ammonium (NH_4) and bromide (Br) concentrations both increase with depth, consistent with their release from organic matter during remineralization (Figure **F40**); however, the NH_4 profile shows two distinct features that appear to be related to changes in

Figure F40. Interstitial water concentration profiles, Hole U1483A. Mudline iron and manganese concentrations were below detection limit and are not plotted. The arrow on the ammonium profile indicates the change in slope in NH_4^+ concentration, which is commensurate with a change in lithology within Subunit IB. Black stars = mudline samples, dashed line = SMTZ, gray shading = intervals of soft-sediment deformation.

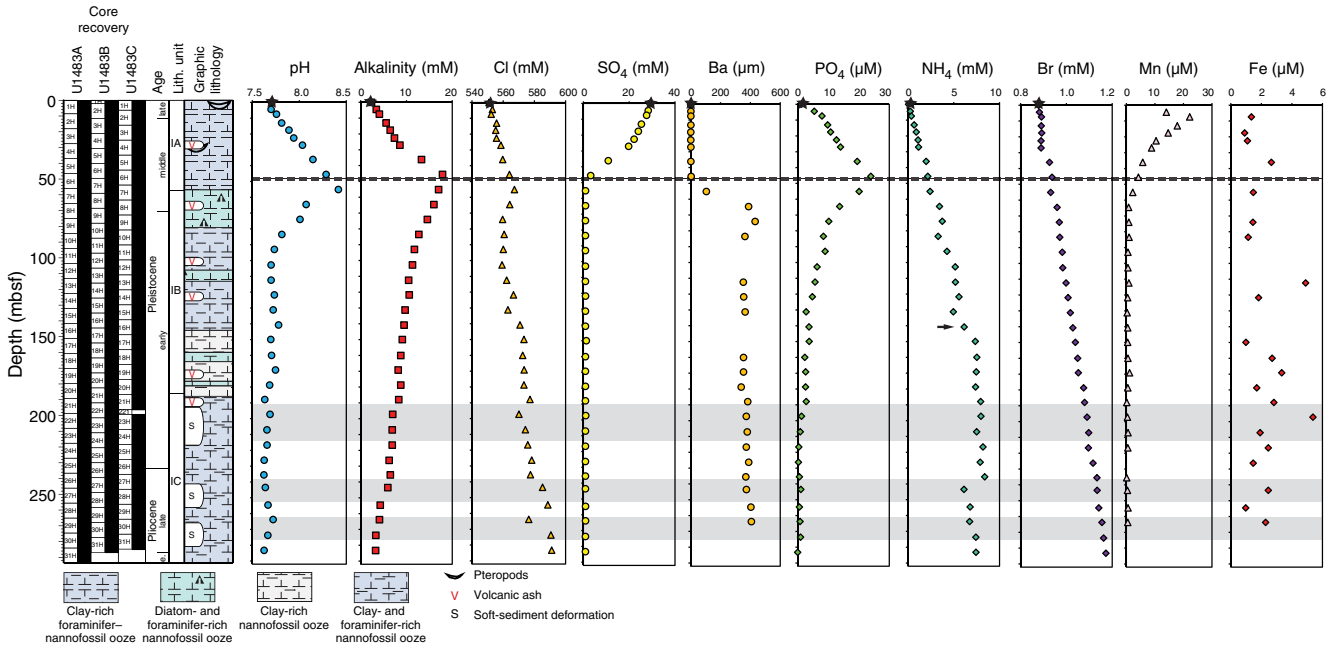

lithology rather than organic matter (see **Core description**). The first of these occurs at ~145 mbsf, where a shift in lithology from clay-rich and foraminifer-rich nannofossil ooze above to predominantly nannofossil clay or diatom-rich nannofossil clay below was observed. The higher slope in the NH_4 profile deeper than ~145 mbsf suggests reduced diffusion rates related to higher clay content and decreased permeability. The Br profile is not characterized by a similar change at this depth, as would be expected if both parameters were controlled primarily by organic matter degradation. A second notable feature in the NH_4 profile occurs at 243.5 mbsf, the location of one of the two prominent intervals of deformed sediment in the hole, where NH_4 concentration drops abruptly from 8.4 to 6.1 µM (see **Discussion**).

Compared to the NH_4 profile, the Br profile shows a far more monotonic increase over the entire hole, with the exception of the upper ~30 mbsf, where little to no change in concentration is observed (Figure **F40**). This could indicate that Br is hosted in the more refractory phases of organic matter, which is degraded after the fresh, labile compounds are remineralized (Henrichs, 1992).

Manganese and iron

Mn concentration increases from the mudline to a maximum of 22.2 µM at 7.5 mbsf within the zone of suboxic organic matter remineralization and then sharply decreases to 0.8 µM by 64.6 mbsf (Figure **F40**). As with PO_4, Mn concentration is higher at Site U1483 relative to Site U1482, and the Mn peak and subsequent downhole depletion occur at shallower depths in the sediment sequence, in agreement with the trends observed in alkalinity, pH, SO_4, and Ba. Deeper than 64.6 mbsf, Mn concentration is low and constant at <1.1 µM. The iron (Fe) profile is characterized by low concentration and a high degree of scatter, making quantitative or qualitative observations about Fe variability difficult (Figure **F40**). The sedimentologists did not observe pyrite in the Site U1483 cores, but some foraminifer samples from the deeper parts of the hole contained large amounts of pyrite (see **Biostratigraphy**). Hence, the low Fe concentration may not be due to extensive pyritization in the sediment as hypothesized for Site U1482.

Potassium, magnesium, and calcium

As at Site U1482, potassium (K) concentration at Site U1483 increases slightly from the mudline value of 10.6 mM to a concentration slightly higher than that of seawater (11.7 mM) in the uppermost ~10 mbsf, suggesting an input of K to the interstitial water from the shallowest sediments (Figure **F41**). As observed in the magnesium (Mg) and strontium (Sr) profiles, K concentration remains constant downhole to ~27 mbsf, where a steady linear decrease begins and continues to a minimum concentration of 6.0 mM at the bottom of Hole U1483A. As at Site U1482, stoichiometric relationships between Mg and K concentrations suggest a common process influencing their profiles, such as clay mineral ion exchange, clay authigenesis (e.g., conversion from kaolinite to illite), and/or a sink at a depth below the deepest material recovered from Site U1483.

Mg concentration remains fairly constant (~52 mM) downhole to 27.0 mbsf (Figure **F41**). Below 27.0 mbsf, Mg concentration decreases throughout the sedimentary sequence to a minimum value of 24.6 mM at the bottom of Hole U1483A. Mg concentration decreases more steeply between 27.0 and 74.0 mbsf but stabilizes toward the base of the hole, suggesting a close balance between uptake and release of Mg or a diffusion-dominated signature over this depth interval.

The calcium (Ca) profile displays a decrease from seawater-like values at the mudline (10.8 mM) to ~4 mM just above the depth of the SMTZ (55.1 mbsf), which, together with alkalinity data, is suggestive of anaerobic oxidation of methane (AOM)-driven carbonate precipitation (Figure **F41**). Mg and Sr do not show any pronounced depletion or enrichment at the same depth, suggesting that calcite forms preferentially at the SMTZ, as opposed to high-Mg calcite, dolomite, or aragonite. Deeper than 45.6 mbsf, Ca concentration increases progressively to 8.5 mM between 235.5 and 243.5 mbsf be-

Figure F41. Interstitial water concentration profiles, Hole U1483A. Black stars = mudline samples, dashed line = SMTZ, gray shading = intervals of soft-sediment deformation.

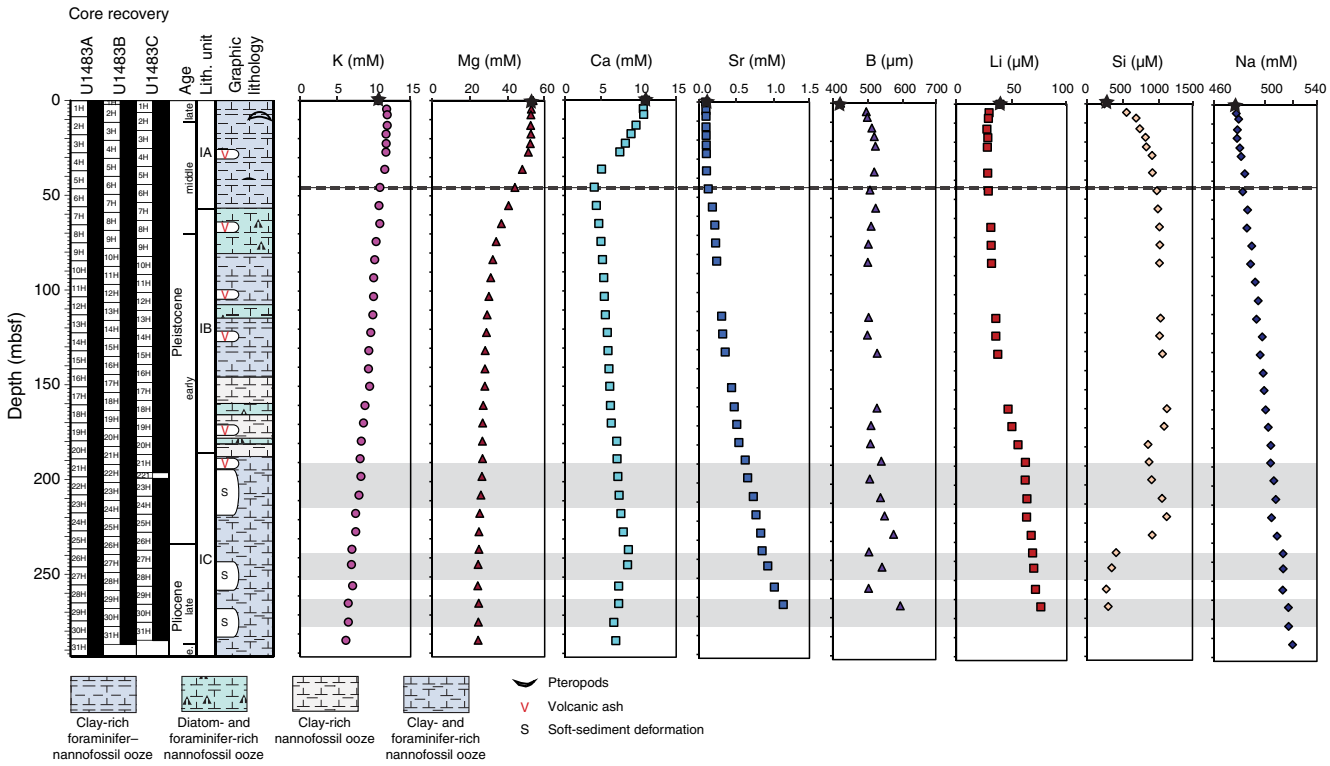

fore decreasing to 6.9 mM at the base of Hole U1483A. Calcareous microfossil preservation is excellent to very good throughout the recovered stratigraphy at Site U1483, with minor dissolution and overgrowth reported only below ~200 mbsf (see **Biostratigraphy**).

Strontium and boron

Sr concentration is approximately constant (average = 93.6 mM) between the mudline and 27.0 mbsf (Figure **F41**). Deeper than 27.0 mbsf, Sr progressively increases to a maximum concentration of 1143.5 mM at the bottom of Hole U1483A. This downhole trend is the inverse of that observed in the Mg profile. The continued increase of Sr with depth suggests an active source of Sr to the interstitial water, likely due to a combination of minor biogenic carbonate dissolution and diffusion from deeper, Sr-enriched sediment.

Although the boron (B) profile at Site U1483 appears less variable than that at Site U1482, the profiles are quite similar over an equivalent time interval. B increases modestly over that interval, from a value of 423.4 µM at the mudline to a maximum of 597 µM at 263.8 mbsf at Site U1483 (Figure **F41**). This is a 41% increase, similar to the 47% increase in interstitial water B concentration observed over the same range at Site U1482. Biogenic carbonate is well preserved throughout the sequence at Site U1483 (see **Biostratigraphy**), which is consistent with the observed moderate downhole increase in B.

Lithium, silica, and sodium

The overall trends in the lithium (Li) profile at Site U1483 (Figure **F41**) are similar to the observed trends in the equivalent depth interval (0–280 mbsf) at Site U1482. Following a slight decrease from a concentration of 39.4 µM at the mudline to 27.5 µM at 13.0 mbsf, Li concentration remains relatively constant over the upper ~30 mbsf, similar to profiles of K, Mg, and Sr. Deeper than ~30 mbsf, Li concentration increases somewhat gradually until 160.0 mbsf then more steeply between 160.0 and the base of the hole. The change of slope occurs near the top of the uppermost interval of soft-sediment deformation (see **Core description** and **Discussion**).

Distinct differences in silica (Si) evident between Sites U1482 and U1483 likely reflect sedimentological differences between the sites. At Site U1482, radiolarians were observed only in the uppermost cores from each hole (see **Biostratigraphy** and **Core description** in the Site U1482 chapter [Rosenthal et al., 2018b]), and the dissolved Si profile reaches a maximum value of 796.6 µM in the upper 100 mbsf before decreasing rapidly downhole to ~250 µM by approximately 200 mbsf. In stark contrast, biogenic silica is present throughout much of Site U1483 (see **Biostratigraphy** and **Core description**), and interstitial water Si concentration increases from 223.9 µM at the mudline to ~1000 µM by 55.1 mbsf (Figure **F41**). Below that, slight variability is observed, with Si concentration averaging ~1000 µM between 55.1 and 226.3 mbsf.

Although the high interstitial water Si at Site U1483 suggests active dissolution of biogenic silica, the appearance of diatoms and radiolarians throughout the entire sedimentary sequence suggests that equilibrium has been reached between the solid and liquid phases of Si at this site. The high interstitial water Si may also have implications for clay mineral alteration/authigenesis because dissolved Si is key for the formation or alteration of many clay minerals. If this type of clay mineral alteration is occurring at Site U1483, interstitial water Si would likely decrease without an additional input of Si (such as dissolution of biogenic silica). However, elevated interstitial water Si concentration throughout most of the record suggests clay mineral alteration and authigenesis may not be as pronounced at Site U1483 compared to Site U1482.

Sodium (Na) concentration decreases linearly from the mudline to the bottom of Hole U1483A (Figure **F41**). Although Na may be influenced by small amounts of clay mineral alteration (see **Geochemistry** in the Site U1482 chapter [Rosenthal et al., 2018b] for detailed background on clay mineral alteration), the linear nature of the increase suggests either uptake of sodium that nearly balances its release or the dominance of diffusion in shaping the profile.

Discussion

The dominant processes influencing the interstitial water profiles at this site include remineralization of organic matter, with rapid transitions through suboxic to anoxic and methanogenic organic matter remineralization, and diffusion. The clay-rich nature of the sediment may reduce the influence of diffusion, resulting in well-preserved gradients in downhole profiles, although trends in Cl and Na indicate a stronger influence of diffusion here than at Site U1482. Downhole trends in K, Ca, Mg, Sr, B, Li, and Si suggest moderate degrees of interaction between interstitial water and biogenic sediment, with clay mineral ion-exchange and diffusion having a more substantial influence at depth.

Several intervals of soft-sediment deformation are observed at Site U1483. In Hole U1483A, deformed sediment occurs at ~193–218 and ~243–258 mbsf. Although lithologically similar to the in situ sediment, the deformed sediment contains a higher percentage of clay (see **Core description**) and has higher bulk density (see **Physical properties**). Changes in several interstitial water profiles are observed at the depths of the deformed sediment intervals, including alkalinity, pH, NH_4, Li, and Si (Figures **F40**, **F41**). Together, these profiles suggest that the denser clay layers influence the reaction/diffusion rates within the deformed intervals. The deformed layers may also act as a "cap," decreasing the interaction between interstitial water above, within, and below the deformed layers and resulting in well-preserved interstitial water gradients that might otherwise have been smoothed out by diffusion.

References

Berggren, W.A., Kent, D.V., Swisher, C.C., III, and Aubry, M.-P., 1995. A revised Cenozoic geochronology and chronostratigraphy. *In* Berggren, W.A., Kent, D.V., Aubry, M.-P., and Hardenbol, J. (Eds.), *Geochronology, Time Scales and Global Stratigraphic Correlation.* Special Publication - SEPM (Society for Sedimentary Geology), 54:129–212. **https://doi.org/10.2110/pec.95.04.0129**

Blum, P., 1997. *Technical Note 26: Physical Properties Handbook—A Guide to the Shipboard Measurement of Physical Properties of Deep-Sea Cores*. Ocean Drilling Program. **https://doi.org/10.2973/odp.tn.26.1997**

Cande, S.C., and Kent, D.V., 1995. Revised calibration of the geomagnetic polarity timescale for the Late Cretaceous and Cenozoic. *Journal of Geophysical Research: Solid Earth,* 100(B4):6093–6095. **https://doi.org/10.1029/94JB03098**

Chaisson, W.P., and Pearson, P.N., 1997. Planktonic foraminifer biostratigraphy at Site 925: middle Miocene–Pleistocene. *In* Shackleton, N.J., Curry, W.B., Richter, C., and Bralower, T.J. (Eds.), *Proceedings of the Ocean Drilling Program, Scientific Results,* 154: College Station, TX (Ocean Drilling Program), 3–31. **https://doi.org/10.2973/odp.proc.sr.154.104.1997**

Dowsett, H.J., 1988. Diachroneity of late Neogene microfossils in the southwest Pacific Ocean: application of the graphic correlation method. *Paleoceanography,* 3(2):209–222. **https://doi.org/10.1029/PA003i002p00209**

Gordon, A.L., 2005. Oceanography of the Indonesian seas and their throughflow. *Oceanography,* 18(4):14–27. **https://doi.org/10.5670/oceanog.2005.01**

Gradstein, F.M., 1992. Legs 122 and 123, northwestern Australian margin—a stratigraphic and paleogeographic summary. *In* Gradstein, F.M., Ludden, J.N., et al., *Proceedings of the Ocean Drilling Program, Scientific Results,* 123: College Station, TX (Ocean Drilling Program), 801–816. **https://doi.org/10.2973/odp.proc.sr.123.110.1992**

Hall, R., 2012. Late Jurassic–Cenozoic reconstructions of the Indonesian region and the Indian Ocean. *Tectonophysics,* 570–571:1–41. **https://doi.org/10.1016/j.tecto.2012.04.021**

Henrichs, S.M., 1992. Early diagenesis of organic matter in marine sediments: progress and perplexity. *Marine Chemistry,* 39(1–3):119–149. **https://doi.org/10.1016/0304-4203(92)90098-U**

Hilgen, F.J., Lourens, L.J., and Van Dam, J.A., 2012. The Neogene period. With contributions by A.G. Beu, A.F. Boyes, R.A. Cooper, W. Krijgsman, J.G. Ogg, W.E. Piller, and D.S. Wilson. *In* Gradstein, F.M., Ogg, J.G., Schmitz, M.D., and Ogg, G.M. (Eds.), *The Geologic Time Scale:* Oxford, United Kingdom (Elsevier), 923–978. **https://doi.org/10.1016/B978-0-444-59425-9.00029-9**

Holbourn, A., Kuhnt, W., Kawamura, H., Jian, Z., Grootes, P., Erlenkeuser, H., and Xu, J., 2005. Orbitally paced paleoproductivity variations in the Timor Sea and Indonesian Throughflow variability during the last 460 kyr. *Paleoceanography,* 20(3):PA3002. **https://doi.org/10.1029/2004PA001094**

Karlin, R., and Levi, S., 1983. Diagenesis of magnetic minerals in recent hemipelagic sediments. *Nature,* 303(5915):327–330. **https://doi.org/10.1038/303327a0**

Keep, M., Harrowfield, M., and Crowe, W., 2007. The Neogene tectonic history of the North West shelf, Australia. *Exploration Geophysics,* 38(3):151–174. **https://doi.org/10.1071/EG07022**

Kuhnt, W., Blümel, M., Boch, R., Dewi, K.T., da Costa Monteiro, F., Dürkop, A., Hanebuth, T., Heidemann, U., Holbourn, A., Jian, Z., van der Kaars, S., Kawamura, H., Kawohl, H., Nürnberg, D., Opdyke, B., Petersen, A., Regenberg, M., Rosenthal, Y., Rühlemann, C., Sadekov, A., Salomon, B., Tian, J., Xu, J., and Zuraida, R., 2005. Cruise Report SO185, VITAL–Variability of the Indonesian Throughflow and Australasian climate history of the last 150000 years, Darwin–Jakarta, September 15 2005–October 06 2005. *IFM-GEOMAR Reports.* **https://doi.org/10.2312/cr_so185**

Kuhnt, W., Holbourn, A., Xu, J., Opdyke, B., De Deckker, P., Röhl, U., and Mudelsee, M., 2015. Southern Hemisphere control on Australian monsoon variability during the late deglaciation and Holocene. *Nature Communications,* 6:5916. **https://doi.org/10.1038/ncomms6916**

McNeill, L.C., Dugan, B., Petronotis, K.E., Backman, J., Bourlange, S., Chemale, F., Chen, W., Colson, T.A., Frederik, M.C.G., Guèrin, G., Hamahashi, M., Henstock, T., House, B.M., Hüpers, A., Jeppson, T.N., Kachovich, S., Kenigsberg, A.R., Kuranaga, M., Kutterolf, S., Milliken, K.L., Mitchison, F.L., Mukoyoshi, H., Nair, N., Owari, S., Pickering, K.T., Pouderoux, H.F.A., Yehua, S., Song, I., Torres, M.E., Vannucchi, P., Vrolijk, P.J., Yang, T., and Zhao, X., 2017. Expedition 362 summary. *In* McNeill, L.C., Dugan, B., Petronotis, K.E., and the Expedition 362 Scientists, *Sumatra Subduction Zone.* Proceedings of the International Ocean Discovery Program, 362: College Station, TX (International Ocean Discovery Program). **https://doi.org/10.14379/iodp.proc.362.101.2017**

Pribnow, D., Kinoshita, M., and Stein, C., 2000. *Thermal Data Collection and Heat Flow Recalculations for Ocean Drilling Program Legs 101–180:* Hanover, Germany (Institute for Joint Geoscientific Research, Institut für Geowissenschaftliche Gemeinschaftsaufgaben [GGA]). **http://www-odp.tamu.edu/publications/heatflow/ODPReprt.pdf**

Rosenthal, Y., Holbourn, A., and Kulhanek, D.K., 2016. *Expedition 363 Scientific Prospectus: Western Pacific Warm Pool.* International Ocean Discovery Program. **https://doi.org/10.14379/iodp.sp.363.2016**

Rosenthal, Y., Holbourn, A.E., Kulhanek, D.K., Aiello, I.W., Babila, T.L., Bayon, G., Beaufort, L., Bova, S.C., Chun, J.-H., Dang, H., Drury, A.J., Dunkley Jones, T., Eichler, P.P.B., Fernando, A.G.S., Gibson, K.A., Hatfield, R.G., Johnson, D.L., Kumagai, Y., Li, T., Linsley, B.K., Meinicke, N., Mountain, G.S., Opdyke, B.N., Pearson, P.N., Poole, C.R., Ravelo, A.C., Sagawa, T., Schmitt, A., Wurtzel, J.B., Xu, J., Yamamoto, M., and Zhang, Y.G., 2018a. Expedition 363 methods. *In* Rosenthal, Y., Holbourn, A.E., Kulhanek, D.K., and the Expedition 363 Scientists, *Western Pacific Warm Pool.* Pro-

ceedings of the International Ocean Discovery Program, 363: College Station, TX (International Ocean Discovery Program). **https://doi.org/10.14379/iodp.proc.363.102.2018**

Rosenthal, Y., Holbourn, A.E., Kulhanek, D.K., Aiello, I.W., Babila, T.L., Bayon, G., Beaufort, L., Bova, S.C., Chun, J.-H., Dang, H., Drury, A.J., Dunkley Jones, T., Eichler, P.P.B., Fernando, A.G.S., Gibson, K.A., Hatfield, R.G., Johnson, D.L., Kumagai, Y., Li, T., Linsley, B.K., Meinicke, N., Mountain, G.S., Opdyke, B.N., Pearson, P.N., Poole, C.R., Ravelo, A.C., Sagawa, T., Schmitt, A., Wurtzel, J.B., Xu, J., Yamamoto, M., and Zhang, Y.G., 2018b. Site U1482. *In* Rosenthal, Y., Holbourn, A.E., Kulhanek, D.K., and the Expedition 363 Scientists, *Western Pacific Warm Pool.* Proceedings of the International Ocean Discovery Program, 363: College Station, TX (International Ocean Discovery Program). **https://doi.org/10.14379/iodp.proc.363.103.2018**

Rowan, C.J., Roberts, A.P., and Broadbent, T., 2009. Reductive diagenesis, magnetite dissolution, greigite growth and paleomagnetic smoothing in marine sediments: a new view. *Earth and Planetary Science Letters,* 277(1–2):223–235. **https://doi.org/10.1016/j.epsl.2008.10.016**

Saito, T., 1976. Geologic significance of coiling direction in the planktonic foraminifer *Pulleniatina. Geology,* 4(5):305–309. **https://doi.org/10.1130/0091-7613(1976)4<305:GSOCDI>2.0.CO;2**

Stagg, H.M.J., and Exon, N.F., 1981. Geology of the Scott Plateau and Rowley Terrace, off northwestern Australia. *Bureau of Mineral Resources, Geology and Geophysics Bulletin,* 213. **http://www.ga.gov.au/corporate_data/62/Bull_213.pdf**

Stoner, J.S., and St-Onge, G., 2007. Magnetic stratigraphy in paleooceanography: reversal, excursion, paleointensity and secular variation. *In* Hillaire-Marcel, C., and de Vernal, A. (Eds.), *Proxies in Late Cenozoic Paleoceanography*: Amsterdam (Elsevier Science), 99–138.

Symonds, P.A., Collins, C.D.N., and Bradshaw, J., 1994. Deep structure of the Browse Basin: implications for basin development and petroleum exploration. *In* Purcell, P.G., and Purcell, R.R. (Eds.), *The Sedimentary Basins of Western Australia: Proceedings of the West Australian Basins Symposium:* Perth, Australia (Petroleum Exploration Society of Australia), 315–331.

Valet, J.-P., Meynadier, L., and Guyodo, Y., 2005. Geomagnetic dipole strength and reversal rate over the past two million years. *Nature*, 435(7043):802–805. **https://doi.org/10.1038/nature03674**

Wade, B.S., Pearson, P.N., Berggren, W.A., and Pälike, H., 2011. Review and revision of Cenozoic tropical planktonic foraminiferal biostratigraphy and calibration to the geomagnetic polarity and astronomical time scale. *Earth-Science Reviews,* 104(1–3):111–142. **https://doi.org/10.1016/j.earscirev.2010.09.003**

Wilkens, R.H., Westerhold, T., Drury, A.J., Lyle, M., Gorgas, T., and Tian, J., 2017. Revisiting the Ceara Rise, equatorial Atlantic Ocean: isotope stratigraphy of ODP Leg 154. *Climate of the Past,* 13:779–793. **https://doi.org/10.5194/cp-13-779-2017**

Xu, J., Holbourn, A., Kuhnt, W., Jian, Z., and Kawamura, H., 2008. Changes in the thermocline structure of the Indonesian outflow during Terminations I and II. *Earth and Planetary Science Letters,* 273(1–2):152–162. **https://doi.org/10.1016/j.epsl.2008.06.029**

Zijderveld, J.D.A., 1967. AC demagnetization of rocks: analysis of results. *In* Collinson, D.W., Creer, K.M., and Runcorn, S.K. (Eds.), *Methods in Palaeomagnetism:* Amsterdam (Elsevier), 254–286.